2018

Design, Fabrication and Characterization of Graded Transition Joints

Jonathan Galler
Lehigh University

Design, Fabrication and Characterization of Graded Transition Joints

by

Jonathan P. Galler

Presented to the Graduate and Research Committee of Lehigh University
in Candidacy for the Degree of
Doctor of Philosophy

in

Mechanical Engineering

Lehigh University

May 2018

Approved and recommended for acceptance as a dissertation in partial fulfillment of the requirements for the degree of Doctor of Philosophy

_____
Date

_____
Dissertation Director

_____
Accepted Date

Committee Members:

_____
John N. DuPont

_____
Herman F. Nied

_____
Wojciech Z. Misiolek

_____
Richard P. Vinci

Acknowledgements

Thank you to Dr. John DuPont for allowing me to join the Engineering Metallurgy Group so that I could continue my education and switch gears to study Materials Science and Engineering. I am very grateful for the patience, guidance and knowledge he has shared with me in the classroom and on my projects.

I would also like to acknowledge financial support for this research through the Department of Energy, Office of Nuclear Energy. Thank you to my Engineering Metallurgy Group members; Andrew Stockdale, Brett Leister, Daniel Bechetti, Rob Hamlin, Erin Barrick, Rishi Kant, Sean Orzolek, Jonah Duch, and Ally Fraser. You have all taught me so much and I greatly appreciate all the time you have spent helping me improve myself as a researcher and a student. I could not ask for a better group of co-workers.

I would also like to thank everyone in the Lehigh University Materials Science and Engineering department for their generosity and their contributions to this research project. Thank you Sue Stetler, Janie Carlin, Katrina Kraft, Arlan Benscoter, Mike Rex, Bill Mushock, Laura Moyer, and all my fellow graduate students.

Finally, thank you to my mother, father, brothers and girlfriend, Stephanie Panayiotou, for the love and support they have given me through all my endeavors.

Table of Contents

List of Tables

List of Figures

Abstract

Carbon diffusion in dissimilar metal welds (DMWs) at elevated temperatures leads to a microstructure that is susceptible to premature failure. Graded transition joints (GTJs) can potentially provide a viable replacement to prolong the service life of these components. In the current investigation, the use of thermodynamic modeling was used to identify candidate alloys that reduce the chemical potential gradient, which is the driving force for carbon diffusion. Additionally, kinetic modeling was used to determine an optimal grade length for a graded transition joint to further reduce the extent of carbon diffusion. A graded transition joint was fabricated using three candidate filler metals (Inconel 82, EPRI P87, and 347H), aged to understand the microstructural evolution, and characterized for a direct comparison with the observed trends from the model simulations. Microhardness measurements were performed on the GTJs in the as-welded and aged conditions to understand the initial strength gradients throughout the graded region, and how they evolve with aging time. Additionally, energy dispersive spectrometry was performed to measure the compositional gradients, which were input into thermodynamic and kinetic calculations to understand the carbon diffusion behavior and phase stability. Enhanced carbon diffusion occurred at the layer interfaces in the graded region of the GTJ, which indicated important regions that undergo microstructural evolution. The hardness results also revealed hardness changes at the layer interfaces. The analyzed interfaces demonstrated that carbon diffusion and corresponding carbide redistribution occurred that accounted for the observed hardness gradients. Additionally, the transition from a martensitic to austenitic region was observed in each GTJ that contributed to the hardness variations in the graded region. Finally, the formation of a nickel-rich martensitic

constituent was observed in the graded region of all filler metals after aging. This constituent was originally austenite at the aging temperature, and transformed to martensite with no change in composition upon cooling. The morphologies of the constituent in the three filler metals are presented and discussed.

Chapter 1 Introduction

Review of Microstructural Evolution of Dissimilar Metal Welds between 2.25Cr-1Mo Ferritic Steel and Austenitic Alloys

Background

Dissimilar Metal Welds (DMWs) are critical for design, development, and manufacturing of very high temperature reactors. These DMWs are fabricated using fusion welding processes to join a ferritic alloy to an austenitic alloy. A typical example of a DMW used in high temperature reactors is 2.25Cr-1Mo (often referred to as Grade 22) welded to Alloy 800H using Inconel 82 filler metal. The ferritic alloys are used in the lower temperature, less corrosive regions, whereas the austenitic alloys are used in the higher temperature regions where enhanced creep strength and corrosion resistance is necessary. Published literature has demonstrated that failures of such DMWs can be caused by carbon diffusion and thermal stresses (due to mismatch in coefficient of thermal expansion), each of which are driven by the large variation in composition across the narrow interface between the two dissimilar materials.[1–7] The high temperatures encountered during service conditions provide the activation energy for carbon diffusion from the ferritic steel to the austenitic steel. This is attributed to the chemical potential gradient between the two materials, which is the driving force for carbon diffusion.[8–12] The diffusivity of carbon in a BCC matrix is higher than in an FCC matrix, resulting in a carbide buildup at the interface of the two dissimilar materials. In addition, carbon will diffuse down the chemical potential gradient, leaving the ferritic material, and migrating to the austenitic weld metal. The resulting microstructure consists of a carbon depleted region in the ferritic material, a row

of carbides at the weld interface and a carbon enriched region across the weld fusion line. It is this carbon depleted region, in combination with the row of carbides, and mismatch of coefficient of thermal expansion that is most susceptible to strain localization that can lead to premature failure. Therefore, the objective of this introduction is to establish a clear understanding of the microstructural evolution of DMWs between ferritic and austenitic materials.

Carbon Diffusion

Typically, the carbon concentration in the ferritic steel is higher than the austenitic steel. This produces a carbon concentration gradient that results in the natural tendency for carbon to diffuse from the higher to the lower carbon concentration region, down the concentration gradient. In addition, there is a driving force that causes carbon diffusion from the ferritic material to the austenitic material, regardless of the concentration gradient. This is known as the activity gradient, or a chemical potential gradient between the two alloys. This activity is strongly dependent on the concentration of the alloying elements in each alloy, specifically the chromium (Cr) content.[13–16] The chemical potential is high in the ferritic material due to the low Cr content, and lower in the austenitic weld metal (due to the higher Cr content), resulting in a negative chemical potential gradient for carbon to diffuse across the weld interface. The effect of Cr on the chemical potential was investigated by Brentrup *et. al.*[16] by changing the Cr composition of Alloy 800 in a GTJ between Grade 22 and Alloy 800. The results can be seen in Figure 1-1 that shows the chemical potential as a function of position across the GTJ between Grade 22-Alloy 800-347. Two Cr concentrations (10 and 21 weight percent) were chosen, with a larger

concentration resulting in a lower chemical potential value. Thus, the chemical potential gradient from Grade 22 to Alloy 800 is more severe using a higher Cr concentration in Alloy 800. Therefore, a larger Cr content would induce a greater driving force for carbon diffusion due to the steeper chemical potential gradient.

The diffusivity of carbon in ferrite is significantly higher than in austenite, and the solubility of carbon is significantly lower in ferrite, as can be seen in a typical iron-carbon phase diagram.[17] This allows carbon to diffuse faster through ferrite than austenite, but allows a greater amount of carbon to go into solution in the austenitic weld metal. When the carbon concentration in the ferritic alloy drops below the solubility limit (due to the carbon migration to the austenitic weld metal), this disturbs the thermodynamic equilibrium of the system.[13] Therefore, it is energetically favorable for some carbon, which is in the form of carbides, to dissolve into solution to bring the carbon level back up to its solubility value. It is important to note that the carbon tied up in a carbide cannot diffuse, it is the carbon in solution that undergoes interstitial diffusion. Eventually, the weld metal will exceed the carbon solubility limit, and carbides will precipitate. This will result in a carbon enriched region near the fusion line in the weld metal.

The diffusion of carbon from the ferritic material across the weld interface (low Cr to high Cr) will continue until a number of microstructural changes occur. First, Cr carbides that form in the weld metal will result in a depletion of Cr from solution. This drop in Cr content weakens the driving force for carbon to diffuse, since there is a smaller chemical potential gradient between the two materials. Second, the formation of carbides at the weld interface (discussed below) can act as barriers to the diffusing carbon atoms. Furthermore, the low level of carbon in the ferritic material results in less carbon to migrate across the

weld interface. A point can be reached where the HAZ near the weld interface will consist of carbon-free ferrite grains, thus the presence of carbon atoms to diffuse from that region is limited.

Carbide Formation

During aging, a row of carbides forms at the weld interface in the HAZ of the ferritic material. These are known as Type 1 carbides that are commonly reported in DMWs using Grade 22.[3,5,6,18,19] The carbides along the weld interface can grow and coalesce after extended aging. The carbide-matrix interface can act as the preferred site for creep void formation under service conditions leading to premature failure of the DMWs. Parker *et. al*.[5,18] aged DMWs between Grade 22 and Inconel 82 up to 6,000 hours. Two types of carbide morphologies were present in their welds. Type I carbides formed in the HAZ of the ferritic material, very close to the fusion line. This is evident in Figure 1-2a, showing a spherical morphology at the weld interface. After prolonged exposures to elevated temperatures, these carbides can grow and coalesce to form an elongated row along the fusion line, as seen in Figure 1-2b. The other carbide morphology noticed was Type II carbides that also form in the HAZ, but over a wider area, as seen in Figure 1-3. They reported these carbides consist in a martensitic region that is much wider than the observed region of the Type I carbides.

A number of studies have been able to identify these carbides in Grade 22 and austenitic filler metals to be Cr-rich $M_{23}C_6$, or molybdenum (Mo) rich M_6C.[19,20] This is attributed to Cr and molybdenum (Mo) having a high affinity for carbon, deeming them strong carbide formers. Nicholson[19] showed that Cr-carbides form along the weld interface

between Grade 22 and Inconel 182 using transition electron microscopy in combination with energy dispersive x-ray analysis. A number of photomicrographs of the weld interface show these Type I carbides evolution after various aging treatments, as seen in Figure 1-4. One significant phenomenon that was noticed in this study was the increasing distance between the carbides and the weld interface after increased aging times. It is important to note that many other studies have showed this result for Grade 22, but have not commented on the reason for what seems like grain boundary migration. However, Nicholson attributed this phenomenon of interface migration to the interdiffusion of the substitutional species in the materials. Furthermore, Klueh and King[1] discussed Cr and Ni diffusion into the Grade 22 steel, along with iron and carbon diffusing to the weld metal. Carbon diffusion is well understood, however it is believed that substitutional diffusion at the aging temperatures (<600°C) and times will not occur and therefore, another mechanism is driving this interface diffusion. Further investigation must be conducted to fully understand this phenomenon.

Hardness Gradients

The hardness gradients are also important to understand the microstructural evolution near the fusion line. Gittos and Gooch[12] investigated welds between ferritic steel and austenitic steels, and compared the hardness profiles to welds made with Ni-based alloys. Figure 1-5a shows an as-welded microstructure between Grade 22 (bottom) and an austenitic stainless steel (top). There is a large difference in hardness across the fusion line over a very short distance. As stated before, there is a natural tendency for carbon to diffuse to the lower carbon concentration region, across the fusion line. Thus, during aging, carbon

will diffuse from Grade 22 across the fusion line, which only exacerbates the as-welded hardness gradient. Figure 1-5b shows the same weld after a post weld heat treatment at 720°C for 10 hours. There is a carbon depleted region in the ferritic material, a carbon enriched region across the fusion line, as well as a row of carbides at the weld interface in the ferritic material. The hardness changes from 134 to 487 HV, when compared to the as welded hardness difference of 227 to 441 HV. This large change in hardness (and corresponding strength) over a short distance creates a region along the fusion line that is susceptible to strain localization. These steep hardness gradients, combined with the mismatch in CTE and carbon diffusion can cause a microstructure that is susceptible to premature failure.

Failure Mechanisms

As mentioned before, DMW failures are well documented, and the cause for failure can be summarized as follows. The sharp concentration and associated chemical potential gradient between the two materials induces carbon diffusion that results in a carbon depleted region prior to the weld interface and a row of carbides forming at the weld interface in the ferritic material. This also results in a sharp change in strength across the interface (indicated by the sharp microhardness gradients discussed above), which is the prime location for strain localization. The mismatch in CTE between the ferritic material and filler metal only exacerbate the problem by providing further stain localization in this region. Under stress at elevated temperatures, the row of carbides will coalesce and form creep voids at the carbide-matrix interface. These creep voids will eventually link up to cause failure in the HAZ near the weld interface prior to the expected service life.

Parker and Stratford[7] investigated the higher temperature performance of nickel-based transition joints. They concluded that creep void formation occurred at the row of carbides along the weld fusion line, as seen in Figure 1-6. These creep voids eventually linked together to form a crack along the interface, as seen in Figure 1-7. This is the primary cause for premature failures in DMWs between Grade 22 and austenitic or Ni-base alloys. The mismatch of coefficient of thermal expansion can be reduced with the use of Ni-based filler metals, however, the steep hardness and concentration gradients still occur over very short distances, and carbon diffusion will occur to form soft and hard zones. The failure of these DMWs is well established, thus, the next step is to determine a long term solution to these premature failures.

Use of Nickel-Based Filler Metals

Nickel-base filler metals are more commonly used in DMW applications due to their decrease in carbon diffusion compared to austenitic alloys.[12,19,21] Gittos and Gooch[12] characterized the weld interface of a DMW using a Ni-base filler metal after a post weld heat treatment and aging. They observed, even at the longest aging treatment times, there was no decarburized layer visible in the HAZ of the ferritic alloy. This suggests carbon diffusion was limited and did not create a carbon depleted region, which is observed in DMWs using austenitic filler metals. Additionally, the martensitic layer that forms in the partially mixed zone (PMZ) of the DMWs decreases when using a Ni-base filler metal. DuPont and Kusko[22] investigated the martensite start temperature on DMWs using austenitic and Ni-base filler metals. They concluded the martensitic layer is significantly

smaller in the Ni-base filler metal, attributed to the steep Ni concentration gradient between the two materials that stabilizes austenite earlier in the PMZ.

In the current thesis, Chapter 1 discusses the background of DMWs and the importance of understanding the microstructural evolution in order to prevent premature failure. Chapter 2 is concerned with establishing a preliminary description of why graded transition joints can be a suitable replacement of DMWs. Furthermore, it provides an overview of the models created to simulate carbon diffusion and phase fraction across the PMZ and graded regions. The calculated carbon diffusion over various grade lengths after extended aging times, was directly compared to the conventional DMW. Chapter 3 builds on the results from Chapter 2 and is focused on characterizing the microstructures in the graded regions.

References

1. Klueh, R.L., King, J.F. Austenitic Stainless Steel-Ferritic Steel Weld Joint Failures. *Weld J*. 1982;(September):302-311.
2. DuPont, J.N. Microstructural evolution and high temperature failure of ferritic to austenitic dissimilar welds. *Int Mater Rev*. 2012;57(4):208-234.
3. Laha, K., Chandravathi, K.S., Rao, K.B.S., Mannan, S.L., Sastry, D.H. An Assessment of Creep Deformation and Fracture Behavior of 2 . 25Cr-1Mo Similar and Dissimilar Weld Joints. *Metall Mater Trans a*. 2001;32A(January):115-124.
4. Lundin, C.D. Dissimilar Metal Welds — Transition Joints Literature Review. *Weld J*. 1982;(Feb):58s-63s.
5. Parker, J.D., Stratford, G.C. Review of factors affecting condition assessment of nickel based transition joints. *Sci Technol Weld Join*. 1999;4(1):29-39.
6. Parker, J.D., Stratford, G.C. The high-temperature performance of nickel-based transition joints. I. Deformation behaviour. *Mater Sci Eng A*. 2001;299(1-2):164-173.
7. Parker, J.D., Stratford, G.C. The high-temperature performance of nickel-based transition joints. II. Fracture behaviour. *Mater Sci Eng A*. 2001;299(1-2):174-184.
8. Christoffel, R.J., Curran, M.R. Carbon Migration in Welded Joints at Elevated Temperatures. *Weld J*. 1956;35(9):457s-468s.
9. Porter, D.A., Easterling, K.E., Sherif, M.Y. *Phase Trasformations in Metals and Alloys*. Third. Taylor and Francis Group; 2009.
10. Darken, L.S. Diffusion of carbon in austenite with a discontinuity in composition. *Metall Mater Trans B Process Metall Mater Process Sci*. 1948;41(4):430-438.

11. Eckel, J.F. Diffusion Across Dissimilar Metal Joints. *Weld J*. 1964;43(4):170s-178s.

12. Gittos, M., Gooch, T. The interface below stainless steel and nickel-alloy claddings. *Weld Res Suppl*. 1992:461-472.

13. Sudha, C., Paul, V.T., Terrance, A.L.E., Saroja, S., Vijayalakshmi, M. Microstructure and Microchemistry of Hard Zone in Dissimilar Weldments of Cr-Mo Steels. *Weld J*. 2006;85(April):71s-80s.

14. Anand, R., Sudha, C., Paul, V.T., Saroja, S., Vijayalakshmi, M. Microstructural Changes in Grade 22 Ferritic Steel Clad Successively with Ni-Based and 9Cr Filler Metals. *Suppl to Weld J*. 2010;89(April):65-74.

15. Laha, K., Latha, S., Rao, K.B.S., Mannan, S.L., Sastry, D.H. Comparison of creep behaviour of 2.25Cr–1Mo/9Cr–1Mo dissimilar weld joint with its base and weld metals. *Mater Sci Technol*. 2001;17(10):1265-1272.

16. Brentrup, G.J., DuPont, J.N., Snowden, B.S., Grenestedt, J.L. Design Considerations of Graded Transition. *Weld J*. 2012;91(September).

17. Callister, W.D., Rethwisch, D.G. *Materials Science and Engineering: An Introduction*. Vol 94.; 2007.

18. Parker, J.D., Stratford, G.C. Characterization of microstructures in nickel based transition joints. *J Mater Sci*. 2000;35(16):4099-4107.

19. Nicholson, R.D. Effect of aging on interfacial structures of Ni based transition joints. 1984;11(March):115-124.

20. Pilling, J., Ridley, N. Tempering of 2.25 Pct Cr-1 Pct Mo Low Carbon Steels. *Metall Trans A*. 1982;13(4):557-563.

21. Klueh, R.L., King, J.F. Thermal-Aging Behavior of ERNiCr-3 Alloy (Weld and Base Metal). 1981;(August):ORNL-5783.

22. DuPont, J.N., Kusko, C.S. Technical note: Martensite formation in austenitic/ferritic dissimilar alloy welds. *Weld J*. 2007;86(2):51.

Appendix

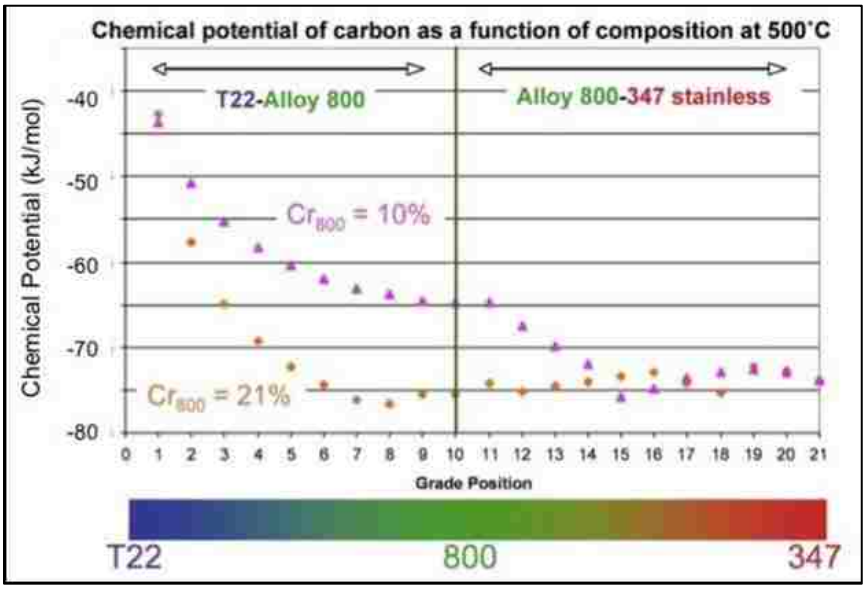

Figure 1-1. Chemical Potential as a function of position across a GTJ between T22-Alloy 800 and Alloy 800-347 showing the effect of Cr on the chemical potential.

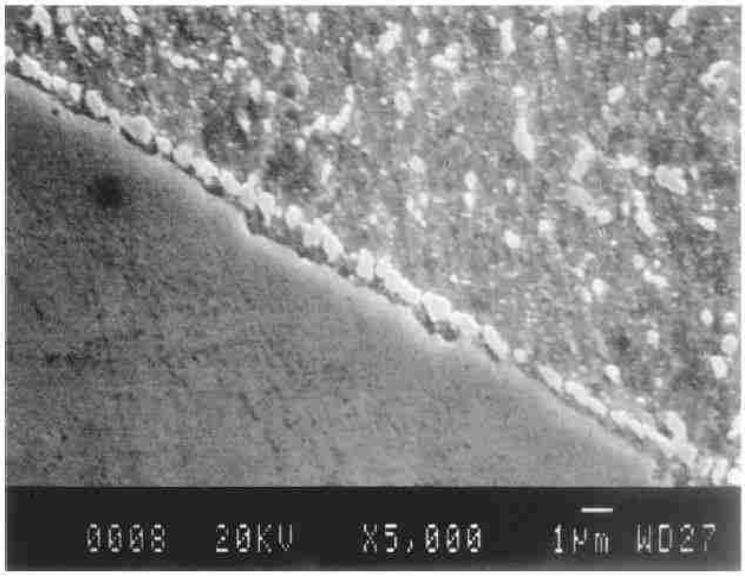

a)

Figure 1-2. A row of type I carbides that form along the weld interface in the ferritic material, and b) after further aging treatments resulting in carbide coarsening.

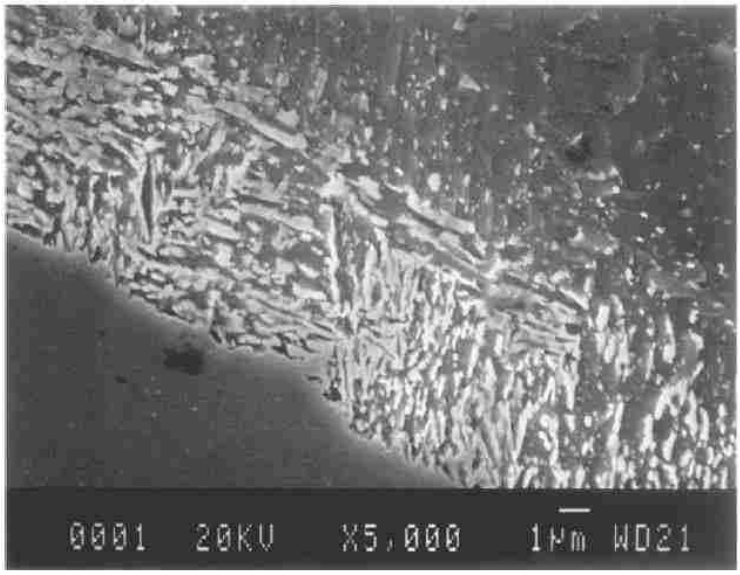

Figure 1-3. A region of type II carbides that form along the weld interface in the ferritic material.

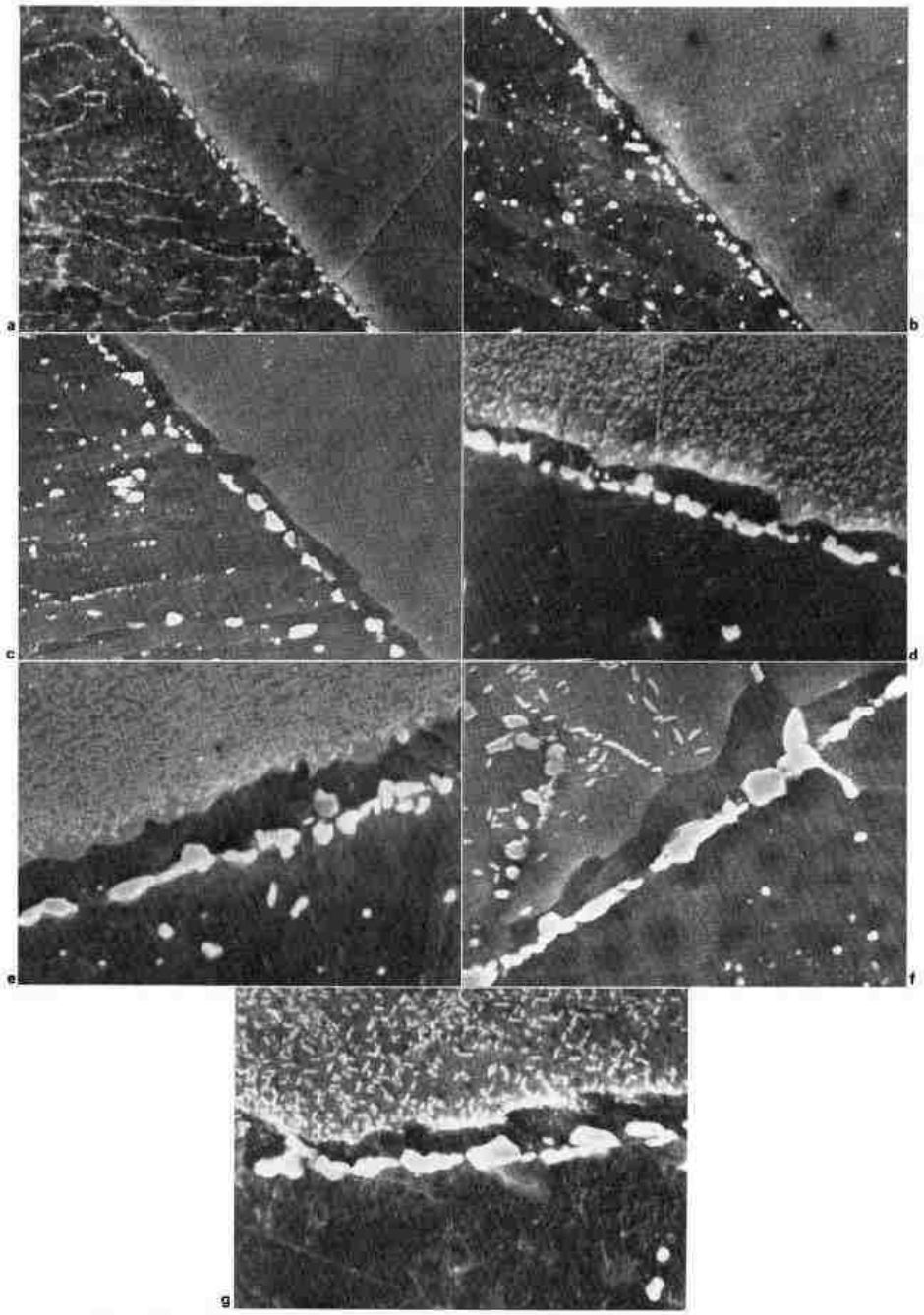

Figure 1-4. A row of type I carbides that form along the weld interface in the ferritic material after further aging treatments resulting in carbide coarsening. Also note the distance between the carbides and weld interface increases with increasing aging time.

a)

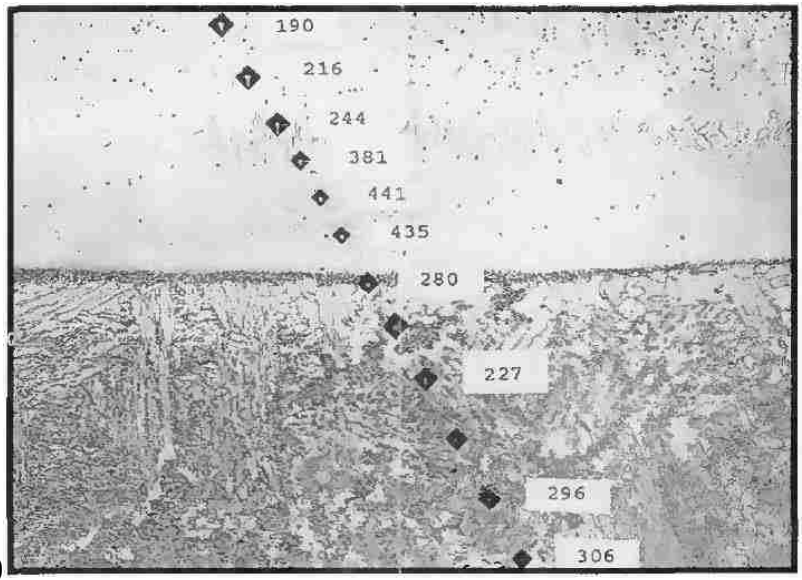

b)

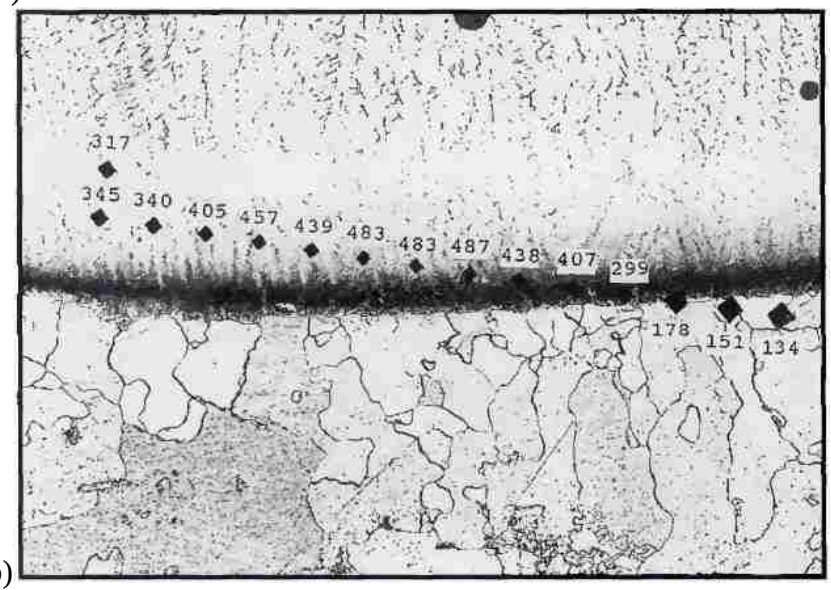

Figure 1-5. Hardness trace across the weld interface of a DMW between grade 22 (bottom) and 309L (top) in a) the as-welded condition and b) aged condition.

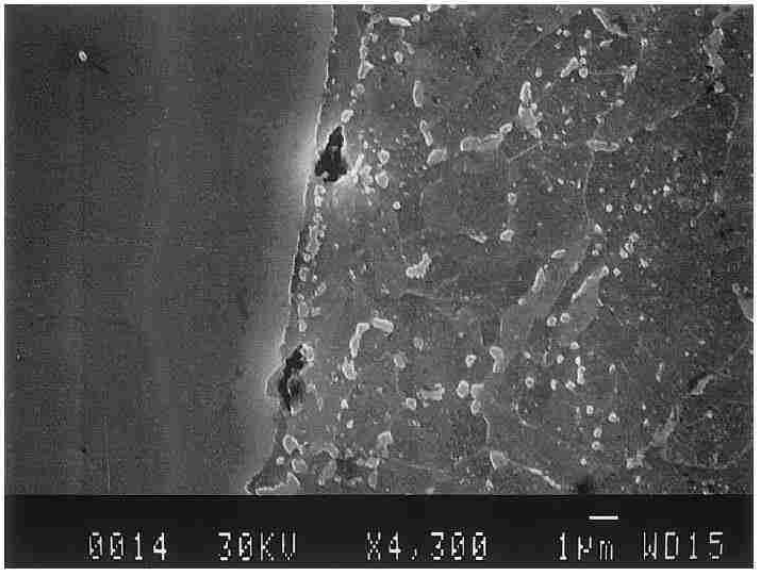

Figure 1-6. The initiation of creep void formation at the carbide-matrix interface after DMWs were creep tested after aging treatments.

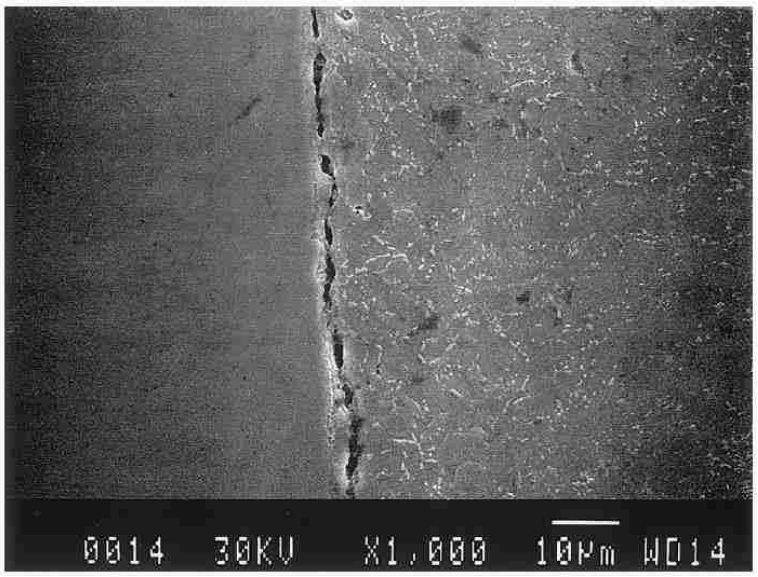

Figure 1-7. The presence of creep voids linking up along the weld interface that results in the premature failure of DMWs.

Chapter 2 Design of Graded Transition Joints through Thermodynamic and Kinetic Modeling

Abstract

Dissimilar metal welds between ferritic and austenitic alloys are common in high temperature applications in the energy industry. Under service conditions, these welds experience carbon diffusion and concomitant detrimental microstructural changes that can render them susceptible to premature failure. Therefore, it is necessary to identify a filler metal and joint design to reduce the driving force of carbon diffusion and prolong the expected service life. In the current investigation, the use of thermodynamic modeling was used to identify candidate alloys that reduce the chemical potential gradient, which is the driving force for carbon diffusion. Additionally, kinetic modeling was used to determine an optimal grade length for a graded transition joint to further reduce the extent of carbon diffusion. A graded transition joint was fabricated and aged to understand the microstructural evolution, and characterized for a direct comparison with the observed trends from the model simulations. It was determined that increasing the grade length to the millimeter length scale reduced the extent of carbon diffusion by an order of magnitude when compared to a conventional dissimilar metal weld with a concentration gradient on the length scale of ~10 – 100 microns. Additionally, a step function composition gradient was implemented into the diffusion calculations to simulate the more realistic gradients produced with additive manufacturing processes. In these stepped gradients, carbon diffusion occurred at the layer interfaces, indicating important regions that undergo

microstructural evolution. The experimentally observed carbide distribution in the characterized graded transition joints is in good agreement with the calculated carbide distribution. Finally, the formation of a nickel-rich martensitic constituent was observed in the graded region after aging. This constituent was originally austenite at the aging temperature, and transformed to martensite upon cooling with no change in composition. The formation of this constituent was also accurately captured in the model results.

Introduction

Dissimilar metal welds (DMWs) are commonly used in energy applications where varying material behavior is necessary due to the high temperature operating conditions. DMWs, specifically in power generation applications, are typically produced by joining a ferritic steel (typically 2.25Cr 1Mo, also called Grade 22) to alloy 800H (commonly used in power generation) using a nickel-base filler metal. The ferritic steel is used in lower temperature, less corrosive environments, whereas the austenitic alloy is used in higher temperature regions where enhanced creep strength and corrosion resistance are required. In this application, the alloys are joined using standard fusion welding processes. This produces very abrupt and uncontrolled gradients in composition, microstructure, and resultant thermal and mechanical properties.[1,2] These sharp gradients lead to premature failure in the ferritic steel near the weld interface, which is a primary concern of the power generation industry. These failures can result in forced plant outages that may cost a power company up to $850,000 per day in lost revenue and repair costs.[3]

It is important to have a thorough understanding of the failure mechanism of these DMWs to design an alternative solution to prevent failure. A large body of work has been conducted to study the mechanisms that lead to premature failure[1,4–8], and the failure mechanism has recently been reviewed in detail.[2] The failures can be attributed to three major factors. The first is the difference in carbon concentration between the two materials, and the microstructural evolution due to carbon diffusion during aging. This promotes sharp changes in microstructure and concomitant mechanical properties along the fusion line. The second factor is the formation of carbides along the fusion line in the heat affected zone (HAZ) of the ferritic material due to carbon migration during service. A typical DMW

failure is initiated from creep voids that form at the carbide-matrix interface.[6,9] Therefore, the presence of these carbides creates a microstructure that is susceptible to creep failure. Finally, the coefficient of thermal expansion (CTE) mismatch between the ferritic and austenitic materials can cause strain localization along the weld interface. This, combined with the previously mentioned issues, exacerbates the susceptibility to failure.

It is well known that concentration gradients defines the diffusion path in a binary alloy system, as an element will typically diffuse down the gradient from high to low concentrations.[10,11] However, tertiary and higher order additions of alloying elements in real, multi-component materials will create a chemical potential gradient that is relieved by the diffusion of elements in the system. Studies have demonstrated the presence of additional elements can create a chemical potential gradient that counteracts the concentration gradient, which results in "uphill" diffusion.[5,10,12–14] In a DMW, the chemical potential of carbon (CPC) gradient generally causes carbon to diffuse from the ferritic material to the austenitic material. This results in a carbon depleted region in the ferritic material, and a carbon enriched region in the partially mixed zone (PMZ). This microstructural evolution (along with CTE mismatch) leads to strain localization near the interface, and contributes to premature failure. Thus, the primary driving force for carbon diffusion in a multicomponent system is the chemical potential difference and resulting CPC gradient between two materials. The diffusion of elements over time will eventually cease when the chemical potential difference is relieved in the system.[11]

It has been reported that the chromium (Cr) content has the largest effect on the CPC.[13,15–17] Brentrup and DuPont varied the Cr content in a Grade 22-800H DMW system to determine the effect on CPC gradient and the concomitant driving force for carbon

diffusion.[18] The larger Cr content in the austenitic material resulted in a steeper CPC gradient, and therefore, a stronger driving force for carbon diffusion. Thus, a reduction in Cr content in the filler metal can reduce the driving force for carbon diffusion. However, the need to further reduce the inevitability of carbon diffusion is necessary, and an alternate method is presented below.

In the current study, the design and fabrication of a graded transition joint (GTJ) was investigated, as it poses a new method to mitigate the carbon diffusion problem. A GTJ exhibits a gradual change in composition between the two materials over larger distances then a DMW. This reduces the sharp changes in microstructure and corresponding thermal and mechanical properties, and reduce the mismatch of CTE that is known to cause strain localization.

Brentrup and DuPont modeled the carbon diffusion of a DMW and GTJ between Grade 22 and Alloy 800H.[18] As expected, a longer grade length significantly reduced the concentration gradient and associated CPC gradient and thus, the extent of carbon diffusion. Transition joints were also investigated by Sridharan *et. al*. using a powder blown additive manufacturing process to join Grade 22 to 316L using SS410 filler.[19] This study attempted to reduce solidification cracking susceptibility of the common filler metal Inconel 82 during fabrication by grading 316L with an austenitic filler (SS410). While they successfully fabricated and characterized the GTJ that did not contain solidification cracks, there is still a need to understand the microstructural evolution and concomitant carbon migration that occurs during aging at high temperatures.

The primary objective of the current investigation is to understand the extent of carbon diffusion expected among different austenitic filler metals and Grade 22 steel, and

analyze the microstructural evolution expected to occur during service conditions. The results from this study form a basis for optimizing GTJs to reduce the extent of carbon diffusion and the detrimental microstructures susceptible to premature failure. Based on the detailed modeling study, optimal grade lengths to minimize carbon diffusion are identified and the details of carbon diffusion behavior is discussed. Additionally, the model can be used as a predictive tool to calculate the extent of carbon diffusion for a given alloy system.

Modeling and Experimental Procedure

The allowable composition ranges of the base metal and filler metals investigated in this work are given in Table 2-1. A wide range of commercially available alloys were initially chosen for this study, as these alloys have been approved by pertinent codes and previously used for energy applications. The alloys selected have been welded directly to ferritic materials in many power generation applications, and are known to have good high temperature creep properties. Future work will explore the potential development of new candidate filler metals without the need to restrict compositions to those approved by various codes.

Initial thermodynamic calculations were conducted using ThermoCalc® software to isolate the effect individual elements had on the CPC of the system.[20] The TCFE7 and NI-DATA-V7 databases were used for high iron (Fe) materials and nickel (Ni) base alloys, respectively.[21,22] Individual elements were varied while simultaneously changing the Ni content (to account for the change), and the remaining composition stayed constant to identify the individual effect an element had on the CPC. Concentrations were selected to

induce the largest CPC gradients that produce the largest extent of carbon diffusion. A revised set of compositions that were used for the simulations is shown in Table 2-2.

In both DMWs and GTJs, the CPC will vary within the PMZ that represents the region where partial mixing occurs between the underlying substrate and filler metal. The incremental change in composition within this PMZ can be characterized by the dilution.[23] The CPC gradient as a function of dilution was calculated at 400°C, 500°C, and 600°C to fully understand the extent of the driving force for carbon diffusion over a typical operating temperature range (400 and 500°C) and to also model an accelerated aging treatment (at 600°C) that was conducted experimentally. The dilution between the two materials was varied by 10% increments that resulted in 11 compositions (including Grade 22).

Aging simulations were performed using DICTRA® in conjunction with the two databases mentioned above and the MOB2 mobility database.[24,25] The following phases were allowed to form based on relevant literature for each material: Austenite, ferrite, $M_{23}C_6$, M_6C, and FCC2 (an additional carbide phase).[4,26–28] The length of the graded region was set as 50 μm for DMW calculations. This is a typical distance of the PMZ in a DWM.[1,5,14,29] Grade lengths were varied for the GTJ calculations to develop the optimal grade design to minimize carbon diffusion. A linear composition gradient was assumed and included a source of each material as end members. Carbon diffusion and phase fraction profiles were extracted from the kinetic simulations for the DMWs and GTJs to compare to actual GTJs that were fabricated, aged at 600°C, and characterized.

Optimal grade lengths of 10 mm and 20 mm were chosen for the fabrication of the GTJs. These joints were fabricated using a dual wire gas tungsten arc welder, as described in prior work.[30] Wire feed rates were varied for each weld pass to match a desired dilution

for a given layer until the graded region was built to 100% filler metal. Samples were then placed in Fisher Scientific furnaces for an accelerated aging study at 600°C up to 8,000 hours to understand the microstructural evolution. Metallographic samples were cross sectioned and prepared using standard metallographic techniques to a final polished state of 0.05 μm colloidal silica. 2% Nital solution was used as an etchant to reveal grain boundaries and carbides in the ferritic material.

Compositional line traces with a 100 μm step size were conducted on the as-welded GTJs in the polished condition using a Leo Gemini 1550 VP scanning electron microscope equipped with an 80mm^2 Oxford X-MAX silicon drift detector capable of count rates up to 100,000/sec (based on current parameters). An operating voltage of 15 keV and 60 μm aperture allowed for 30% dead time. Secondary electron imaging and x-ray energy dispersive spectrometry (EDS) were performed in a Hitachi 4300SE/N Schottky field emission scanning electron microscope at an operating voltage of 15 keV. Compositions measured from this analysis are standardless and therefore, semi-quantitative. The accuracy of this technique was evaluated using custom "standards" analyzed via optical emission spectroscopy (OES). Table 2-3 shows the results from EDS alongside the OES results. EDS measurements show good agreement with the OES measurements. Therefore, this measurement technique should be sufficient enough to identify regions of local enrichment. Monte Carlo simulations using the CASINO program demonstrated that the x-ray generation volume was approximately 1 μm^3 under the operating conditions.[31] Thus, results of sub-micron size particles are likely affected by the surrounding matrix material, but were still useful for identifying the formation of expected phases.

Results and Discussion

Chemical Potential of Carbon Calculations

The CPC was calculated for a wide range of alloys and compared to the CPC of Grade 22. Since the CPC gradient is the driving force for carbon diffusion, the most promising alloys will have a CPC similar to Grade 22. This will reduce the CPC gradient and corresponding driving force and thus, minimize carbon diffusion. Figure 2-1 shows the CPC of each material as a function of temperature with Grade 22 shown on the left (in red) for each temperature.

The justification of the selected candidate alloys are as follows: 347H, Inconel 182 and Inconel 82 are the three filler metals with the closest CPC to that of Grade 22 at each temperature. IN800 was included as a reference, as it represents the end member for the application (but is not available as filler metal). Work conducted by Brentrup *et. al*. reported that the direct joining of Grade 22 to IN800 resulted in solidification cracks.[30] Thus, IN800 would not be a viable filler metal for direct grading to Grade 22 steel. Inconel 617, 625, and 718 exhibit a relatively large difference in CPC compared to Grade 22 for all temperatures. In addition, recent results have shown undesirable brittle intermetallic phases would be stable when these filler metals are joined to a ferritic steel.[32] Therefore, these three alloys do not appear to be good candidates and thus, were not considered. 347 was not considered since 347H has a higher carbon content (closer to Grade 22), and has a closer CPC to that of Grade 22.

Only considering the difference in CPC at each temperature, 347H, Inconel 182, and Inconel 82 were initially chosen as candidate alloys. However, as mentioned previously, the CTE mismatch at elevated temperatures between Grade 22 and the

candidate alloys was also considered. In addition to having a reasonable CPC match, P87 has a closer CTE match to Grade 22 at elevated temperatures than the other alloys and was therefore considered.[33] Thus, the candidate alloys chosen for this study were Inconel 82, 347H, and P87.

Within a GTJ, the Grade 22 steel will become diluted with the composition from the filler metal until the end of the graded region, which consists of "100% dilution" of filler metal (i.e "pure" filler metal). The CPC gradient was determined by taking 10% increments of the candidate alloy's dilution with Grade 22 (using Grade 22 and the filler metal compositions shown in Table 2-2) and calculating the CPC for each composition. Figure 2-2a-c shows the CPC as a function of dilution for the three candidate alloys. The results for Inconel 82 (Figure 2-2a) and 347H (Figure 2-2c) show a steep CPC gradient at the start of the dilution (after x=0). The gradient decreases towards the end of the dilution, and under certain conditions turns positive. Constitution boundary lines are superimposed onto the figure from the well-known Schaeffler diagram, which shows the major phases that form in ferritic and austenitic welds at a given composition.[34] Note the Schaeffler diagram does not account for secondary phases such as carbides, thus only martensite and austenite are included. In all figures, martensite is expected to form at the beginning of the grade, encompassing Grade 22, followed by a region of mixed martensite and austenite. The composition will reach a point where only austenite is predicted to form. The beginning of the grade is where the CPC gradient is the steepest and the most carbon diffusion is therefore anticipated. Thus, as described in more detail in a later section, the beginning of the grade can be elongated to minimize the CPC gradient and extent of carbon diffusion.

Aging Simulations

A DMW composition gradient across the PMZ is typically on the order of 10 – 100 microns in length.[1,5,14,29] Therefore, the simulation for a baseline case for conventional DMWs was selected as 50 μm in length using a linear change in composition. DICTRA® was used to model the carbon concentration as a function of distance for various aging times at an elevated temperature. Figure 2-3a shows the carbon concentration as a function of distance for a DMW between Grade 22 and Inconel 82 with a 50 μm PMZ aged at 500°C up to 8,000 hours. On either side of the 50 μm transition region is a source of the two end members (Grade 22 and Inconel 82). It is known that DMWs between ferritic and austenitic materials result in a carbon depleted region prior to the fusion line in the HAZ of the ferritic material, and a carbon enriched region in the PMZ.[15,35,36] Thus, the model results are consistent with findings in literature.

The carbon concentration in the as-welded condition at the weld interface (x=10 mm) initially starts at 0.15 weight percent, and is reduced to ~0.10 weight percent after simulated aging for 8,000 hours. Furthermore, carbon enrichment in the PMZ increased to 0.70 weight percent after aging 8,000 hours, which can lead to extensive carbide formation. Figure 2-3b shows the same simulation with an output of phase fraction as a function of distance after simulated aging for 8,000 hours at 500°C. Body centered cubic (BCC) is the dominate phase before the interface since Grade 22 is a ferritic material, and face centered cubic (FCC) becomes the dominate phase through the PMZ as the dilution increases towards Inconel 82. Studies have shown that DMWs fabricated with Grade 22 form $M_{23}C_6$ and M_6C carbides in the HAZ of the ferritic steel.[1,4,14,17,27] The model

shows the formation of three types of carbides; $M_{23}C_6$ chromium carbide which reaches a maximum of 0.08 phase fraction, M_6C molybdenum carbide at a max of 0.005 and MC (niobium) carbide a max of 0.02 phase fraction. Again, the model results are consistent with findings in literature.

The composition gradient controls the chemical potential gradient and concomitant carbon diffusion. With GTJs, the concentration gradient is decreased by simply increasing the distance over which the composition varies from Grade 22 base metal to the austenitic filler metal. The decrease in the composition gradient will decrease the chemical potential gradient and the extent of carbon diffusion in the system. Figure 2-4 compares the effect of temperature and grade length on carbon diffusion after simulated aging for 8,000 hours for a DMW and GTJ between Grade 22 and Inconel 82. Figure 2-4a-c has a transition region of 50 μm (typical of a DMW). As expected, an increase in aging temperature results in greater carbon depletion prior to the fusion line, and a significant increase in carbon enrichment in the PMZ. Figure 2-4d-f shows results of a GTJ with a transition region of 10 mm. The results have the same trend as the DMW results, but the extent of carbon diffusion is significantly reduced when compared to a typical DMW. (Note the differences in the scales of the y-axes between the DMW and GTJ). Carbon enrichment in the PMZ of the DMW is as high as 1.7 weight percent when aged for 8,000 hours at 600°C, while the GTJ exhibits carbon enrichment of only 0.2 weight percent under the same conditions. This illustrates that an increase in grade length significantly reduces the driving force and the extent of carbon diffusion.

A summary of the modeling results for all DMWs and GTJs aged at 500°C is shown in Figure 2-5. The percent carbon loss at the weld interface is plotted as a function of

simulated aging time up to 20 years. The percent carbon loss at the interface refers to the difference in carbon content after aging compared to the nominal Grade 22 concentration (0.15 weight percent). The three candidate alloys are plotted using grade lengths of 50 μm (labeled "DMW" in Figure 2-5), 10 mm, and 20 mm to resemble a conventional DMW and GTJs, respectively. It is interesting to note, after an initial loss in carbon after 2,000 hours, the P87 and Inconel 82 DMWs then exhibit a decrease in carbon loss with additional aging time. The DMW made with 347H shows a continuous increase in carbon loss with time, also demonstrated by the GTJs. Results from this summary are discussed below.

The CPC and concentrations of Fe, Ni, Cr, and C as a function of distance are shown in Figure 2-6a, 6c, and 6e for the DMW 347H, and Figure 2-6b, 6d, and 6f for Inconel 82. The starting condition of the CPC in the as-welded condition for 347H (Figure 2-6a) shows a significant decline from Grade 22 towards 347H until it remains constant when $x \geq 10.050$ mm. Note that the slope of the CPC is always negative within the graded region. In contrast, Inconel 82 exhibits a steep decline in CPC until the CPC gradient turns positive around $x=10.025$ mm (Figure 2-6b). This gradient change can be explained by the composition profiles for each system, combined with the CPC trends shown in Figure 2-7 that reveal the impact individual elements have on the CPC. The CPC difference compared to Grade 22 is plotted against the concentration for Cr, niobium (Nb), C, and Ni (Figure 2-7a). Individual elements in the Inconel 82 system were varied with a simultaneous change with Ni to show how each element effects the CPC. As shown, a decrease in Cr will increase the CPC, an effect that is more prevalent for higher Cr contents (Cr > 10 wt %), resulting in a value closer to Grade 22 (designated at the top of the graph). Conversely, the effect of Ni (replaced with Fe) is almost negligible until lower Ni concentrations, where

a decrease will decrease the CPC, thus increasing the mismatch of Grade 22. C and Nb have little effect on Inconel 82's ability to minimize the mismatch of Grade 22's CPC. While the effects are small, a decrease in Nb and an increase in C will increase the CPC, thus decreasing the CPC mismatch of Grade 22. The trends were also conducted on Grade 22 as a baseline while simultaneously varying Fe, with the trends shown in Figure 2-7b. The trends between the two materials are the same, however the slopes (and corresponding relevance) is different. For example, an increase in Nb in Grade 22 decreases the CPC almost 50 kJ/mol when compared to the change of Nb in Inconel 82. Additionally, the increase in Cr has a larger affect for low Cr values. Although these results are insightful, the CPC values are for the end members (base and filler metals), and does not account for variations in the PMZ. For example, decreasing the Cr content will decrease the mismatch of the CPC, but worsen the effects of the CPC "well" in the PMZ.

To fully understand the cause for the "well" seen in the PMW between Grade 22 and Inconel 82, individual elements were varied and the initial CPC was calculated throughout the PMZ. It was determined the Nb concentration had the largest effect on the "well", as shown in Figure 2-7c. The CPC as a function of distance for two Nb concentrations in Inconel 82 is shown, along with the phase fraction of the Cr and Nb carbides. A higher Nb concentration causes the Cr carbide ($M_{23}C_6$) to dissolve at the expense of the Nb carbide (NbC), which significantly affects the CPC of the system. This is the condition the Grade 22-Inconel 82 DMW experiences. As expected, an increase in the Nb concentration results in an increase in the NbC phase, which decreases the CPC in the PMZ. However, a decrease in Nb in Inconel 82 results in an increase in CPC in the PMZ, minimizing the formation of the "well". Further evidence of the Nb effect is shown

in Figure 2-7d for the DMW between Grade 22 and 347H. Similarly, two Nb concentrations (0.15 wt%, representative of 347H, and 3 wt%) were investigated to determine the effect on the 347H system that contains similar Cr contents, but significantly less Ni than Inconel 82. The increase in Nb concentration causes the $M_{23}C_6$ to dissolve, as seen in the previous condition. This results in a steep reduction in the CPC. Increasing the Ni concentration in combination with matching the other elements to that of Inconel 82 will have an effect of increasing the CPC in the end member, thus creating a "well" in the PMZ.

Looking back at Figure 2-6e, there is a localized carbon depletion at the Grade 22-PMZ interface (x=10 mm), and the carbon concentration decreases with increasing aging time when x<10.025 mm. The carbon concentration increases with aging time when x>10.025 mm. The local decrease in carbon at the interface is attributed to the abrupt discontinuity of the CPC observed in the as-welded condition at the start of the PMZ in Figure 2-6a. To alleviate this discontinuity, carbon decreases in the Grade 22 during aging, since a decrease in carbon decreases the CPC (Figure 2-7a). The decrease in carbon concentration with aging when x<10.025 mm, and increase in carbon beyond this point, is attributed to the curvature of the CPC gradient shown in Figure 2-6a. The CPC profile has a negative curvature (concave down) for x<10.025 mm and, as a result, the carbon concentration values decrease with time. In contrast, for x>10.025 mm, the CPC profile has a positive curvature (concave up) so the same values increase. This also accounts for the localized enrichment shown by the carbon peaks in the PMZ.

The principles discussed above can be applied to the trends shown in the DMW between Grade 22 and Inconel 82. However, the difference between 347H and Inconel 82

filler metals lies in the behavior of the CPC curve and corresponding carbon profile at the Grade 22/PMZ interface. After the initial decrease in carbon at and near the interface after 2,000 hours (associated with alleviating the CPC discontinuity) the carbon content increases with aging time in the DMW between Grade 22 and Inconel 82. Although minor, this increase in carbon (not seen in the GTJs or 347H DMW) after aging beyond 2,000 hours is attributed to the behavior of the CPC curve and the presence of the CPC "well" (located in the center of the PMZ in Figure 2-6b) that reduces the driving force for carbon diffusion. Since carbon cannot diffuse up the CPC gradient, a pile-up of carbon will occur that causes an overall increase in carbon content that continues into the Grade 22. Additionally, due to the shape of the "well", there will be carbon diffusion from both the Grade 22 and Inconel 82. This is evident in Figure 2-6f at x=10.05 mm. Carbon will diffuse down the right side of the CPC well resulting in a carbon depleted region at the start of the "pure" Inconel 82, and a localized carbon enriched region at the end of the PMZ. This explains why Ni-base filler metals reduce the extent of carbon diffusion, which has already been reported in literature.[1,14,37] However, the fundamental reason for this reduction has not been recognized, as the CPC "well" has not been reported. This phenomenon explains the underlying reason for the increase in carbon observed before the interface that is not present in DMWs made with Fe-base (as opposed to Ni-base) filler metals. The DMW using P87 (a Ni-base filler metal) follows almost identical trends as Inconel 82. Therefore only Inconel 82 was discussed.

The carbon content was calculated for each phase throughout the simulated GTJs aged at 500°C for 8,000 hours. The results for the GTJ between Grade 22 and Inconel 82 are shown in Figure 2-8a, where the carbon concentration in each phase as a function of

distance is shown for the five stable phases. The carbon resides almost completely in the carbides, as the BCC and FCC phases have negligible carbon contents. This result can assist in understanding the microstructures of actual aged DMWs with regards to the extent of carbon, as a region enriched in carbides suggests a large extent of carbon. Thus, the observed carbides are a good indication of the extent of carbon. Additionally, the observed carbides can be compared with the calculated carbon content shown in Figure 2-6e and 6f. The DMW using 347H shows a carbide depleted region in the Grade 22 prior to the weld interface (shown far left in Figure 2-8c), with carbides (represented by white particles) in the matrix. This can be directly compared to the DMW using Inconel 82 (Figure 2-8d) that shows a larger extent of carbides in the Grade 22 HAZ matrix (left of the image). The extent of carbon, represented by carbides, in the base metal is shown in Figure 2-8b for reference. This observation of a larger carbon depleted region in the DMW using 347H is consistent with the calculated carbon in Figure 2-6e and 6f, and provides further evidence that using a Ni-base filler metal reduces carbon diffusion. Furthermore, another major microstructural difference between the two DMWs is the formation of a larger martensitic layer in the PMZ of the DMW using 347H. A thicker martensite layer is expected in welds produced with Fe-base austenitic filler metals, as shown from DuPont and Kusko.[38] This can be attributed to the smaller concentration gradient within the PMZ, when compared a Ni-base filler metal, due to the lower Ni concentration. A larger Ni concentration will stabilize austenite at a shorter location in the PMZ, resulting in a thinner martensitic layer. This is consistent with the calculated phase fractions for the DMWs using Inconel 82 and 347H, shown in Figure 2-9. After 10 μm, there is no BCC phase in the Inconel 82 DMW,

and the FCC phase consists of 90% of the system. Conversely, it takes a further distance, more than half of the PMZ, for the FCC phase in 347H to become the dominant phase.

The simulated GTJs for the same filler metals exhibit significantly less carbon depletion at the interface. This is illustrated in Figure 2-10-b and Figure 2-10c-d that plots both the carbon and CPC profiles for 347H and Inconel 82, respectively. In both GTJs, carbon decreases prior to the interface with increased aging time, but the reduction is minimal relative to a DMW. Since the CPC gradient is three orders of magnitude lower than that in the DMWs, the driving force is significantly lower for carbon diffusion to occur. Although a CPC "well" still occurs in Inconel 82 GTJ (Figure 2-10b), the aging time would need to be drastically extended for the carbon content at the interface to increase. For comparison, a 2 mm graded region was modeled under the same conditions as the DMWs and GTJs (500°C), and the aging time necessary for carbon to increase after the initial depletion prior to the interface is 1,000 years. These results demonstrate that grade lengths of 10 mm and 20 mm for each material result in less than 20% carbon loss at the weld interface when aged up to 20 years. Based on the findings, GTJs with graded regions of 10 mm and 20 mm in length were fabricated for this study.

Reduced Composition Gradient

As shown in Figure 2-2, the CPC gradient produced from a linear change in dilution (i.e. linear composition gradient) is generally the largest at the beginning of the grade, and appreciably decreases (or becomes positive) towards the "pure" filler metal side. Thus, carbon diffusion can be further minimized by simply elongating the grade within this region in order to reduce the concentration gradient, the corresponding CPC gradient, and

the concomitant carbon diffusion. For example, the CPC gradient at 500°C for Inconel 82 (Figure 2-2a) illustrates that a composition of 60% dilution Inconel 82 represents the location where the gradient becomes positive. This composition was chosen to become the new end member of the graded region. Maintaining a linear concentration gradient, the new graded region has a composition from Grade 22 to an end member of 60% dilution Inconel 82 expanded over the same grade length. Figure 2-11 shows the carbon concentration as a function of distance for a GTJ 10 mm in length, aged at 500°C up to 20 years. Figure 2-11a shows the original carbon concentration curve that contained the initial CPC gradient, while Figure 2-11b shows the carbon profile with the revised composition and reduced CPC gradient. Note in Figure 2-11b, the final carbon content is 0.12 weight percent C, which is consistent with 60% dilution Inconel 82. The original end member contained 0.10 weight percent C. These results clearly show a decrease in the CPC gradient results in less carbon depletion prior to the fusion line in the Grade 22 HAZ and less carbon enrichment into the graded region. These results are insightful for future endeavors as they demonstrate how the graded region can be fabricated for the most effective results.

Simulation Results for Fabricated GTJs

The modeling results discussed thus far are useful to understand the effects of temperature on carbon diffusion and provide guidance on the optimal grade length required to reduce carbon diffusion. However, the results to date have assumed a linear composition gradient. In a graded material made with welding and additive manufacturing processes, it is not often recognized that the composition is uniform within each layer, and rather steep composition gradients exist between the layers.[19,39] Figure 2-12 shows the EDS results for

the major alloying elements Fe, Ni, and Cr across the GTJ between Grade 22 (left) and Inconel 82 (right). There is a graded region between the two end members with each layer representing a different composition. This result shows the composition gradient is not linear, and is actually a step function. Thus, the experimentally measured compositions of each layer were averaged to create a revised profile for modeling that consisted of a constant composition for each layer with a 50 μm partially mixed region at each layer interface.

Due to the difficulty of accurately measuring low amounts of carbon, the carbon concentration gradient was calculated through knowledge of the measured dilutions of the major alloying elements.[38] The calculated carbon profile was used for the model, along with the other measured elements, to simulate a GTJ aged up to 8,000 hours at 600°C (matching experimental conditions). Figure 2-13a shows the carbon concentration as a function of distance for the GTJ between Grade 22 and Inconel 82 simulated at 600°C for 8,000 hours. The individual layers are marked between the vertical red lines, and designated as L1 for layer one, L2 for layer two, etc. The as-welded condition (time=0) shows the initial carbon profile as a function of distance throughout the GTJ. The results show that carbon diffusion is locally enhanced between the individual layers at the interfaces, particularly near the Grade 22 side of the GTJ. The carbon diffusion is minimal when x>20 mm. This can be attributed to the FCC phase dominating this region, as carbon is known to diffuse slower through an FCC matrix than in a BCC matrix. This is consistent with the enhanced carbon diffusion in the beginning of the grade where the BCC is the dominate phase. These results indicate that reducing the composition gradient at beginning

of the graded region could further decrease the extent of carbon diffusion expected under the current conditions.

This result can be directly compared to the conventional DMW from Figure 2-4c for identical simulation conditions of 8,000 hours at 600°C. Note that the extent of carbon diffusion is still significantly higher in the conventional DMW when compared to the GTJ with the step function composition. Carbon enriched regions reach up to 1.2 weight percent C in the DMW, but only reach about 0.2 weight percent in the GTJ. Thus, even though carbon diffusion is enhanced between the layers within the GTJ, the extent of the depletion and enrichment is still an order of magnitude lower than the DMW.

Simulations were also conducted to calculate the stable phases throughout the GTJ with the stepped composition profile. Figure 2-13b shows the phase fraction as a function of distance between Grade 22 and Inconel 82 aged for 2,000 hours at 600°C. BCC is the dominant phase in the beginning of the grade, and FCC dominates as the composition transitions to Inconel 82. Layers L2-L4 contain both BCC and FCC at 600°C. This transition is not as dramatic as a DMW transition seen in Figure 2-3b, thus the steep changes in phases and corresponding microstructures are reduced. Figure 2-13b also shows the amount of carbides in the system. There is a depletion of $M_{23}C_6$ carbides prior to every interface, with an enrichment into the subsequent layer. Furthermore, Nb carbides become the dominant carbide in the graded region towards Inconel 82.

These results are consistent with experimental observations and Figure 2-14 shows how the carbide content (and associated carbon concentration) vary throughout the graded region. The unaffected base metal is shown in Figure 2-14a for reference. The HAZ adjacent to L1, beginning and end of L1, and beginning of L2 are shown in Figure 2-14b-e

for the GTJ using Inconel 82 aged at 600°C for 4,000 hours. The phase fraction calculates $M_{23}C_6$ carbide depletion and enrichment at the layer interfaces, which matches well with the microstructures in each region. The HAZ depicts a region of a coarse-grained, tempered martensite that is depleted of carbides. This can be attributed to the prolonged aging treatment that caused tempering and carbon diffusion from this region. The beginning of L1 shows a large population of carbides in a fine lath-like structure. EDS on the white particles in the matrix confirmed an enrichment in the Cr content, suggesting the presence of $M_{23}C_6$ chromium carbides. The calculated carbide profile shows a decrease across L1, and a peak into L2. Again, this is consistent with the observed microstructure features. The end of L1 shows a coarse structure depleted in carbides (compared to the beginning of the layer), and a significant change in microstructure into L2. There is a secondary phase that forms at the initiation of L2 that will be discussed in a later section, however smaller carbides are observed between the matrix and secondary phase that are in good agreement with the simulation.

The discussion thus far has been in reference to the GTJ made between Grade 22 and Inconel 82. However, as stated earlier, three candidate alloys were chosen for this study. Therefore, work that was conducted on the Grade 22-Inconel 82 system was also performed on alloys P87 and 347H. Diffusion simulations were conducted for GTJs involving each candidate filler metal in order to compare differences in diffusion behavior expected from the various filler metals. The summary of simulated carbon diffusion can be seen in Figure 2-15a and 15b, which shows the percent of carbon depletion and enrichment for each layer, respectively. The results indicate P87 to be the most promising candidate

alloy, since the extent of carbon depletion and enrichment near the interfaces are generally the lowest for P87.

Major Phase Analysis

Figure 2-16 shows the microstructures of the first four layers in the GTJ between Grade 22 and Inconel 82. L1 contains a high population of carbides (Figure 2-16a). A secondary constituent forms and increases in volume fraction between L2 and L3, and L4 consists almost entirely of this constituent. The formation of this constituent can be explained through the calculations of phase fraction seen in Figure 2-17. At 600°C (the aging temperature), L1 is ferrite (BCC) with carbides. Austenite (FCC) does not exist in L1 at 600°C, but is increasingly stable at 600°C in L2-L4, shown in Figure 2-17b-17d, respectively. The FCC phase at 600°C will transform to martensite with no change in composition when cooled to room temperature. This was confirmed through SEM imaging of this constituent combined with electron back scatter diffraction, which did not detect austenite in the beginning layers where this constituent was present. Figure 2-18a and 18b show the calculated and measured compositions for the major alloying elements in the FCC and BCC phases, respectively. As shown, the calculated composition of Ni enriched FCC at 600°C is in excellent agreement with the room temperature EDS measurements on the secondary phase. The as-welded microstructure did not contain this Ni-rich martensitic constituent. Thus, aging the GTJ at 600°C will result in portions of the sample transforming to austenite that, upon cooling, transform to Ni-rich martensitic.

Conclusions

Thermodynamic and diffusion simulations were conducted to understand phase stability and carbon diffusion behavior in DMWs and GTJs. The following conclusions can be drawn from this work.

1. The chemical potential gradient and associated extent of carbon diffusion associated with joining dissimilar alloys can be reduced by simply extending the grade length within the region of the grade where the CPC gradient is negative.
2. For GTJs made with additive manufacturing processes that involve multiple layers of constant compositions (i.e. stepped compositions), enhanced carbon diffusion is expected at the layer interfaces due to locally high CPC gradients. However, the extent of carbon diffusion near the layer interfaces within such GTJs is still expected to be significantly less than that of conventional DMWs.
3. The reduction of carbon diffusion (in the HAZ of Grade 22) in DMWs using Ni-base filler metals is attributed to the CPC "well" located in the PMZ. This "well" causes a pile-up effect that restricts carbon diffusion. The "well" is not present in the DMW using 347H, therefore the carbon content decreases in the HAZ with aging.
4. A portion of the GTJs will transform to FCC austenite during aging at 600°C. This FCC phase then transforms to martensite with no change in composition during cooling to room temperature.
5. Based on carbon diffusion calculations that simulate local discontinuities in the CPC gradient between individual layers associated with stepped concentration changes in GTJs, alloy P87 is the most promising candidate filler metal. The P87

generally exhibited the lowest amount of carbon depletion and enrichment near the interfaces.

References

1. Klueh, R.L., King, J.F. Austenitic Stainless Steel-Ferritic Steel Weld Joint Failures. *Weld J*. 1982;(September):302-311.
2. DuPont, J.N. Microstructural evolution and high temperature failure of ferritic to austenitic dissimilar welds. *Int Mater Rev*. 2012;57(4):208-234.
3. Dooley, B., Chang, P.S. The current state of boiler tube failures in fossil plants. *Fuel Energy Abstr*. 2002;43(4):56.
4. Laha, K., Chandravathi, K.S., Rao, K.B.S., Mannan, S.L., Sastry, D.H. An Assessment of Creep Deformation and Fracture Behavior of 2 . 25Cr-1Mo Similar and Dissimilar Weld Joints. *Metall Mater Trans a*. 2001;32A(January):115-124.
5. Lundin, C.D. Dissimilar Metal Welds — Transition Joints Literature Review. *Weld J*. 1982;(Feb):58s-63s.
6. Parker, J.D., Stratford, G.C. Review of factors affecting condition assessment of nickel based transition joints. *Sci Technol Weld Join*. 1999;4(1):29-39.
7. Nath, B. Creep Rupture and Creep Crack Growth Behaviour of Transition Joints. *Weld Technol Energy Appl*. 1982:597-621.
8. Parker, J.D., Stratford, G.C. The high-temperature performance of nickel-based transition joints. I. Deformation behaviour. *Mater Sci Eng A*. 2001;299(1-2):164-173.
9. Parker, J.D., Stratford, G.C. The high-temperature performance of nickel-based transition joints. II. Fracture behaviour. *Mater Sci Eng A*. 2001;299(1-2):174-184.
10. Christoffel, R.J., Curran, M.R. Carbon Migration in Welded Joints at Elevated Temperatures. *Weld J*. 1956;35(9):457s-468s.

11. Porter, D.A., Easterling, K.E., Sherif, M.Y. *Phase Trasformations in Metals and Alloys*. Third. Taylor and Francis Group; 2009.

12. Darken, L.S. Diffusion of carbon in austenite with a discontinuity in composition. *Metall Mater Trans B Process Metall Mater Process Sci*. 1948;41(4):430-438.

13. Eckel, J.F. Diffusion Across Dissimilar Metal Joints. *Weld J*. 1964;43(4):170s-178s.

14. Gittos, M., Gooch, T. The interface below stainless steel and nickel-alloy claddings. *Weld Res Suppl*. 1992:461-472.

15. Sudha, C., Paul, V.T., Terrance, A.L.E., Saroja, S., Vijayalakshmi, M. Microstructure and Microchemistry of Hard Zone in Dissimilar Weldments of Cr-Mo Steels. *Weld J*. 2006;85(April):71s-80s.

16. Anand, R., Sudha, C., Paul, V.T., Saroja, S., Vijayalakshmi, M. Microstructural Changes in Grade 22 Ferritic Steel Clad Successively with Ni-Based and 9Cr Filler Metals. *Suppl to Weld J*. 2010;89(April):65-74.

17. Laha, K., Latha, S., Rao, K.B.S., Mannan, S.L., Sastry, D.H. Comparison of creep behaviour of 2.25Cr–1Mo/9Cr–1Mo dissimilar weld joint with its base and weld metals. *Mater Sci Technol*. 2001;17(10):1265-1272.

18. Brentrup, G.J., DuPont, J.N., Snowden, B.S., Grenestedt, J.L. Design Considerations of Graded Transition. *Weld J*. 2012;91(September).

19. Sridharan, N., Cakmak, E., Jordan, B. Design, Fabrication, and Characterization of Graded Transition Joints. *Weld J*. 2017;96:295-s-306-s.

20. Andersson, J.O., Helander, T., Hoglund, L., Shi, P.F., Sundman, B. No Title. *Calphad*. 2002;26:273-312.

21. Thermo-Calc Software TCFE7-TCS Steels/Fe-Alloys Database version 7.

22. Thermo-Calc Software Ni-Data-v7 Ni-Alloys Database.

23. DuPont, J.N., Marder, A.R. Dilution in Single Pass Arc Welds.pdf. *Metall Mater Trans B*. 1996;27B:481-489.

24. Borgenstam, A., Höglund, L., Ågren, J., Engström, A. DICTRA, a tool for simulation of diffusional transformations in alloys. *J Phase Equilibria*. 2000;21(3):269-280.

25. Thermo-Calc Software MOB2 TCS Alloy Mobility Database.

26. Klueh, R.L. Heat treatment effects on creep and rupture behavior of annealed 2.25 Cr-1 Mo steel. *Metall Trans A*. 1978;9(11):1591-1598.

27. Parker, J.D., Stratford, G.C. Characterization of microstructures in nickel based transition joints. *J Mater Sci*. 2000;35(16):4099-4107.

28. Zhou, Y., Li, Y., Liu, Y. Precipitation behavior of type 347H heat-resistant austenitic steel during long-term high-temperature aging. *J Mater Res*. 2015;30(23):3642-3652.

29. Banovic, S.W., DuPont, J.N., Marder, A.R. Experimental Evaluation of Fe-Al Claddings in High-Temperature Sulfidizing Environments. *Weld J*. 2001;(March):63-70.

30. Brentrup, G.J., DuPont, J.N. Fabrication and Characterization of Graded Transition Joints for Welding Dissimilar Alloys. *Weld J*. 2013;92(March):72-79.

31. Drouin, D., Couture, A.R., Joly, D., Tastet, X., Aimez, V., Gauvin, R. CASINO A Fast and Easy to use Modeling Tool for Scanning Electron Microscopy and Microanalysis. 2007;29:92-101.

32. DuPont, J.N. *Microstructural Characterization and Modeling of Dissimilar Weld Failures Involving Grade 91*.; 2016.

33. Shingledecker, J., Coleman, K., Siefert, J., Tanzosh, J., Newell, W. High-temperature performance of a new nickel-based filler metal for power generation applications. *EPRI Conf*. 2010.

34. Schaeffler, A.L. Constitution diagram for stainless steel weld metal. *Met Prog*. 1949;56(11):680.

35. Albert, S.K., Gill, T.P.S., Tyagi, A.K., Mannan, S.L., Kulkarni, S.D., Rodriguez, P. Soft Zone Formation in Dissimilar Welds between Two Cr-Mo Steels. *Weld J*. 1997:135-142.

36. King, J.F., Sullivan, M.D., Slaughter, G.M. Development of an Improved Stainless Steel to Ferritic Steel Transition Joint. *Weld J*. 1977;56:354-358.

37. Nicholson, R.D. Effect of aging on interfacial structures of Ni based transition joints. 1984;11(March):115-124.

38. DuPont, J.N., Kusko, C.S. Technical note: Martensite formation in austenitic/ferritic dissimilar alloy welds. *Weld J*. 2007;86(2):51.

39. Suresh, S.S. Modeling and Design of Multi-layered and Graded Materials. *Prog Mater Sci*. 1997;42:243-251.

Appendix

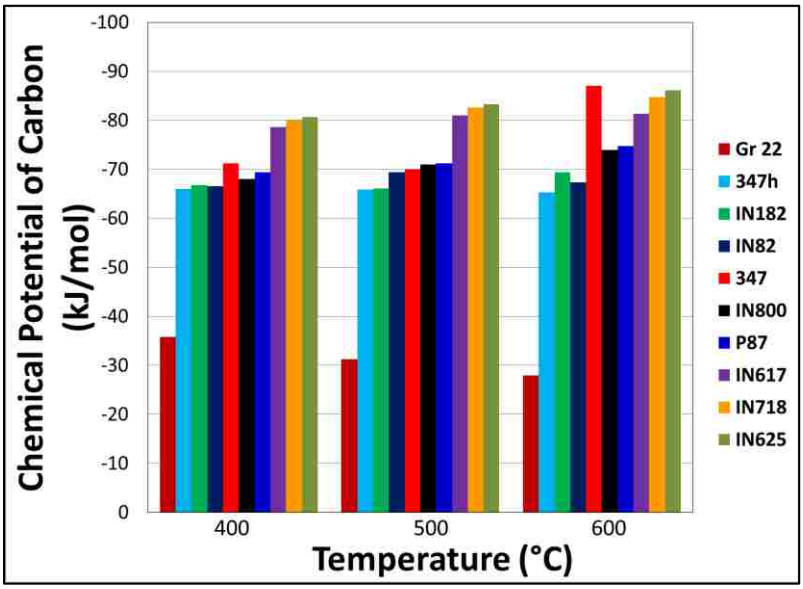

Figure 2-1. Chemical potential of carbon for a number of candidate alloys at various temperatures.

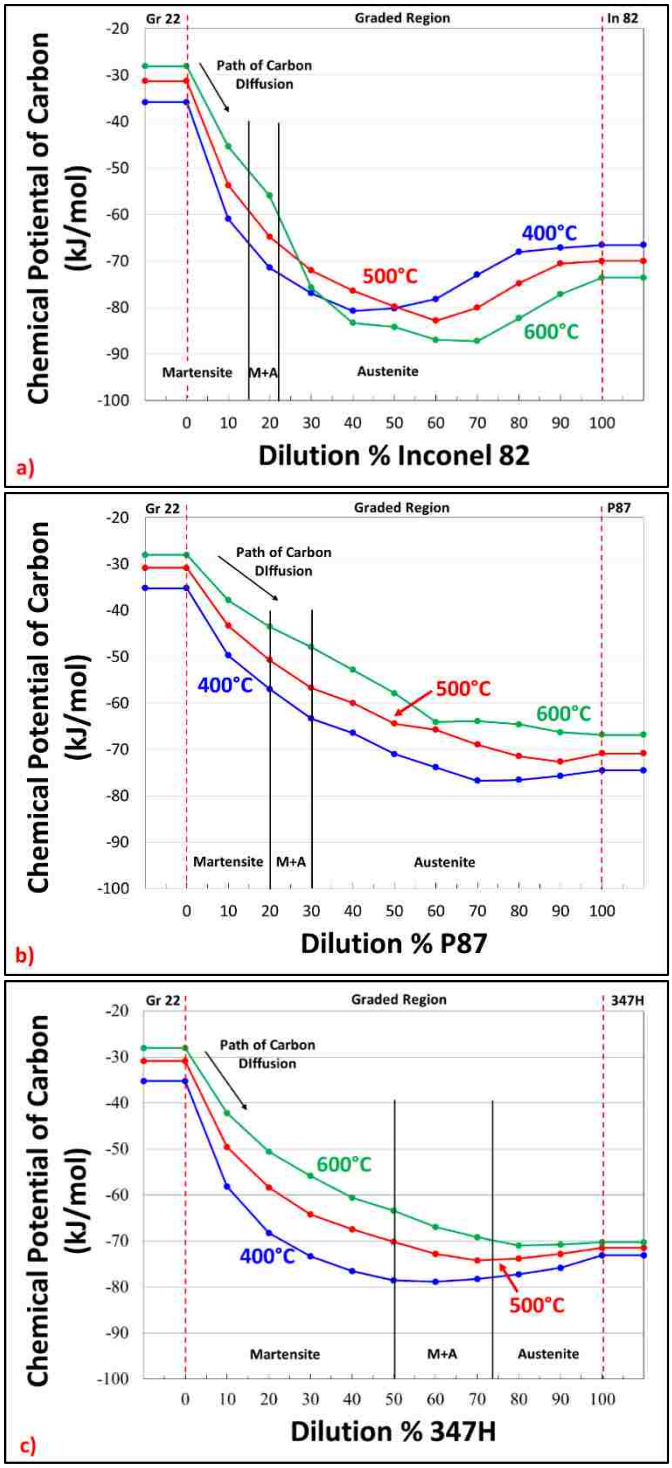

Figure 2-2. Chemical potential of carbon curves as a function of dilution for the three candidate alloys a) Inconel 82, b) P87, and c) 347H.

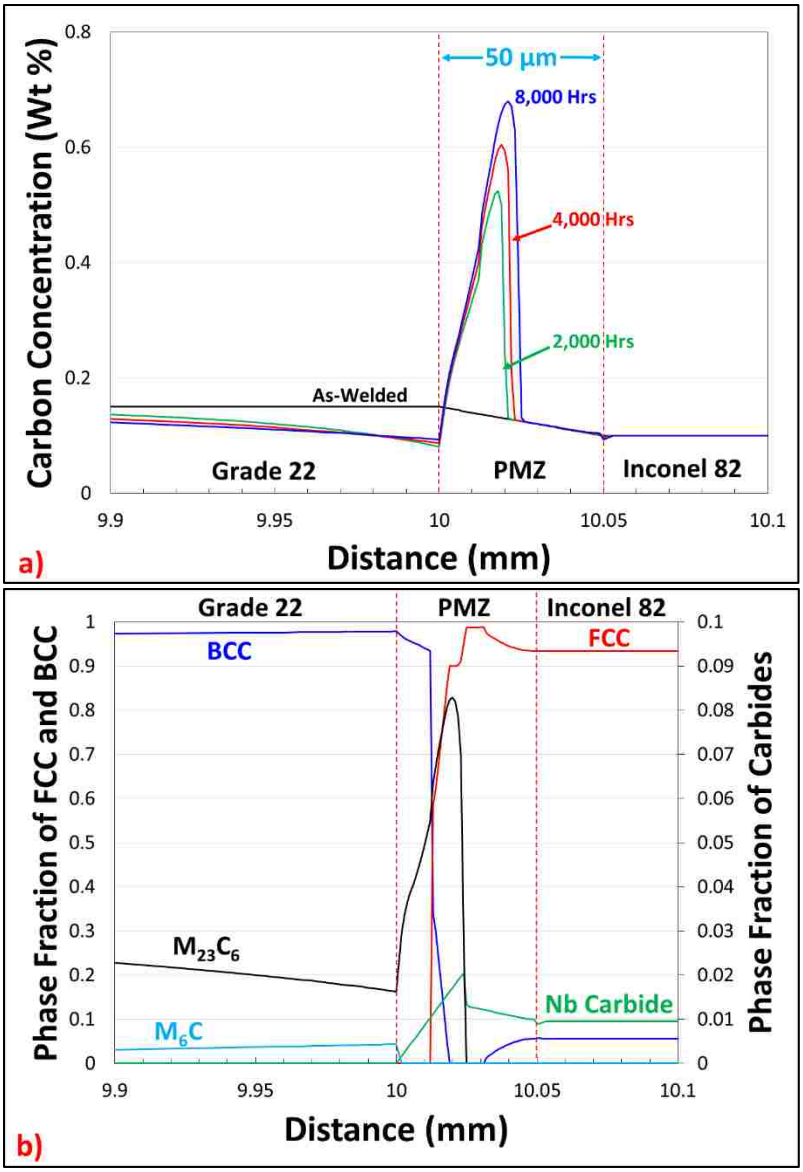

Figure 2-3. Typical a DMW between Grade 22 and Inconel 82 aged at 500°C showing a) carbon concentration profile with a 50 µm partially mixed zone and b) phase fractions plots aged at 500°C after 8,000 hours.

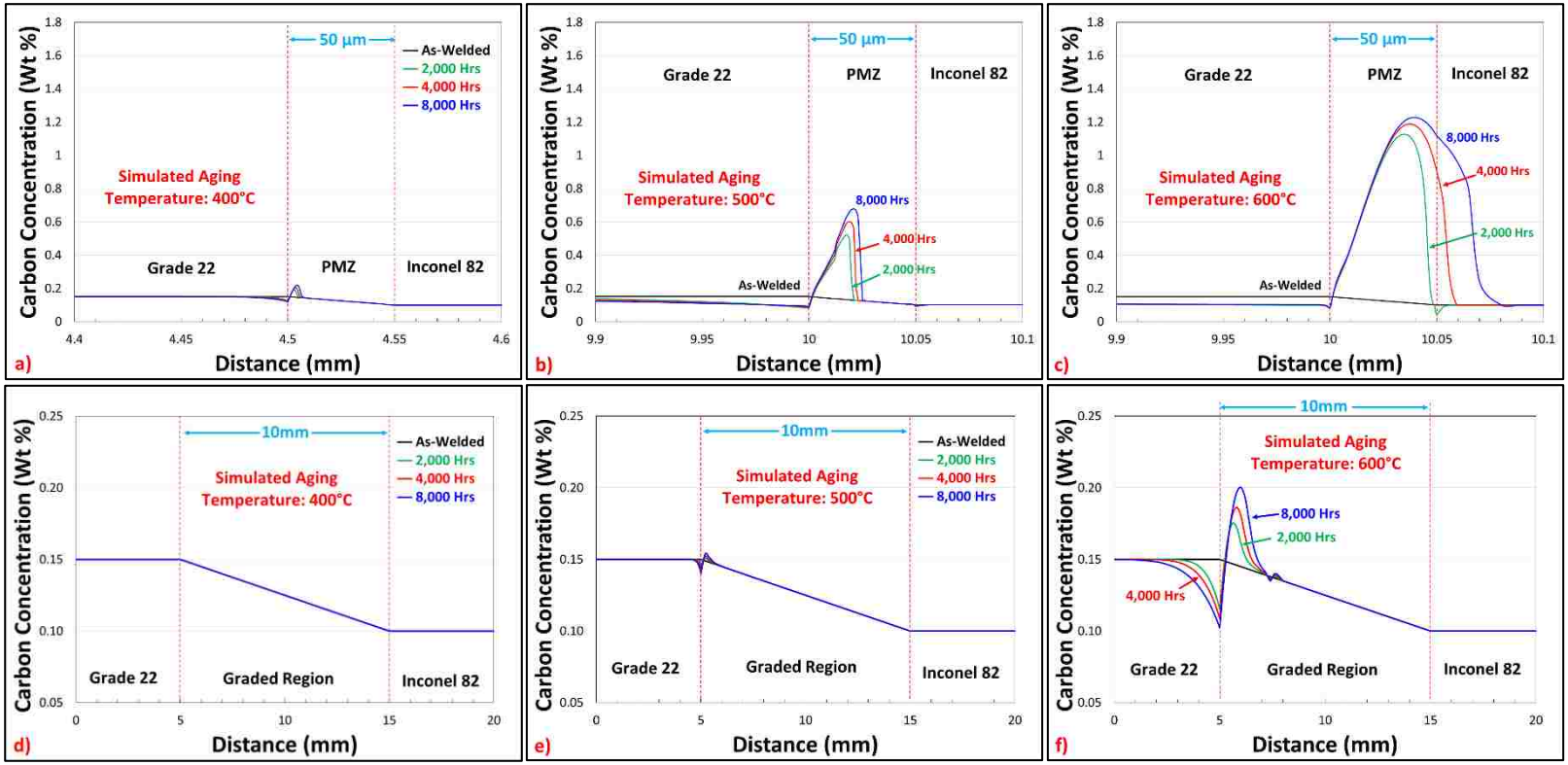
a)
b)
c)
d)
e)
f)
Carbon Concentration (Wt %)
Distance (mm)
50 µm
10mm
As-Welded
2,000 Hrs
4,000 Hrs
8,000 Hrs
Simulated Aging
Temperature: 400°C
Simulated Aging
Temperature: 500°C
Simulated Aging
Temperature: 600°C
Grade 22
PMZ
Inconel 82
Graded Region

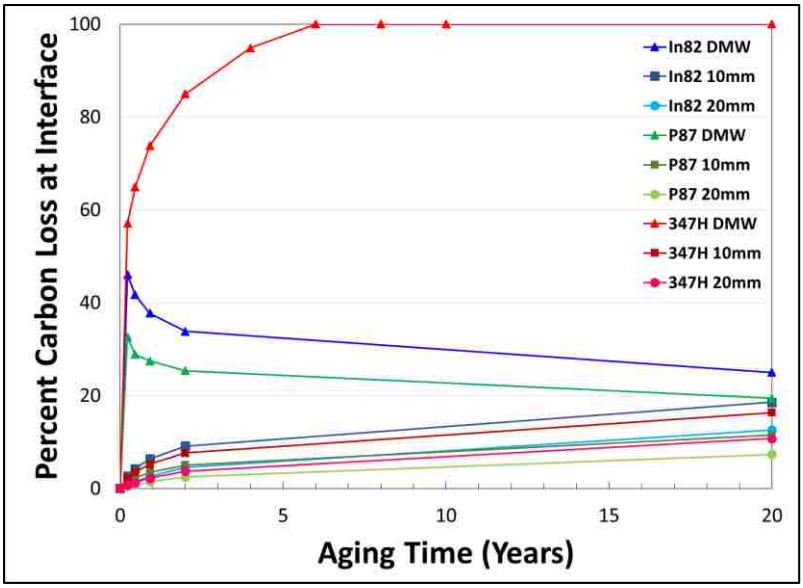

Figure 2-5. Summary for the three candidate alloys aged at 500°C showing the percent Carbon loss at interface up to 20 years.

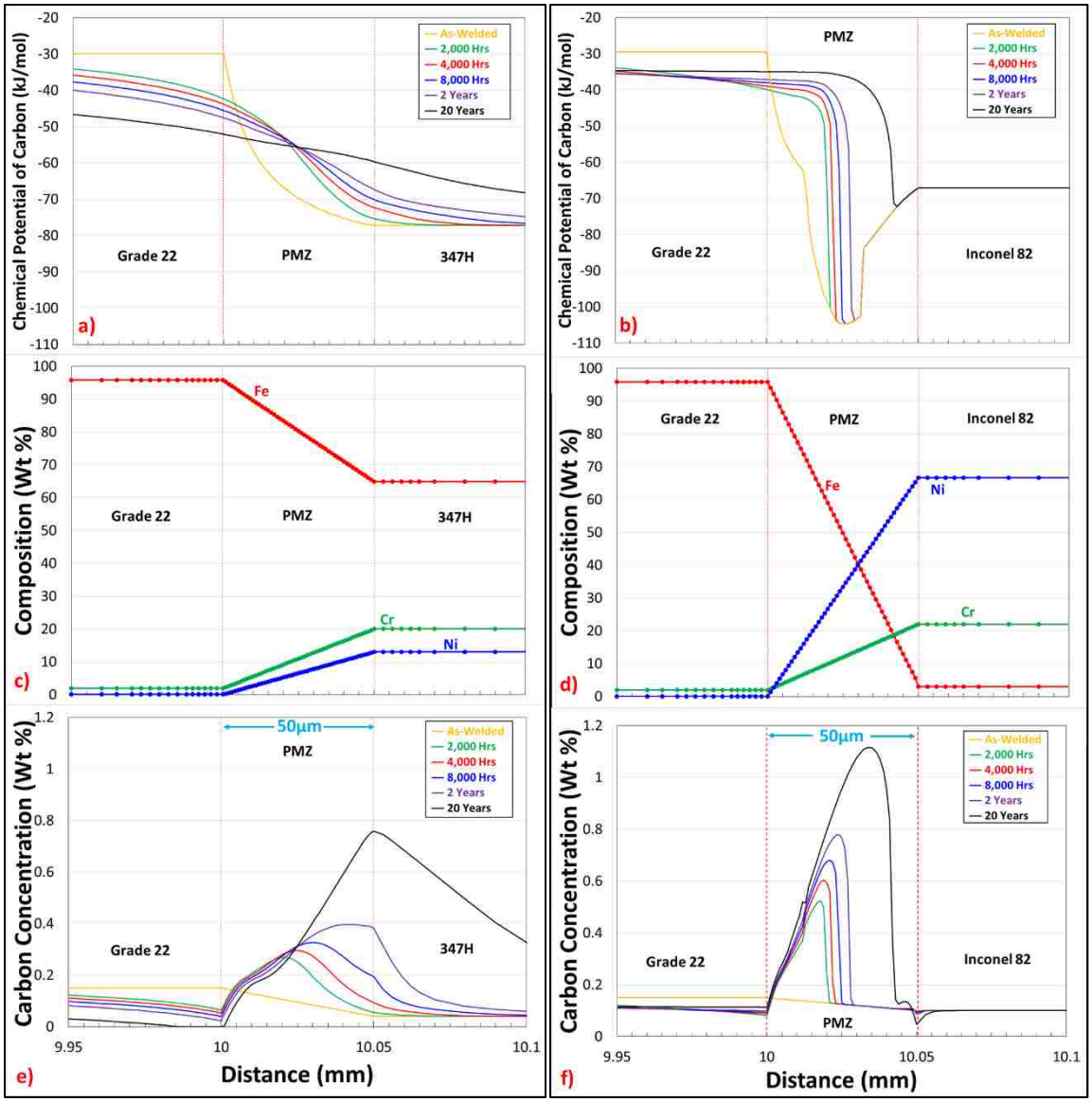

Figure 2-6. Composition, CPC and carbon concentration as a function of distance for 347H (a, c, e) and Inconel 82 (b, d, f), respectively.

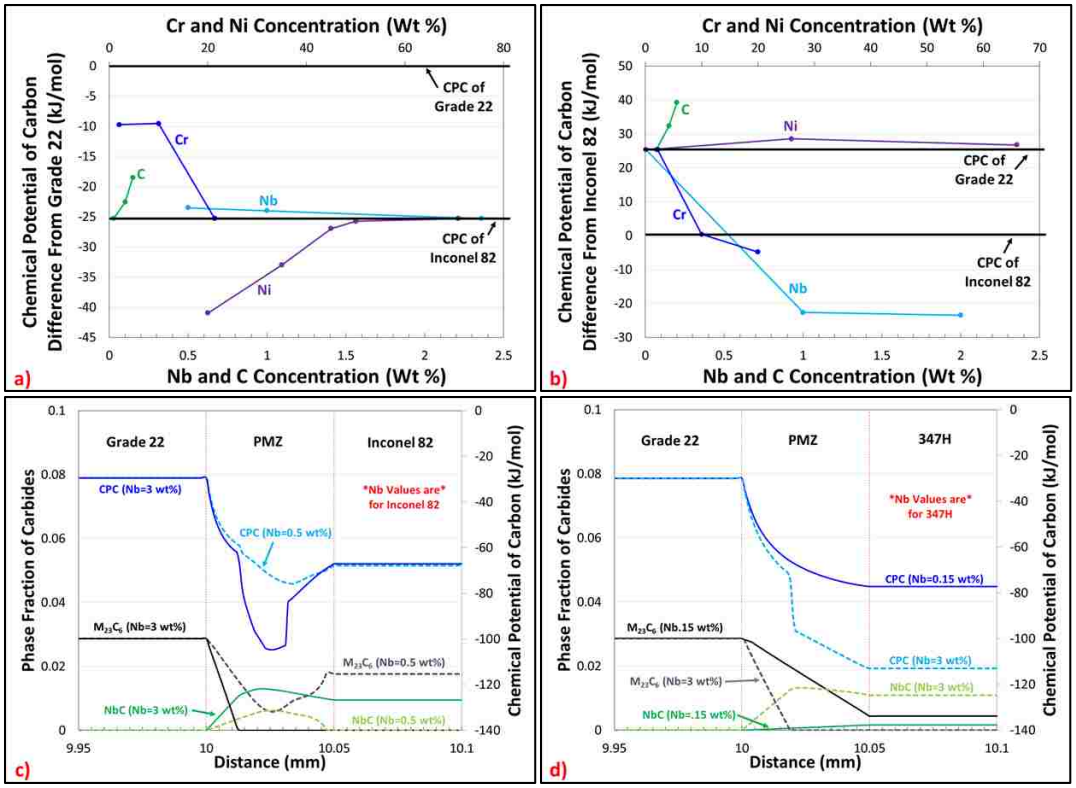

Figure 2-7. Chemical potential of carbon difference from a) Grade 22 and b) Inconel 82 as a function of concentration for Cr, Nb, Ni and C, c) DMW using Inconel 82 varying Nb concentration, and c) DMW using 347H varying Nb concentration.

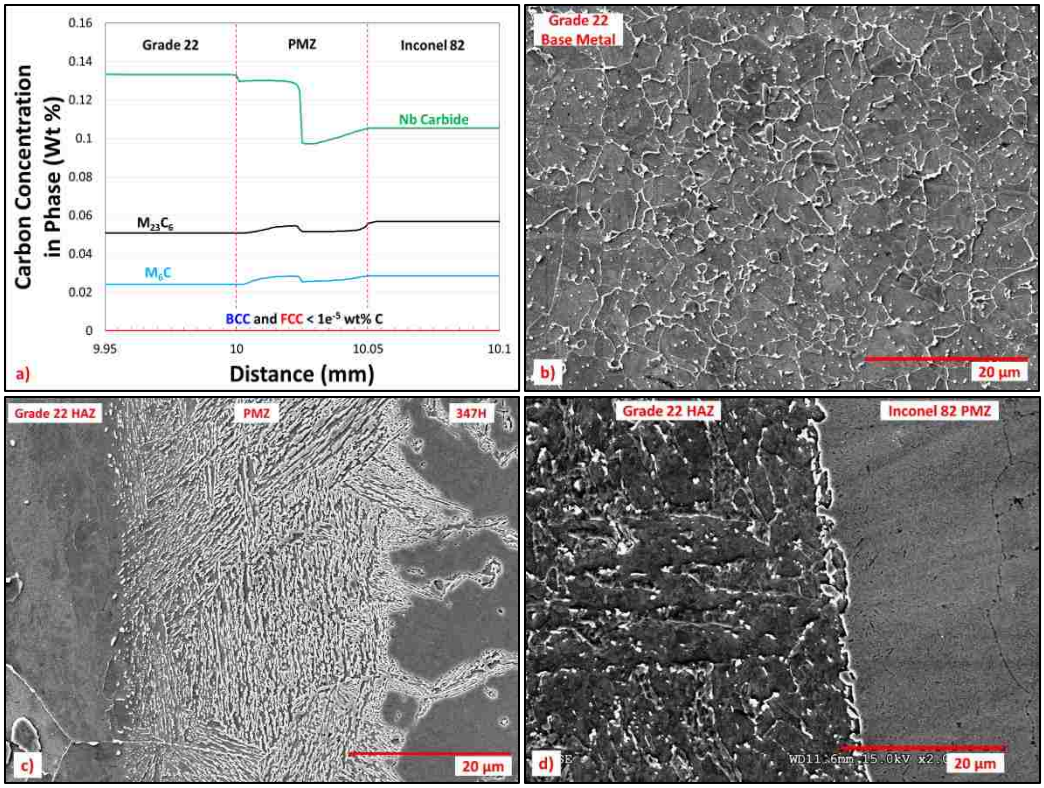

Figure 2-8. a) Calculation of the amount of carbon in each phase for DMW between Grade 22 and Inconel 82 after simulated age at 500°C for 8,000 hours, and photomicrographs showing the extent of carbon diffusion after aging at 600°C for 8,000 hours for b) Grade 22 base metal, c) the interface of the DMW between Grade 22 and 347H and d) interface between Grade 22 and Inconel 82.

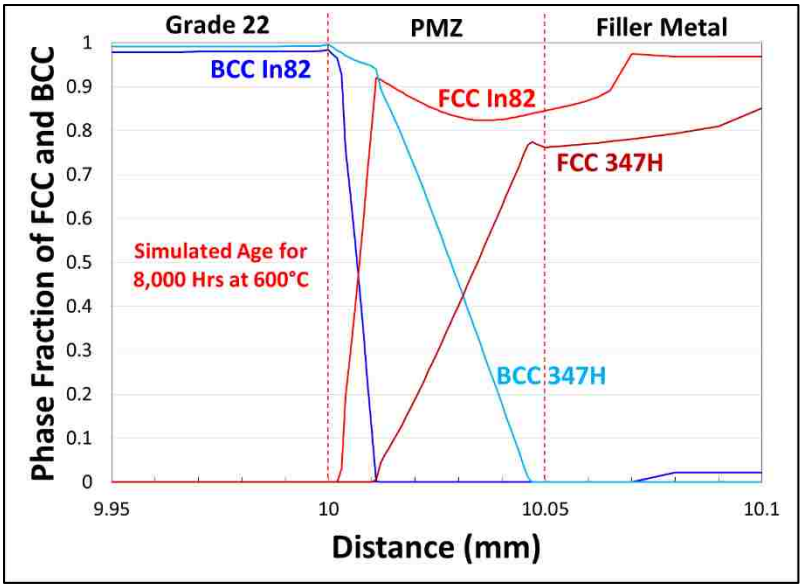

Figure 2-9. Phase fraction of BCC and FCC between Grade 22 and two filler metals Inconel 82 and 347H showing the difference in FCC stability in the PMZ.

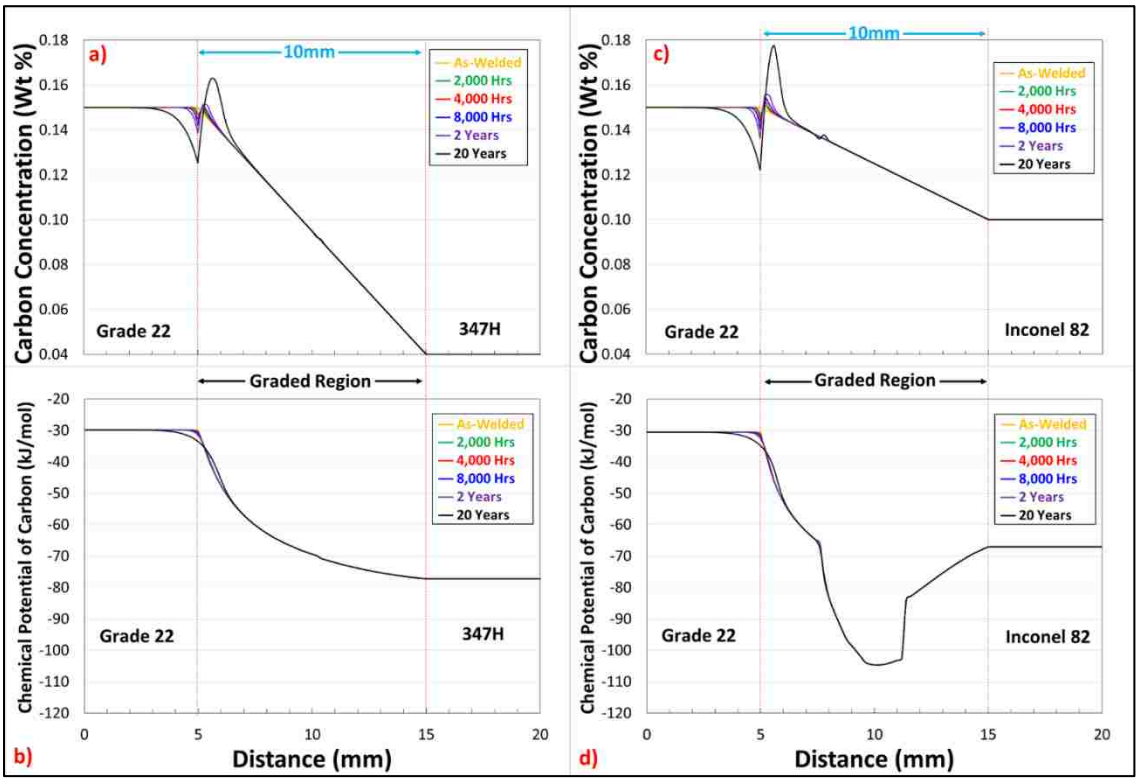

Figure 2-10. Carbon concentration and CPC as a function of distance for a 10 mm GTJ aged at 500°C 347H (a-b) and Inconel 82 (c-d).

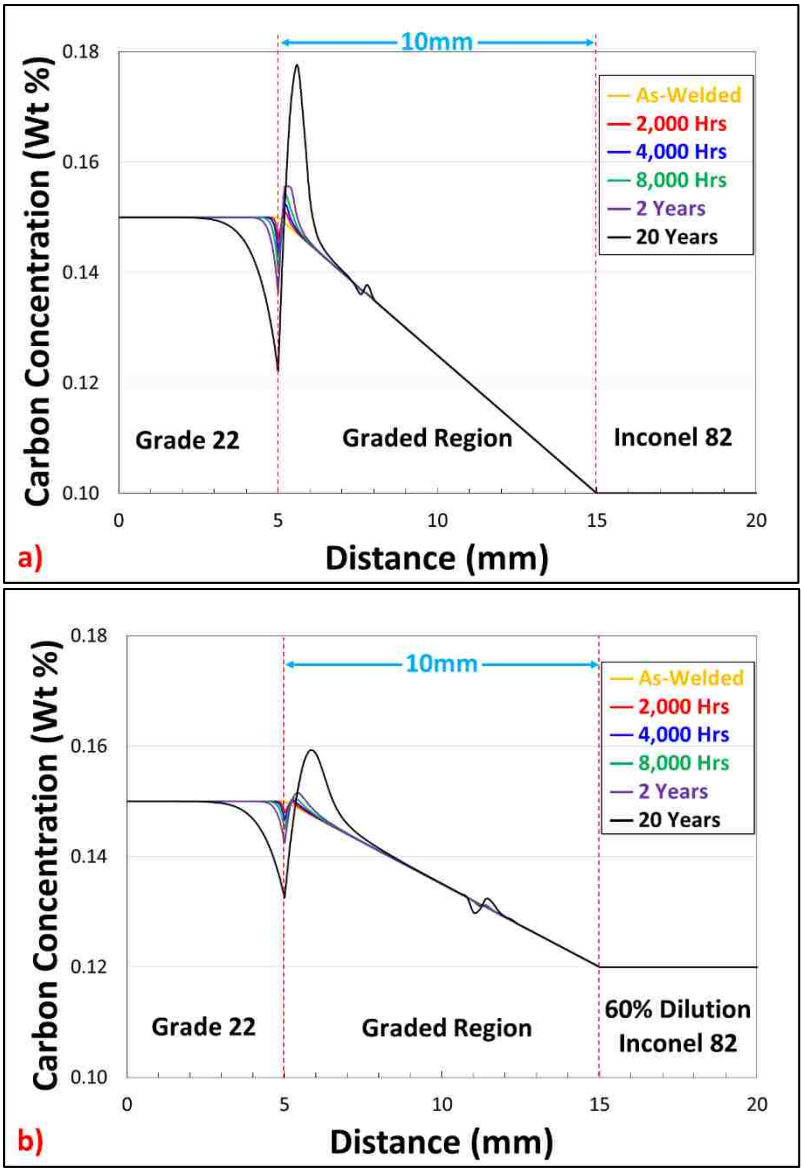

Figure 2-11. Carbon concentration as a function of distance for a 10 mm GTJ aged at 500°C showing a) the original composition gradient and b) the revised composition that reduced the CPC gradient.

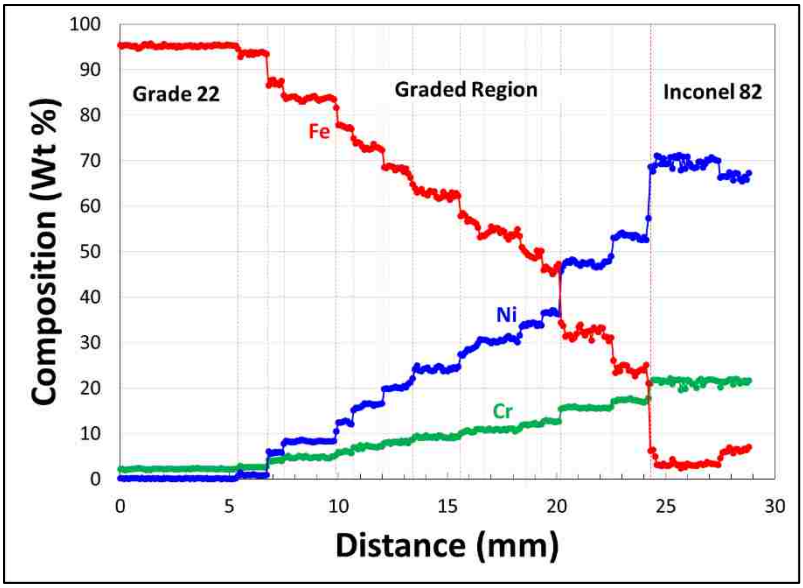

Figure 2-12. EDS trace of a 10 layer GTJ showing the main alloying elements iron, nickel, and chromium in the as-welded condition.

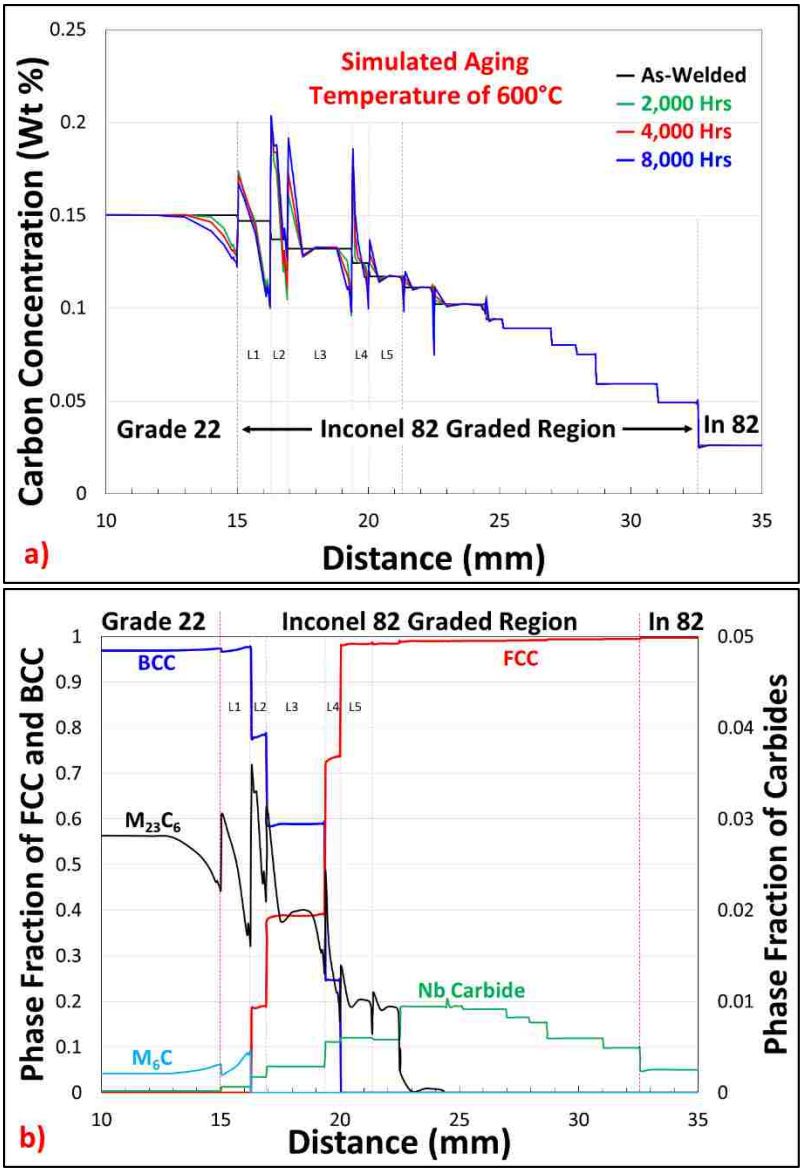

Figure 2-13. Carbon concentration as a function of distance for the GTJ made between Grade 22 and Inconel 82 simulated aged at 600°C up to 8,000 hours and b) phase fraction as a function of distance aged for 8,000 hours at 600°C showing all phases and a magnified view of carbide phases.

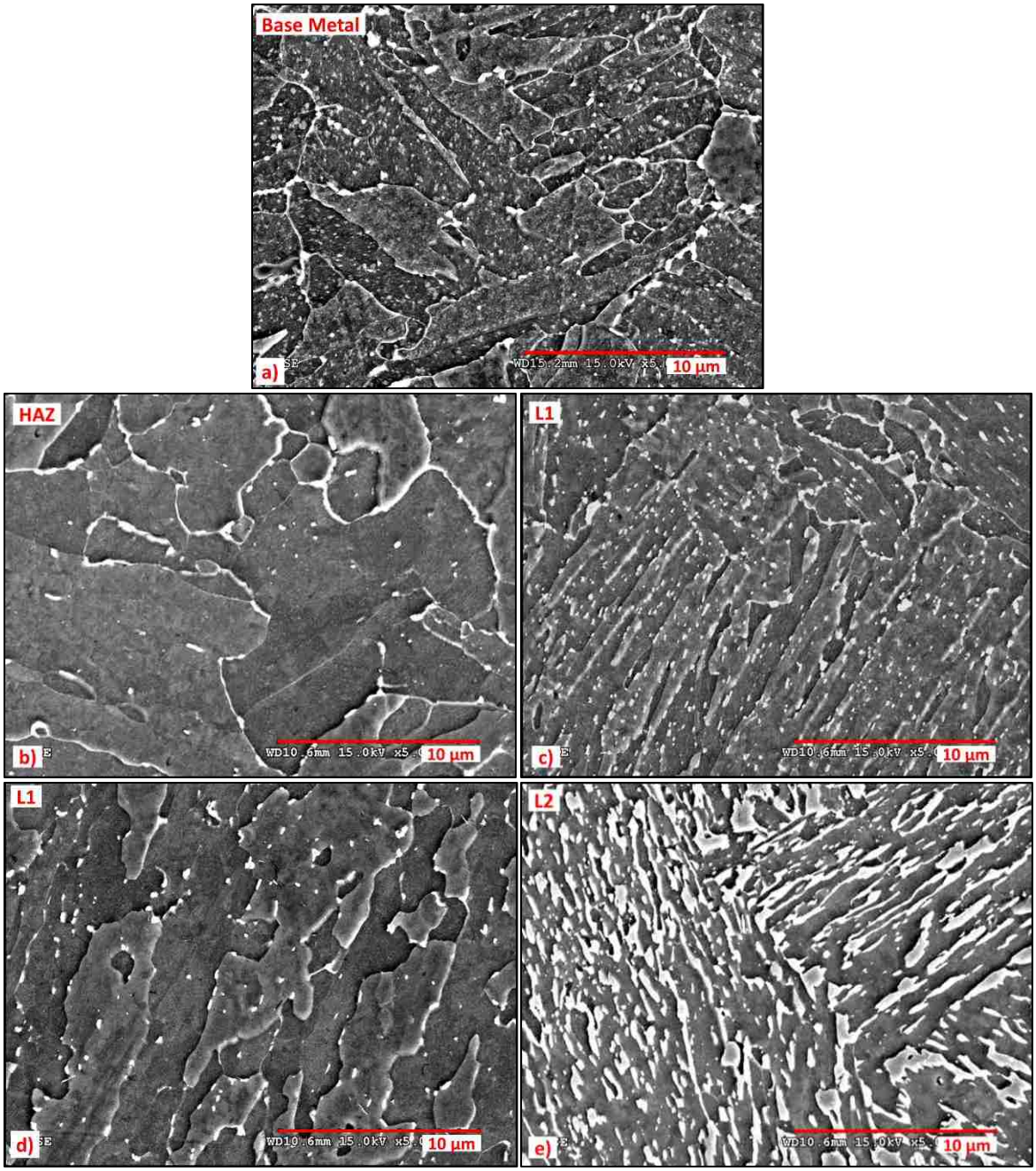

Figure 2-14. SEM photomicrograph of the interfaces in a GTJ made between Grade 22 and Inconel 82 aged for 4,000 hours at 600°C showing a) Base Metal, b) HAZ prior to interface, c) beginning of L1, d) L1/L2 interface, and e) beginning of L2.

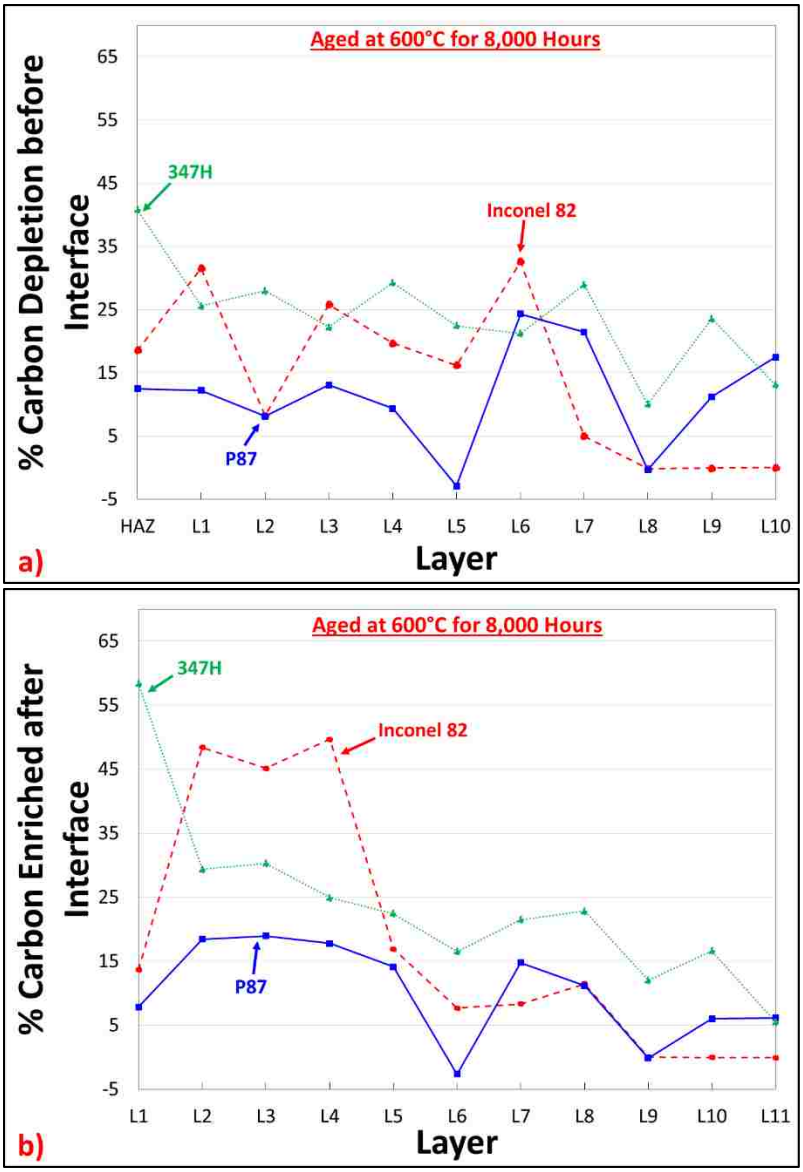

Figure 2-15. Carbon diffusion results for the three filler metals showing a) percent carbon loss before each interface and b) percent carbon gain after each interface.

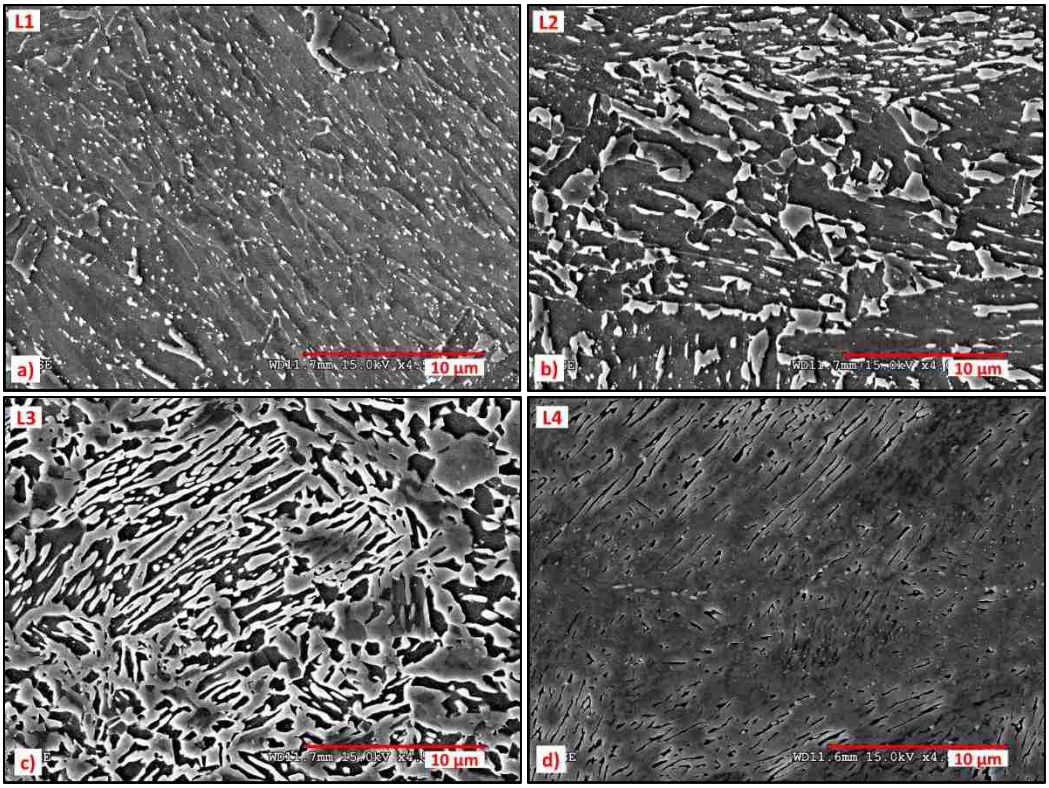

Figure 2-16. SEM photomicrographs of the extent of the secondary constituent in the GTJ using Inconel 82 aged for 2,000 hours at 600°C showing a) layer 1, b) layer 2, c) layer 3, and d) layer 4.

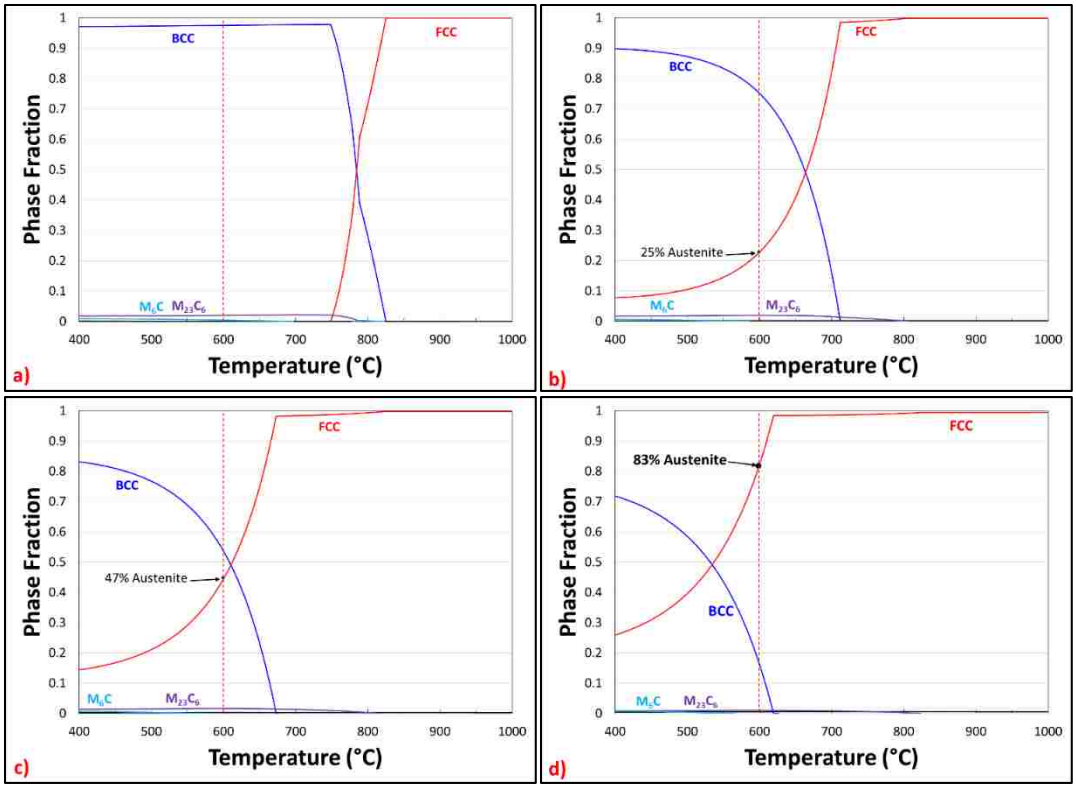

Figure 2-17. Calculated phase fraction as a function of temperatures for in a) layer 1, b) layer 2, c) layer 3, and d) layer 4 for the GTJ using Inconel 82 for a simulated age at 600°C for 2,000 hours.

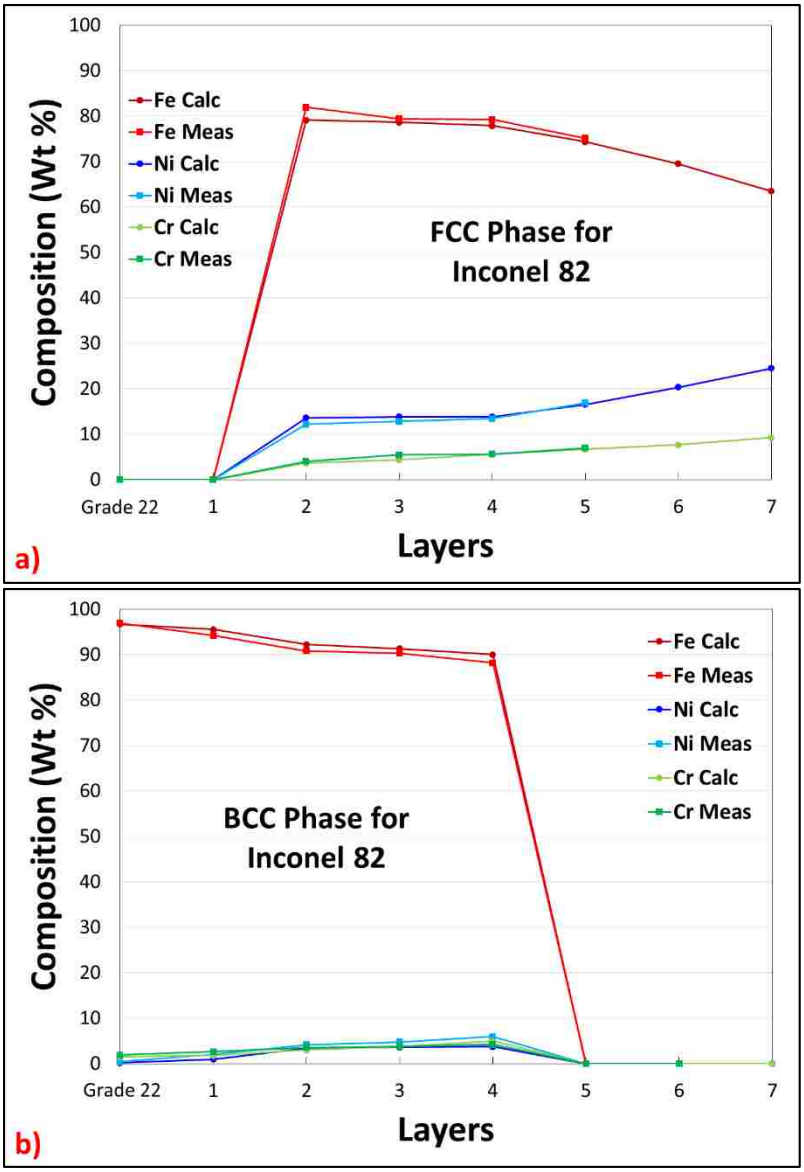

Figure 2-18. The measured and calculated compositions as a function of layers for the austenite phase in the GTJ using Inconel 82.

Tables

Table 2-1. Composition range for alloys used in this study.

	Compositions (Weight %)										
Material	**Fe**	**Al**	**C**	**Cr**	**Cu**	**Mn**	**Mo**	**Nb**	**Ni**	**Si**	**Ti**
Grade 22	Bal.	0.01	0.05 - 0.15	1.9 - 2.6	0.14	0.59	0.87 - 1.13	-	0.05	0.47	-
P87	38 - 42	0.1 - 0.2	0.80 - 0.14	8.5 - 9.5	0.25 max	1.2 -1.8	1.8 -2.2	0.9 -1.4	54 max	0.05 -0.50	0.05 max
347H	Bal.	-	0.04 - 0.10	17 - 20	-	2.00	-	0.15	9 - 13	0.47	-
IN82 (ER NiCr-3)	3 max	-	.1 max	18 - 22	.5 max	2.5 - 3.5	-	2 - 3	67 min	.5 max	.75 max

Table 2-2. Actual compositions used for modeling.

	Compositions used for Model (Weight %)											
Material	**Fe**	**Al**	**C**	**Cr**	**Cu**	**Mn**	**Mo**	**Nb**	**Ni**	**Si**	**Ti**	**Co**
Grade 22	95.8	0.01	0.15	1.90	0.14	0.59	0.87	-	0.05	0.47	-	-
P87	30.0	0.20	0.08	9.50	0.25	1.80	2.20	1.40	54.0	0.50	0.05	-
347H	64.9	-	0.04	20.0	-	1.03	0.16	0.15	13.0	0.75	-	-
Inconel 82	3.00	-	0.08	22.0	0.50	3.50	-	3.00	66.7	0.50	0.75	-
Alloy 800	41.3	0.42	0.09	20.9	0.27	1.03	0.16	0.15	34.7	0.44	0.56	-
347	68.3	-	0.05	19.4	0.13	1.68	0.20	0.63	9.13	0.46	-	-
IN182	10.0	-	0.10	15.0	-	7.25	-	1.75	63.9	1.00	1.00	-
IN617	3.00	1.15	0.10	22.0	0.50	1.00	9.00	-	49.2	1.00	0.60	12.5
IN625	5.00	0.40	0.10	21.5	-	0.50	9.00	3.75	58.9	0.50	0.40	-
IN718	16.4	0.50	0.08	19.0	0.30	0.35	3.10	5.00	53.0	0.35	0.90	1.00

Table 2-3. EDS measurements compared to OES results for the custom standards.

		Elements (Values given in wt. %. N/A = not measured)								
Standards		**Si**	**Cr**	**Mn**	**Fe**	**Co**	**Ni**	**Cu**	**Nb**	**Mo**
Alloy 800	Ave	0.33	22.44	0.95	44.62	0.21	30.89	0.15	0.00	0.42
	OES	0.44	20.97	1.03	41.11	0.07	34.65	0.27	0.15	0.16
347	Ave	0.724	18.208	1.814	67.79	0.288	9.508	0.378	0.756	0.526
	OES	0.55	17.44	1.67	69.93	N/A	9.6	0.47	N/A	0.34
T22	Ave	0.496	2.37	0.568	94.844	0.21	0.068	0.032	N/A	1.41
	OES	0.38	2.19	0.5	Bal	N/A	0.06	0.09	N/A	1.01

Chapter 3 Microstructural Characterization of Graded Transition Joints

Abstract

Carbon diffusion in dissimilar metal welds (DMWs) at elevated temperatures leads to a microstructure that is susceptible to premature failure. Graded transition joints (GTJs) can potentially provide a viable replacement to prolong the service life of these components. The purpose of the current investigation is to fabricate, age and characterize GTJs using three candidate filler metals (Inconel 82, EPRI P87, and 347H) to understand the microstructural evolution at elevated temperatures. Microhardness measurements were performed on the GTJs in the as-welded and aged conditions to understand the initial strength gradients throughout the graded region, and how they evolve with aging time. Additionally, energy dispersive spectrometry was performed to measure the compositional gradients, which were input into thermodynamic and kinetic calculations to understand the carbon diffusion behavior and phase stability. Enhanced carbon diffusion occurred at the layer interfaces in the graded region of the GTJ, which indicated important regions that undergo microstructural evolution. The hardness results also revealed hardness changes at the layer interfaces. The analyzed interfaces demonstrated that carbon diffusion and corresponding carbide redistribution occurred that accounted for the observed hardness gradients. Additionally, the transition from a martensitic to austenitic region was observed in each GTJ that contributed to the hardness variations in the graded region. Finally, the formation of a nickel-rich martensitic constituent was observed in the graded region of all filler metals after aging. This constituent was originally austenite at the aging temperature,

and transformed to martensite with no change in composition upon cooling. The morphologies of the constituent in the three filler metals are presented and discussed.

Introduction

Dissimilar metal welds (DMWs) are critical for design, development, and manufacturing of very high temperature reactors, specifically steam generators in the nuclear industry. Experience has demonstrated that failures of such DMWs can be caused by strain localization attributed to carbon diffusion and thermal stresses due to the chemical potential of carbon (CPC) gradient and the coefficient of thermal expansion (CTE) and mechanical property mismatch.[1,2] Each of these factors is caused by the large variation in composition across the narrow interface between the two dissimilar materials. These failures can occur well before the expected service lifetime, and can cost power plants up to $850,000 per day in lost revenue and repair costs.[3] Potential solutions of DMWs are the design and implementation of graded transition joints (GTJs).

Functionally graded materials have been considered for use in components exposed to high temperature gradients.[4] A typical functionally graded material consists of a ceramic-metal mixture that can be tailored to utilize the advantages of the individual material properties. The ceramic part has good thermal and corrosion resistance capabilities, and the metallic part provides superior fracture toughness and ductility.[5,6] A GTJ is a type of a fully-metallic functionally graded material that consists of two regions of "pure" material on either side of a region where the two materials are mixed in continuously varying proportions over a known distance. This region has a continuous graded composition that is significantly longer than what is reported in DMWs, by as much as three orders of magnitude.[1,7,8] By continuously grading the composition, the sharp changes in both composition and material properties within DMWs are broadened over the length of the grade to mitigate many of the factors that cause premature failure.[9] In the

context of the power generation industry, useful GTJs can be fabricated by multipass welding or additive manufacturing processes.

While GTJs present a potentially viable solution to the problems associated with DMWs, the complex microstructural and property gradients introduce challenges to their effective design and implementation. Design of GTJs using finite element analysis (FEA) tools can potentially expedite the process, provided that the inputs to the model are of sufficient quality so as to produce meaningful outputs. Recent studies have investigated the modeling of functionally graded materials using predictive finite element modeling incorporating 'effective' material properties.[2,4,5] These effective properties are typically estimated using numerical methods such as a simple rule of mixtures, shown in equation 1 where:

$$P_{eff} = fP_A + (1 - f)P_B \qquad (1)$$

where P_{eff} is the effective property, f is the volume fraction, and P_A and P_B are the material properties of material A and B, respectively. Young's modulus, CTE and Poisson's ratio are examples of thermal and mechanical properties that are typically estimated in this manner. This technique requires obtaining only the properties for the two materials, rather than measuring properties at a given location in the graded region. FEA tools such as ANSYS® can be used for modeling external forces and thermal behaviors the materials are likely to experience, thus the effectiveness of the graded material in service can be determined.

Even though the properties of the graded region can potentially be estimated with such techniques, experimental information is still needed to validate these models. Furthermore, it would be very difficult to estimate how the properties change during aging.

One of the important requirements of a GTJ is the stability of the microstructure and properties at an elevated temperature during the service life of the component. It is therefore essential to understand the microstructural evolution of GTJs during long term exposure.

Brentrup and DuPont[10] modeled the carbon diffusion of a DMW and GTJ between Grade 22 and Alloy 800H. A longer grade length significantly reduced the concentration gradient and associated CPC gradient and thus, reduced the extent of carbon diffusion. Transition joints were also fabricated by Sridharan *et. al*.[11] using a blown powder additive manufacturing process to join Grade 22 to 316L with SS410 filler. That study attempted to reduce solidification cracking susceptibility of Inconel 82 during fabrication by grading 316L with an austenitic filler (SS410). Although they successfully fabricated and characterized a GTJ in the as-welded condition, there is still a need to understand the carbon migration and concomitant microstructural evolution that occurs during aging at high temperatures.

While there is a large body of work on the characterization of DMWs, it is unknown how a GTJ will respond to elevated temperatures, and whether it is a suitable replacement for DMWs. The present paper aims to understand the microstructural evolution and localized hardness changes that occur during fabrication and after various aging conditions.

Experimental Procedure

A conventional DMW was fabricated between Grade 22 and Alloy 800H using Inconel 82 filler metal. The gas tungsten arc welding (GTAW) process was used with a single V-Joint configuration. This provided a baseline comparison to the fabricated GTJs.

The GTJ fabrication processes utilized a dual wire GTAW system equipped with two copper cooling plates to contain the liquid weld pool. A substrate of Grade 22 plate 3" x 12" x ½" (0.076 x 0.305 x 0.013 meters)was placed between two copper cooling plates so that the torch and wire feeder assembly deposited metal on the ½" (0.013 m) surface for a maximum travel distance of 12" (0.305 m). The fabrication setup is shown in Figure 3-1a. The feed rates of each filler metal were varied with every deposited layer to meet the required dilution for each layer, and the desired dilution values were calculated from previous modeling studies.[12] Ten layers were deposited using a current of 250A, voltage of 12.5V and travel speed of 1 mm/s. The welding direction was rotated every two passes to avoid weld metal build up at the end members. The ten layers corresponded to ~10 mm graded region, as it was previously determined each layer was ~1 mm under the current welding conditions. The wire feed rates combined for a maximum of 50 in/min (21.167 mm/s). An additional three layers of filler metal were deposited so the graded region avoided affects from joining of 800H extensions. The final product was a three inch substrate of Grade 22, ~10 mm graded region, and a three inch 800H extension joined using Inconel 82 filler metal, as shown in Figure 3-1b. The three filler metals used to fabricate the three GTJs were Inconel 82, P87, and 347H. These candidate filler metals were selected from a wide range of austenitic alloys based on a separate modeling study.[13] The compositions of the materials used in this study can be seen in Table 3-1.

Samples from the as-welded conventional DMW and GTJs were sectioned and prepared using standard metallographic techniques to a final polished state using 0.05 μm colloidal silica for characterization. Compositional line traces using energy dispersive spectrometry (EDS) were conducted on the as-fabricated GTJ samples in the as-polished

condition using the Leo Gemini® 1550 VP scanning electron microscope equipped with an 80mm^2 Oxford® X-MAX silicon drift detector operated at an operating voltage of 15 keV with a 60 μm objective aperture. The remaining weld sections were aged at 600°C up to 8,000 hours (approximately one year) for an accelerated aging treatment to simulate the microstructural evolution expected from service conditions. Samples were removed after 2,000, 4,000 and 8,000 hours and prepared for characterization similar to the as-welded samples.

Microhardness traces were conducted on the as-welded and aged samples in the as-polished condition using a LECO® LM 248AT Vickers microhardness indenter with a 13 second dwell time with 5 and 10g loads for DMWs and GTJs, respectively. A two percent nital solution was used to reveal grain boundaries and carbides in the ferritic material, and a ten percent oxalic acid solution was used to reveal grain boundaries and carbides in the austenitic structures by electrolytic etching at 2V for 5-15 seconds, depending on filler metal.

Secondary electron imaging and X-ray EDS were performed in a Hitachi® 4300SE/N Schottky field emission scanning electron microscope at an operating voltage of 15 keV. Compositions measured from this analysis are standardless and therefore, semi-quantitative. However, the accuracy of this technique was evaluated using commercial alloy “standards” of known chemistry measured by optical emission spectroscopy (OES). Table 3-2 shows the results from EDS alongside the OES results. The EDS measurements show reasonably good agreement with the OES measurements. Therefore, this measurement technique was sufficient enough to identify regions of local enrichment. Monte Carlo simulations using the CASINO® program demonstrated that the X-ray

generation volume was approximately 1 μm^3 under the operating conditions.[14] Thus, results of sub-micron size particles were likely affected by the surrounding matrix material but were still useful for identifying the formation of expected phases. Electron back scattered diffraction (EBSD) measurements were performed at an accelerating voltage of 20 keV and a step size of 0.2 microns across the welded interfaces. Image quality and phase maps were recorded to aid in microstructure characterization.

Thermodynamic and kinetic modeling was conducted on the conventional DMW and the three GTJs. Simulated aging times and temperatures were selected to match the accelerated aging treatment at 600°C. Aging simulations were performed using the DICTRA® software package in conjunction with the MOB2 mobility database.[15,16] The TCFE7 and NI-DATA-V7 databases were used for high iron materials and nickel based alloys, respectively.[17,18] The following phases were allowed to form based on relevant literature for each material: Austenite, ferrite, $M_{23}C_6$, M_6C, and FCC2 (MC carbide phase).[19–22] The length of the graded region was set as 50 μm for DMW calculations. This is a typical distance of the PMZ in a DWM.[1,7,8,23] Composition profiles for the GTJs were chosen from the EDS line trace results utilizing a step function concentration gradient, with individual layer compositions averaged from experimental measurements. Carbon diffusion and phase fraction profiles were extracted from the kinetic simulations for both the DMW and GTJ and were compared to the observations from characterized samples. Additionally, non-equilibrium (Scheil) solidification calculations were performed in for compositional representative of select regions of the GTJs using Thermo-Calc software and the TTNi7 thermodynamic database to assess the compositional gradients during weld

metal solidification. EDS line scans across a series of cellular microstructure in the as-welded condition were conducted to directly compare to the Scheil simulations.

Nanoindentation was conducted using a HYSITRON PI 85 PicoIndenter® using a Berkovich indenter. The indentation data was analyzed using the HYSITRON TriboScan^{TM} nanomechanical data and analysis software package. The testing was performed with a maximum load of 2,000 μN on microstructural features. A 7x7 grid was indented, each indent 5 μm apart. The hardness of individual phases was observed to aid in explaining the microhardness trends.

Results

Microhardness Trends

As-welded condition

Microhardness gradients in the as-welded condition for the conventional DMW and fabricated GTJs using Inconel 82, P87 and 347H are shown in Figure 3-2a-d, respectively. The microhardness and composition are plotted as a function of distance across the PMZ in the DMW, and graded region in the GTJ. Due to the difficulties of accurately measuring carbon, the carbon concentration gradient was estimated from knowledge of the concentration of major elements (measured by EDS) in the manner previously described by Kusko and DuPont.[24] Using the measured values of manganese (Mn), nickel (Ni), chromium (Cr), and molybdenum (Mo), along with estimated values of carbon (C), the variation in martensite start (M_s) temperature across the PMZ and graded regions was also determined and shown in Figure 3-2. This is useful to determine the region where the M_s temperature is below room temperature (T_{RM}), which indicated the material will be

austenitic. The expression used for this calculation was provided by Andrews[25] and shown by equation (2):

$$M_S(°C) = 539 - 423C - 30.4Mn - 17.7Ni - 12.1Cr - 7.5Mo \quad (2)$$

where the composition is in weight percent. The conventional DMW (Figure 3-2a) shows a steep concentration gradient for the three major alloying elements Fe, Ni, and Cr. As expected, the M_s temperature also exhibits a steep gradient across the narrow PMZ. There is a high hardness region in the heat affected zone (HAZ) of Grade 22 prior to the fusion line, with a significant reduction in hardness from 400 HV to 200 HV across the PMZ and into the Inconel 82 weld metal.

The spatial variation in composition, hardness, and M_s temperature are shown for Grade 22/Inconel 82 GTJ in Figure 3-2b. The difference in length scales between Figure 3-2a and 2b must be noted, as the PMZ of the DMW is on the order of microns, whereas the graded region of the GTJ is on the order of millimeters. The primary goal of GTJs is to eliminate the sharp changes in composition and property gradients. Although the GTJs do exhibit changes in hardness, these changes occur over much greater distances when compared to the conventional DMW. The composition changes gradually throughout the graded region, and is in the form of a step-function, as each layer consists of a constant composition. The base metal hardness starts around 200 HV, and increases throughout the HAZ and into the graded region. The hardness increases throughout the graded region and then decreases slightly in Layer 4. Layer 4 exhibits a larger reduction in hardness from 400 HV to 200 HV. (Note: layers will be labeled “L” followed by the layer number. i.e. layer 1 is L1.) Beyond L4, the hardness remains essentially constant until the end of the

graded region, and experiences a slight increase as it transitions to the Inconel 82 weld metal.

The P87 and 347H GTJs (Figure 3-2c-d) follows similar trends to that of Inconel 82. The region of mixed hardness in the P87 GTJ is L6 (opposed to L4 in Inconel 82) and in L10 for the 347H GTJ. Furthermore, the concentration gradient is less severe in the 347H GTJ than the other two filler metals because 347H is an iron-base filler metal, whereas Inconel 82 and P87 are nickel-base materials.

Aged Condition

The microhardness gradients in the aged conditions for the conventional DMW and GTJs are shown in Figure 3-3a-d. The conventional DMW in Figure 3-3a shows a locally soft region prior to the fusion line for all aged conditions, and hardness peak in the Inconel 82 weld metal. This can be directly compared to the microhardness gradients shown in Figure 3-3b for the Inconel 82 GTJ. The Inconel 82 GTJ also exhibits a reduction in hardness in the HAZ from the as-welded condition, but the extent of softening near the HAZ/L1 interface is significantly reduced. For all aged conditions, there is an overall decrease in hardness from the as-welded condition, but still an increase in hardness in each layer as the grade transitions to complete austenite. Layer 5 contains mixed hardness, followed by a reduction to 200 HV in L6 for the 2,000 and 4,000 hour aged conditions. After aging for 8,000 hours, the hardness is higher (in L6 through the Inconel 82 weld metal) than the 2,000 hour aged condition. Similar trends are shown in the P87 GTJ (Figure 3-3c), except the hardness does not increase after 8,000 hours aging, and the mixed hardness layer is L6 (opposed to L5 in the Inconel 82 GTJ). The 347H GTJ (Figure 3-3d)

also exhibits similar hardness trends, only over a larger region, and does not exhibit the sharp decrease in hardness like Inconel 82 and P87 in L6 and L7, respectively. Instead, the reduction in hardness occurs beyond L10 (~x=25mm), and increases after aging, essentially eliminating sharp hardness gradients seen in the Inconel 82 and P87 GTJs.

Thermodynamic and Kinetic Modeling

The calculated carbon concentration and phase fraction as a function of distance at the simulated aging temperature of 600°C for up to 8,000 hours is shown for the conventional DMW (Figure 3-4a-b) and the Inconel 82 GTJ (Figure 3-4c-d), respectively. (Note the large difference in both concentration and distance scales between the DMW and GTJ). The conventional DMW shows a carbon depleted region prior to the fusion line (x=10mm) and a carbon enriched region in the PMZ for all aging conditions. The phase fraction at 600°C in Figure 3-4b shows three stable carbides, a molybdenum rich carbide (M_6C), chromium rich carbide ($M_{23}C_6$) and niobium rich carbide (NbC). The NbC is stable in Inconel 82 due to the higher Nb content in the filler metal. There is a sharp transition from BCC to FCC, which is attributed to the steep concentration gradients between the two materials. These figures can be directly compared to the GTJ between Grade 22 and Inconel 82 showing the carbon concentration and phase fraction in Figure 3-4c-d, respectively. The initial carbon concentration profile (Figure 3-4c) exhibits a slight, local reduction at the interfaces associated with the change in composition of each layer. After 8,000 hours, there is considerable carbon depletion and enrichment at the first four layer interfaces. This is insightful, as it demonstrates the location of significant microstructural evolution – in the beginning of the grade, and at the layer interfaces. While carbon diffusion

occurs in the GTJ, the extent of the enriched regions are less than 0.17 weight percent C, as opposed to 0.70 weight percent C in the DMW PMZ. This is expected, as an increase in grade length and corresponding decrease in the CPC gradient (discussed below) results in a lower driving force for carbon diffusion.

Localized variations in the BCC and FCC phase distribution occur through the first five layers of the graded region (Figure 3-4d). The $M_{23}C_6$ carbide fraction follows the trend of the carbon concentration. This is expected, as it was previously demonstrated that most of the carbon in the system resides primarily in the carbides.[13] Similar to the DMW, the Nb carbide is stable throughout the FCC range until the end of the graded region and also follows the carbon concentration behavior once the $M_{23}C_6$ carbide is no longer stable.

The carbon concentration and phase fraction as a function of distance is shown for the P87 GTJ (Figure 3-5a-b) and the 347H GTJ (Figure 3-5c-d), respectively. Similar trends are observed for these GTJs. Carbon diffusion occurs at the layer interfaces, and the extent of diffusion increases with increased aging time. A major difference between these filler metals and Inconel 82 is that the carbon depletion and enrichment at the layer interfaces continues further into the graded region (Figure 3-5a and c). The phase fraction for P87 GTJ (Figure 3-5b) shows that all three carbides are stable throughout the graded region. The phase fraction for the 347H GTJ shows a gradual transition (in the form of a step function) from BCC to FCC, attributed to the lower concentration gradient as compared to the Ni-base filler metals. Additionally, the $M_{23}C_6$ phase fraction shows significant depletion and enrichment at the layer interfaces, with NbC stable throughout the entire 347H graded region.

The carbon concentration is lower in Grade 22 than in P87, resulting in a positive concentration gradient in the P87 graded region (Figure 3-5a). In a binary system, carbon will diffuse from high to low concentrations.[26,27] However, in a multicomponent system, the CPC gradient is the driving force for carbon diffusion. The CPC gradient is shown in the as-welded and aged conditions for the conventional DMW, Inconel 82, P87, and 347H GTJs in Figure 3-6a-d, respectively. In the as-welded condition, the conventional DMW has a steep CPC gradient after the fusion line that drives the carbon to diffuse from Grade 22, down the CPC gradient, and into the PMZ. In the aged condition, the CPC discontinuity that existed at the fusion line in the as-welded condition is alleviated due to carbon diffusion. The three GTJs show a step function in the negative CPC gradient for all conditions. Even though the P87 GTJ has a positive carbon concentration gradient, it exhibits a negative CPC gradient across the graded region, as shown in Figure 3-6c. This results in carbon to diffuse up the concentration gradient, a phenomenon known as "uphill" diffusion.[7,8,26,28,29]

Microstructure Characterization

Photomicrographs were acquired in the Inconel 82 GTJ aged for 4,000 hours at locations of significant microstructural evolution seen from the hardness and modeling results, and shown in Figure 3-7. The HAZ directly adjacent to the interface, and the beginning of L1 is shown in Figure 3-7a-b, respectively. The HAZ was originally martensitic in the as-welded condition. Upon aging, the combination of tempering and carbon diffusion resulted in a microstructure depleted of carbides, as shown in Figure 3-7a. The microstructure in L1 adjacent to the HAZ/L1 interfaces is comprised of fine lath

martensite populated by carbides, which were determined to be Cr rich. Figure 3-7c shows a microstructure at the end of L1 that is somewhat similar to Figure 3-7, however the population of carbides is reduced and a courser, lath martensite is observed. Finally, the microstructure in L2 (Figure 3-7d) shows in increase in carbide content, and the formation of a secondary constituent. Identical microstructural trends were observed in GTJs made with P87 and 347H filler metal.

Figure 3-8a-b shows EBSD phase maps overlaid with image quality maps of the layer interfaces where the BCC/FCC transition occurs in GTJs using Inconel 82 and P87, respectively. (EBSD results shown here do not differentiate between BCC ferrite, BCC bainite, and BCT martensite. Thus, for simplicity, the phase map is shown for BCC ferrite and FCC austenite.) All samples were examined in the 2,000 hour aged condition. The phase maps are shown for the L4/L5 and L5/L6 interfaces for the Inconel 82 GTJ. Layer 4 consists of all BCC, and L5 shows the initial formation of austenite. Beyond the L5/L6 interface, only FCC is stable. Similar results are shown in Figure 3-8b for the P87 GTJ, except the interfaces between L6/L7 and L7/L8 were investigated. Layer 7 represents the region of mixed BCC/FCC, with L8 consisting of all FCC. Figure 3-8c represents four regions throughout the 347H GTJ were the martensite/austenite transition occurs. Layer 9 consists of all BCC, and L10 has a small amount of FCC in a BCC matrix. Layers 11 and 12 exhibit increasing amounts of the FCC phase. Beyond L12, Inconel 82 was joined to the 800H extension and exhibited all FCC (as confirmed with EBSD).

Layer 7 in the as-welded P87 GTJ was analyzed to understand the cause for the mixed BCC/FCC microstructure. Figure 3-9a shows a light optical image superimposed on an SEM photomicrograph of L7 with hardness indents used as markers for regions of

interest. The dark and light regions, representing cell core and intercellular regions, correspond to the BCC and FCC austenite phases, respectively. Additionally, an EDS line scan (shown by the black arrow in Figure 3-9a) was conducted across the region to understand the elemental distribution that could be attributed to the stability of the FCC phase. The results of the EDS line scan are presented in Figure 3-9b showing only Fe, Cr, Ni, C, and Mo (other elements were analyzed but not included). The analysis of carbon was calculated by considering a constant carbon concentration of L7 (0.091 weight percent). Next, the EDS trace was subjected to a simulated weld thermal cycle from DICTRA. Due to the alloying element segregation and corresponding CPC gradient, the carbon will diffuse to the cell core, as shown in Figure 3-9b. The trace initiated in an intercellular region that is depleted in Fe, and enriched in the remaining measured elements. Conversely, the cell core is enriched in Fe and depleted in the remaining elements. Figure 3-9c-d show results from the solidification simulation for this layer composition. For this composition profile shown in Figure 3-9d, the cell core is the initial solidification region (far left on figure), with the intercellular region solidifying last. The calculated distribution of the elements shown is in good agreement with the measured elements, as Fe is depleted in the intercellular region when the other elements become enriched.

Evaluation of Ni-rich Constituent

Briefly mentioned above (in Figure 3-7d) was the formation of a secondary constituent observed in all three GTJs. An example of this is shown in Figure 3-10a-d that represents L2 through L5 in the P87 GTJ aged for 8,000 hours, respectively. The constituent is in the form of elongated particles in L2 and L3 (Figure 3-10a-b) that increases

in volume fraction with increasing layer. The calculated phase fraction as a function of temperature for the P87 GTJ is shown in Figure 3-11a-d for L2-L4, respectively. Paying specific attention to 600°C, the austenite that forms during aging increases in phase fraction with increasing layer, going from 12 percent FCC in L2 (Figure 3-11a) to 76 percent FCC in L5 (Figure 3-11d). The austenite that exists at 600°C will also transform to martensite without a change in composition when cooled to $T_{RM,}$ thus accounting for the presence of this martensite constituent within the GTJs after aging.[30] Also labeled on the plots are the "Ac3" temperatures, which are designated as the location where BCC completely dissolves upon heating. As shown, increasing layers exhibit progressively lower Ac3 temperatures, ranging from 734°C in L2 (Figure 3-11a) to 625°C in L5 (Figure 3-11d). It must be recognized that these are under equilibrium conditions. The heating rates experienced during welding are significantly faster than equilibrium and therefore, it is expected for these temperatures to be higher.[31] Additionally, the accuracy of ThermoCalc at lower temperatures is limited due to the insufficient low temperature data available from the databases used for the models. Thus, the trends are more important than the actual Ac3 values. This will be discussed further in the next section. Figure 3-12a shows the calculated composition of the FCC phase at 600°C directly compared to the measured composition of the martensite constituent. This constituent is Ni rich at T_{RM} and is in very good agreement with the calculated composition of the austenite phase at 600°C. Similarly, Figure 3-12b shows very good agreement between the measured matrix and calculated BCC phase compositions.

The morphology of the Ni rich martensite was different between filler metals. This is shown in Figure 3-13 where the Ni-rich martensite is observed in the 347H GTJ. The

Ni-rich martensite has a different morphology than that observed in the GTJs using Inconel 82 and P87 (see Figure 3-7d and Figure 3-10b for comparison). The martensite morphology in Inconel 82 and P87 GTJs is rod-like, whereas the martensite in the 347H GTJ exhibits a blocky morphology.

Discussion

As-Welded Microstructures

The analysis of the as-welded microstructures is summarized in Figure 3-2 with the combination of hardness, composition, and M_s temperature. The conventional DMW (Figure 3-2a) shows a high hardness in the HAZ. This is attributed to martensite formation during fabrication from the high cooling rates associated with welding. Directly after the HAZ, the GTJs exhibit increased hardness with each layer (i.e., before the fully austenitic region is reached). This hardness variation is associated with several factors that are all related to the variation in composition, including changes in both the M_s and Ac3 temperatures, along with solid solution strengthening. The increase in alloying elements along the grade suppresses the M_s temperature (Figure 3-2b-d). If martensite forms at an elevated temperature (i.e., the M_s temperature is relatively high), then significant auto-tempering can occur during cooling to T_{RM}. Therefore, the layers with higher M_s temperatures will experience a larger degree of auto-tempering, thus lowering the hardness. This explains, in part, the lower hardness values observed near the beginning of the grade where the M_s temperature is relatively high.

As demonstrated in Figure 3-11, the Ac3 temperature will also decrease with each additional layer within the graded region (due to the increased alloy content). The relatively

high alloy content within the layers provides high hardenability that, combined with the fast cooling rates from welding, will produce martensite during cooling for any region heated above the Ac3 temperature. Since the Ac3 temperature decreases along the graded region, the amount of material exposed to peak temperatures above Ac3 increases with each additional layer, thus leading to more as-quenched martensite. This effect also partly accounts for the increased hardness along the length of the grade.

The increased hardness can also partly be attributed to solid solution strengthening. For solid solution strengthening, the increase in shear strength with concentration is typically given by an expression of the form:

$$\tau \propto c^{1/2} \qquad (3)$$

where τ represents the strength and *c* represents concentration[32]. Literature has shown this relationship applies to Ni and Cr in martensitic steels.[33,34] The change in hardness as a function of a change in Ni and Cr concentration is shown in Figure 3-14a-b for only increasing Cr and increasing Ni affects, respectively. For a known increase in Cr, the expected measured increase in hardness is plotted for both Inconel 82 and P87 (Figure 3-14a). This is compared to the calculated hardness from literature, accounting for solid solution strengthening from Cr. It is expected for the experimentally measured value to be harder than the calculated hardness increase, as there are most likely other strengthening mechanisms contributing to the GTJs increasing hardness. Similar results are shown for changing Ni concentration (Figure 3-14b). In all conditions, there is an increase in hardness with increasing Cr and Ni content, which is consistent with equation (3).

Finally, after the initial increase in hardness within the first several layers of the graded regions in the GTJs, there is a significant hardness decrease (at locations of x=15,

19, and 24 mm for Inconel 82, P87 and 347H GTJs, respectively). Figure 3-8 shows that this hardness reduction is associated with austenite formation. The austenite phase stability can primarily be attributed to the increase in Ni concentration along the grade that eventually drives the M_s temperature below T_{RM}, thus stabilizing austenite. Formation of the mixed martensite/austenite regions can be understood with reference to solidification simulations, shown in Figure 3-9. Austenite (FCC) and carbides form during solidification (Figure 3-9c), and the segregation of the alloying elements plays a major role in the microstructure that forms upon cooling to T_{RM}. Cr, Ni, and Mo segregate to the intercellular regions (light regions in Figure 3-9a). Equation (2) can be used to estimate the variation in M_s temperature with position along the cellular substructure due to the micro segregation. The M_s temperature varied above and below T_{RM} (shown by the blue horizontal line) in the cell core and intercellular regions, respectively. This is consistent with the phases present from EBSD analysis in L7of the P87 GTJ where austenite is stable in the intercellular regions, which is attributed to the M_s temperature suppressed below T_{RM}.

Simulated Results

Some of the simulation results provide particular insight into microstructural evolution during aging (discussed below). Note that the $M_{23}C_6$ carbide stability follows the carbon concentration profiles (Figure 3-4c-d for Inconel 82, Figure 3-5a-b for P87, and Figure 3-5c-d for 347H). The carbon concentration depletes prior to every interface, and enriches into the subsequent layer. This is controlled by the CPC gradient (Figure 3-6), as carbon will diffuse down the gradient to alleviate the CPC discontinuity at the interface. Nearly all the carbon resides in carbides.[13] Therefore, carbon must dissolve into the matrix

in order to diffuse. Of the three carbides in the system ($M_{23}C_6$, M_6C, and NbC), the $M_{23}C_6$ carbide is the least stable. $M_{23}C_6$ is considered a low temperature carbide due to its complex structure and lower dissolution temperature, which is confirmed in the equilibrium calculations shown in Figure 3-11.[31] For these reasons, this carbide will dissolve before the M_6C and NbC carbides.

In the Inconel 82 GTJ, there is negligible diffusion at the layer interfaces after L4 (Figure 3-4c), which is coincident with the $M_{23}C_6$ carbide dissolution and NbC stability (Figure 3-4d). Additionally, austenite becomes the dominant phase in this region. Carbon can diffuse faster through a BCC matrix, thus the FCC matrix after L4 limits the diffusion of carbon in the matrix.[35] Furthermore, the carbon resides in the Nb carbide (since the $M_{23}C_6$ carbide dissolved), which also shows negligible enrichment or depletion at the layer interfaces. Even though chromium is relatively high in Inconel 82, the increase in Nb concentration across the graded region stabilizes NbC over the $M_{23}C_6$ carbide at 600°C. It is interesting to note that even the sharp discontinuities in CPC at the interfaces are not alleviated after aging up to 8,000 hours. This effect may be associated with carbon being tied up in the highly stable NbC. Similar trends are shown in the other two filler metals.

Aged Microstructures

The modeling results described above can be combined with experimental observations to explain the hardness trends observed in Figure 3-3a-d. The conventional DMW exhibits a reduction in hardness in the HAZ that is attributed to tempering of the martensitic microstructure during aging. Additionally, there is a localized reduction in hardness directly adjacent to the fusion line that can be attributed to carbon diffusion, which

results in a carbon depleted region in the HAZ of Grade 22, and a carbon enriched region in the PMZ. This is consistent with the carbon diffusion calculation (Figure 3-4a) that shows the same carbon depleted and enriched regions in the HAZ and PMZ, respectively. The carbon diffusion is attributed to the negative chemical potential gradient from the Grade 22 to the Inconel 82. Carbon will eventually exceed the solubility limit in the PMZ, resulting in $M_{23}C_6$ formation, as shown in the phase fraction of carbides in Figure 3-4b. A local increase in carbide content will increase the hardness, and this is consistent with the hardness trace shown in Figure 3-3a.

The GTJs experience the same trend as the DMW regarding the tempering of the martensitic microstructure in the HAZ, which contributes to the observed reduction in hardness. Additionally, there is an overall reduction in hardness in the martensitic layers of the graded region for all three filler metals, prior to the austenite formation. This is also attributed to the tempering of the martensitic microstructure during aging. Furthermore, enhanced carbon diffusion occurs in the GTJs at the layer interfaces, as shown in Figure 3-4c and Figure 3-5(a and c). This is consistent with the photomicrographs in Figure 3-7 that show the carbides in the regions of significant hardness changes in the beginning layers, specifically in the Inconel 82 GTJ. All three filler metals exhibit a hardness decrease in the HAZ adjacent to the HAZ/L1 interface, and an increase at the beginning of L1. The carbon (and corresponding carbide) calculation also exhibits depletion and enrichment in these regions, shown by the calculated carbon and $M_{23}C_6$ carbide in Figure 3-4c-d. The microstructural features in these images presented in Figure 3-7 are consisted with the $M_{23}C_6$ carbide trend, and account for the hardness decrease in the HAZ, and the increase into L1 (Figure 3-3b). Additionally, a decrease in hardness across L1 is shown for

Inconel 82 and P87 in all aged conditions, and observed in 347H after 8,000 hours. This can also be attributed to variation in $M_{23}C_6$ content shown in the model, and validated by the observations in the photomicrographs represented by the Inconel 82 GTJ in Figure 3-7b-c. In addition, the lath martensite is relatively fine in the beginning of L1 and coarser at the end of L1, which can also contribute to the hardness decrease across this layer. The combination of reduced carbides and coarser lath martensite accounts for the observed decrease in hardness across the layer. As described previously, although carbon diffusion and the associated microstructural changes are somewhat accelerated near the interfaces of the GTJs, they are significantly reduced relative to the conventional DMW. The P87 GTJ exhibits similar trends. In this case, L6 exhibits decreased hardness (relative to L5) that is associated with a mixed martensite/austenite structure.

The increase in hardness observed in the Inconel 82 GTJ after 8,000 hours and the 347H GTJ after L10 after aging for 2,000 hours can likely be attributed to precipitation that is known to occur in these alloys. Alloy 347H forms Nb carbides during aging.[36–41] Hajiannia *et. al.*[36] revealed that fine intercellular Nb carbide precipitates increased the hardness of the welded 347H after aging. This is consistent with the results of Minami *et. al.*[38] who used transmission electron microscopy to show the presence of fine nanometer scale Nb carbides in the same alloy. The presence of the fine Nb carbides also contribute to the increase in hardness in the Inconel 82 GTJ. Klueh and King[42] investigated the thermal aging behavior of Inconel 82 after aging up to 10,000 hours at various temperatures. They also observed a precipitate that developed in the matrix that was associated with the cellular-dendritic substructure and the concomitant solute rejection from the solidification process. Since Inconel 82 has a Nb content of 2.36 weight percent,

it is expected Nb carbides will form and provide an overall increase in strength. The presence of Nb carbides in both materials are consistent with the calculated carbide phase fraction from the simulations that show the stability of NbC in the graded region.

Ni-Rich Martensite

The Ni-rich martensite does not form in the as-welded condition, but forms in all the GTJs after aging at 600°C due to austenite stability at this temperature. Austenite stability was confirmed in Figure 3-11 that shows thermodynamic equilibrium plots for a given layer. With increasing layer, the FCC phase increases in phase fraction and, upon cooling, transforms to martensite. This is confirmed with the photomicrographs in Figure 3-10. Since the martensite transformation is diffusionless, the as-quenched martensite has the same composition of the parent austenite, most notably Ni.[30] This is confirmed with EDS results showing that the martensite is rich in Ni for the FCC phase (Figure 3-12a) as compared to the Ni in the BCC phase (Figure 3-12b). This is also confirmed from the EBSD results that show BCC is the stable phase until L7 (P87 GTJ), L5 (Inconel 82 GTJ), and L10 (347H GTJ). The lack of Ni-rich martensite in the as-welded condition is associated with the time necessary for austenite formation at 600°C. Figure 3-15a provides simulation results for non-equilibrium solidification of L3 for the Inconel 82 GTJ that shows FCC and carbides are expected to form during solidification. Due to the high cooling rates from the weld thermal cycles (and the high hardenability of this layer), the austenite transforms martensite during cooling. The subsequent thermal cycles do not allow enough time for the FCC phase to form at an elevated temperature. This is demonstrated in Figure 3-15b that shows the phase fraction as a function of time, aging from 400°C to 600°C. Since low

temperature kinetic data is limited, the Inconel 82 GTJ L3 (as an example) was simulated at a temperature of 400°C and then heated to 600°C. It takes almost 20 hours for the BCC and FCC phases to stabilize to the 600°C equilibrium phase fraction values. The sluggish transformation kinetics can be attributed to the low diffusivity of Ni in austenite. The inability to form Ni-rich austenite during the short thermal cycles associated with welding accounts for the lack of Ni-rich martensite in the as-welded condition.

Although the hardness and amount of Ni-rich martensite each increase along the grade, the increase in hardness cannot be attributed to the presence of the Ni-rich martensite. The hardness of martensite is largely affected by carbon concentration. The Ni-rich martensite could potentially have relatively high carbon (due to the high solubility of carbon in austenite). However, under these conditions, nearly all the carbon is tied up in the carbides.[13] This is confirmed from thermodynamic calculations, which demonstrate that the carbon in the FCC and BCC phases at 600°C was less than $1e^{-5}$ weight percent carbon, and the rest of the carbon was in the carbides. Additionally, nanohardness measurements conducted on each phase showed that the BCC matrix hardness was 4.84±0.77 GPa, while the Ni-rich martensite had a hardness of 5.06±0.43 GPa. Thus, there is no significant difference in hardness between these two phases. Finally, note that the hardness increases along the grade in the as-welded condition when no Ni-rich martensite is present, which is also consistent with the above observation.

A large body of work has investigated a quench, lamellarization, and tempering (QLT) process to determine the formation of a similar Ni-rich martensite constituent, similar to what is observed in this study.[43–46] Even though the Ni-rich martensite form from specific thermal cycle treatments and not after prolonged aging (as conducted in the current

study), the location and morphologies show similarities. The martensite morphology is largely effected by the initial microstructure prior to aging. When the sample is heated to 600°C, there will be regions were this temperature is above the Ac1 temperature (defined as the initiation of austenite transformation upon heating) and thus, austenite is stable. The initiation sites for the parent austenite formation are the martensite laths or prior austenite grain boundaries (PAGB).[43,44,47,48] The austenite that forms at the PAGB and/or lath boundaries will transform to a Ni-rich martensite, and take the form of rod-like morphology or blocky morphology, also described in the literature as "islands".[49] The blocky Ni-rich martensite forms mostly at the PAGB, while the rod-like martensite forms on the martensite laths.[47,48,50] A blocky morphology is clearly observed in Figure 3-13 for the 347H GTJ. Conversely, the elongated morphology of the Ni-rich martensite can be seen in Figure 3-7d and Figure 3-10b for Inconel 82 and P87, respectively.

Work is in progress to understand the tensile and creep properties of these GTJs relative to conventional DMWs and will be reported in separate articles.

Conclusions

Microstructural characterization was conducted on three GTJs in the as-welded and aged conditions. Thermodynamic and kinetic modeling of the joints was compared to the experimental results. The following conclusions can be drawn from this work.

1. The graded regions of the GTJs in the as-welded condition exhibit martensite in the first few layers of the grade, followed by a mixed martensite/austenite region, and then a fully austenitic region in the final layers.

2. The austenite stability in the final layers is attributed to the increase in Ni concentration that reduces the martensite start temperature below room temperature, thus stabilizing austenite. The preceding layers of mixed FCC/BCC are attributed to element segregation upon solidification that causes the martensite start temperature to vary above and below room temperature.
3. The increase in hardness within the martensitic region of the grade in the as-welded condition is associated with a decrease in the M_s temperature (less auto-tempering), a decrease in the Ac3 temperature (more as-quenched martensite), and solid solution strengthening. The subsequent decrease in hardness is associated with the austenite stability in the final layers.
4. Enhanced carbon diffusion occurs at the layer interfaces during aging, and is more significant in the beginning layers of the graded region. Although the carbon is tied up in carbides, the $M_{23}C_6$ carbide will dissolve, allowing carbon to diffuse due to the chemical potential gradient that is steepest in the beginning of the grade.
5. Significant hardness gradients can be attributed to the distribution of carbides throughout the layers from carbon diffusion and aging. Carbon/carbide depleted and enriched regions form at the end and beginning of a layer, respectively. This coincides with the hardness variation, as the overall hardness was observed to be higher at the beginning of each layer.
6. During aging at 600°C, both FCC and BCC phases are stable in the first several layers of the grade. The amount of Ni-rich FCC (austenite) increases as the Ni concentration increases throughout the grade. The Ni-rich austenite transforms to martensite with no change in composition during cooling.

References

1. Klueh, R.L., King, J.F. Austenitic Stainless Steel-Ferritic Steel Weld Joint Failures. *Weld J*. 1982;(September):302-311.
2. DuPont, J.N. Microstructural evolution and high temperature failure of ferritic to austenitic dissimilar welds. *Int Mater Rev*. 2012;57(4):208-234.
3. Dooley, B., Chang, P.S. The current state of boiler tube failures in fossil plants. *Fuel Energy Abstr*. 2002;43(4):56.
4. Ramu, I., Mohanty, S.C. Modal Analysis of Functionally Graded Material Plates Using Finite Element Method. *Procedia Mater Sci*. 2014;6(Icmpc):460-467.
5. Bhandari, M., Purohit, K. Analysis of Functionally Graded Material Plate under Transverse Load for Various Boundary Conditions. *IOSR J Mech Civ Eng*. 2014;10(5):46-55.
6. Gupta, A., Talha, M. Recent development in modeling and analysis of functionally graded materials and structures. *Prog Aerosp Sci*. 2015;79:1-14.
7. Lundin, C.D. Dissimilar Metal Welds — Transition Joints Literature Review. *Weld J*. 1982;(Feb):58s-63s.
8. Gittos, M., Gooch, T. The interface below stainless steel and nickel-alloy claddings. *Weld Res Suppl*. 1992:461-472.
9. Brentrup, G.J., DuPont, J.N. Fabrication and Characterization of Graded Transition Joints for Welding Dissimilar Alloys. *Weld J*. 2013;92(March):72-79.
10. Brentrup, G.J., DuPont, J.N., Snowden, B.S., Grenestedt, J.L. Design Considerations of Graded Transition. *Weld J*. 2012;91(September).
11. Sridharan, N., Cakmak, E., Jordan, B. Design, Fabrication, and Characterization of

Graded Transition Joints. *Weld J*. 2017;96:295-s-306-s.

12. DuPont, J.N., Marder, A.R. Dilution in Single Pass Arc Welds.pdf. *Metall Mater Trans B*. 1996;27B:481-489.
13. Galler, J.P., DuPont, J.N., Babu, S.S., Subramanian, M. Design of Graded Transition Joints through Thermodynamic and Kinetic Modeling. *Submitt to Weld J*.
14. Drouin, D., Couture, A.R., Joly, D., Tastet, X., Aimez, V., Gauvin, R. CASINO A Fast and Easy to use Modeling Tool for Scanning Electron Microscopy and Microanalysis. 2007;29:92-101.
15. Borgenstam, A., Höglund, L., Ågren, J., Engström, A. DICTRA, a tool for simulation of diffusional transformations in alloys. *J Phase Equilibria*. 2000;21(3):269-280.
16. Thermo-Calc Software MOB2 TCS Alloy Mobility Database.
17. Thermo-Calc Software TCFE7-TCS Steels/Fe-Alloys Database version 7.
18. Thermo-Calc Software Ni-Data-v7 Ni-Alloys Database.
19. Klueh, R.L. Heat treatment effects on creep and rupture behavior of annealed 2.25 Cr-1 Mo steel. *Metall Trans A*. 1978;9(11):1591-1598.
20. Laha, K., Chandravathi, K.S., Rao, K.B.S., Mannan, S.L., Sastry, D.H. An Assessment of Creep Deformation and Fracture Behavior of 2 . 25Cr-1Mo Similar and Dissimilar Weld Joints. *Metall Mater Trans a*. 2001;32A(January):115-124.
21. Parker, J.D., Stratford, G.C. Characterization of microstructures in nickel based transition joints. *J Mater Sci*. 2000;35(16):4099-4107.
22. Zhou, Y., Li, Y., Liu, Y. Precipitation behavior of type 347H heat-resistant

austenitic steel during long-term high-temperature aging. *J Mater Res*. 2015;30(23):3642-3652.

23. Banovic, S.W., DuPont, J.N., Marder, A.R. Experimental Evaluation of Fe-Al Claddings in High-Temperature Sulfidizing Environments. *Weld J*. 2001;(March):63-70.
24. DuPont, J.N., Kusko, C.S. Technical note: Martensite formation in austenitic/ferritic dissimilar alloy welds. *Weld J*. 2007;86(2):51.
25. Andrews, K.W. Empirical formulae for the calculation of some transformation temperatures. *J Iron Steel Inst*. 1965;(July):721-727.
26. Christoffel, R.J., Curran, M.R. Carbon Migration in Welded Joints at Elevated Temperatures. *Weld J*. 1956;35(9):457s-468s.
27. Porter, D.A., Easterling, K.E., Sherif, M.Y. *Phase Trasformations in Metals and Alloys*. Third. Taylor and Francis Group; 2009.
28. Darken, L.S. Diffusion of carbon in austenite with a discontinuity in composition. *Metall Mater Trans B Process Metall Mater Process Sci*. 1948;41(4):430-438.
29. Eckel, J.F. Diffusion Across Dissimilar Metal Joints. *Weld J*. 1964;43(4):170s-178s.
30. Krauss, G. *Steels: Processing, Structure, and Performance*. ASM International; 2015.
31. Sindo Kou. *Metallurgy Second Edition Welding Metallurgy*. Vol 822.; 2003.
32. Hertzberg, R.W., Vinci, R.P., Hertzberg, J.L. *Deformation and Fracture Mechanics of Engineering Materials*. Fifth Edit. Wiley and Sons; 2013.
33. Krauss, G. Martensite in steel: strength and structure. *Mater Sci Eng A*. 1999;273-

275:40-57.

34. Bain, E.C. *Functions of the Alloying Elements in Steel*. American Society for Metals; 1939.

35. Callister, W.D., Rethwisch, D.G. *Materials Science and Engineering: An Introduction*. Vol 94.; 2007.

36. Hajiannia, I., Shamanian, M., Kasiri, M. Microstructure and mechanical properties of AISI 347 stainless steel/A335 low alloy steel dissimilar joint produced by gas tungsten arc welding. *Mater Des*. 2013;50:566-573.

37. Shalchi Amirkhiz, B., Xu, S., Liang, J., Bibby, C. Creep Properties and TEM Characterization of 347H Stainless Steel. *36th Annu CNS Conf*. 2016;(June).

38. Minami, Y., Kimura, H., Tanimura, M. Creep Rupture Properties of 18 Pct Cr-8 Pct Ni-Ti-Nb and Type 347H Austenitic Stainless Steels. *J Mater Energy Syst*. 1985;7(1):45-54.

39. Mittal, R., Sidhu, B.S. Microstructures and mechanical properties of dissimilar T91/347H steel weldments. *J Mater Process Technol*. 2015;220:76-86.

40. Sourmail, T. Precipitation in creep resistant austenitic stainless steels. *Mater Sci Technol*. 2001;17(1):1-14.

41. Tanaka, H., Murata, M., Abe, F., Yagi, K. The effect of carbide distributions on long-term creep rupture strength of SUS321H and SUS347H stainless steels. *Mater Sci Eng A*. 1997;234-236(97):1049-1052.

42. Klueh, R.L., King, J.F. Thermal-Aging Behavior of ERNiCr-3 Alloy (Weld and Base Metal). 1981;(August):ORNL-5783.

43. Barrick, E.J., Jain, D., DuPont, J.N., Seidman, D.N. Effects of Heating and

Cooling Rates on Phase Transformations in 10 Wt Pct Ni Steel and Their Application to Gas Tungsten Arc Welding. *Metall Mater Trans A*. 2017;48(12):5890-5910.

44. Isheim, D., Hunter, A.H., Zhang, X.J., Seidman, D.N. Nanoscale Analyses of High-Nickel Concentration Martensitic High-Strength Steels. *Metall Mater Trans Trans A*. 2013;44A(July).

45. Jain, D., Isheim, D., Zhang, X.J., Ghosh, G., Seidman, D.N. Thermally Stable Ni-rich Austenite Formed Utilizing Multistep Intercritical Heat Treatment in a Low-Carbon 10 Wt Pct Ni Martensitic Steel. *Metall Mater Trans A Phys Metall Mater Sci*. 2017;48(8):3642-3654.

46. Wu, S.J., Sun, G.J., Ma, Q.S., Shen, Q.Y., Xu, L. Influence of QLT treatment on microstructure and mechanical properties of a high nickel steel. *J Mater Process Technol*. 2013;213:120-128.

47. Matsuda, F., Ikeuchi, K., Fukada, Y. Review of mechanical and metallurgical investigations of M-A constituents in welded joint in Japan.pdf. *Transcations JWRI*. 1995;24(May 1996):1-24.

48. Li, Y., Baker, T.N. Effect of morphology of martensite–austenite phase on fracture of weld heat affected zone in vanadium and niobium microalloyed steels. *Mater Sci Technol*. 2010;26(9):1029-1040.

49. Davis, C.L., King, J.E. Effect of cooling rate on intercritically reheated microstructure and toughness in high strength low alloy steel. *Mater Sci Technol*. 1993;9(1):8-15.

50. Li, X., Ma, X., Subramanian, S.V., Shang, C., Misra, R.D.K. Influence of prior

austenite grain size on martensite-austenite constituent and toughness in the heat affected zone of 700MPa high strength linepipe steel. *Mater Sci Eng A.* 2014;616:141-147.

Appendix

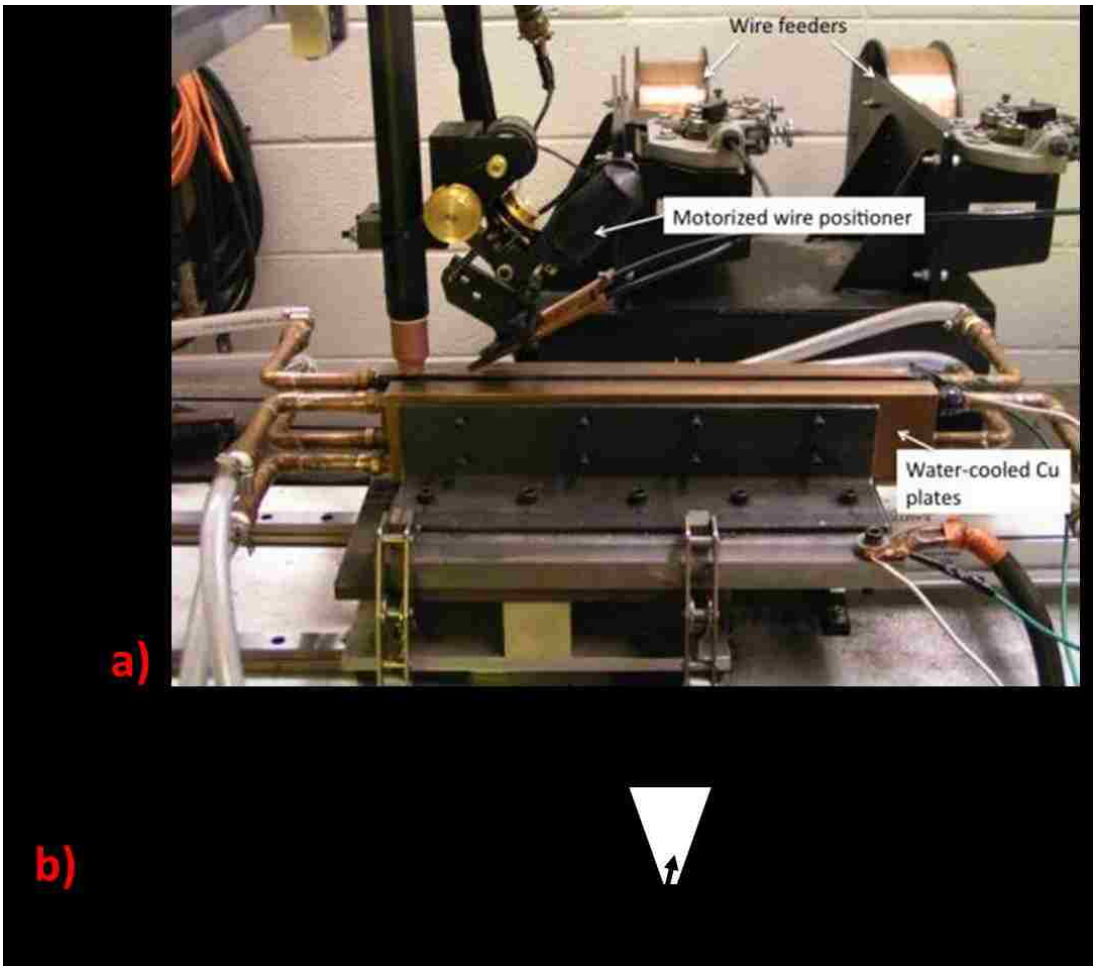

Figure 3-1. a) Image of the GTJ fabrication set up and b) schematic representation of the final GTJ product.

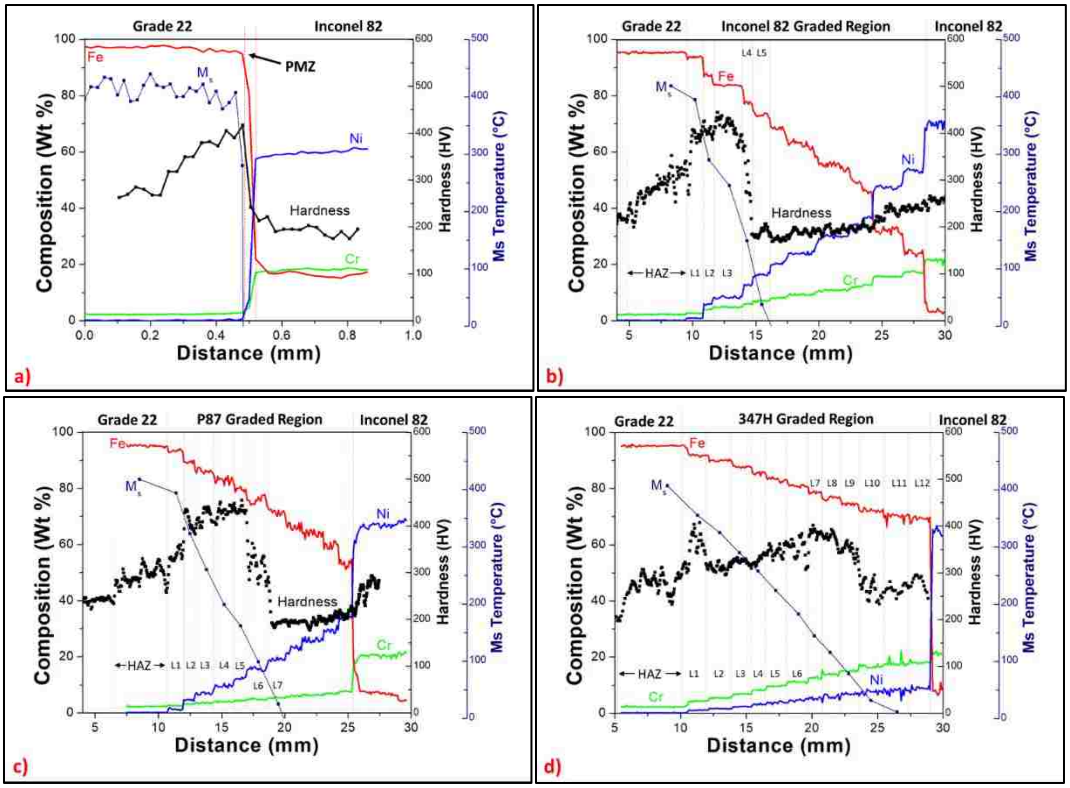

Figure 3-2. Composition, hardness, and martensite start temperature as a function of distance for a) DMW and GTJs between Grade 22 and b) Inconel 82, c) P87, and d) 347H.

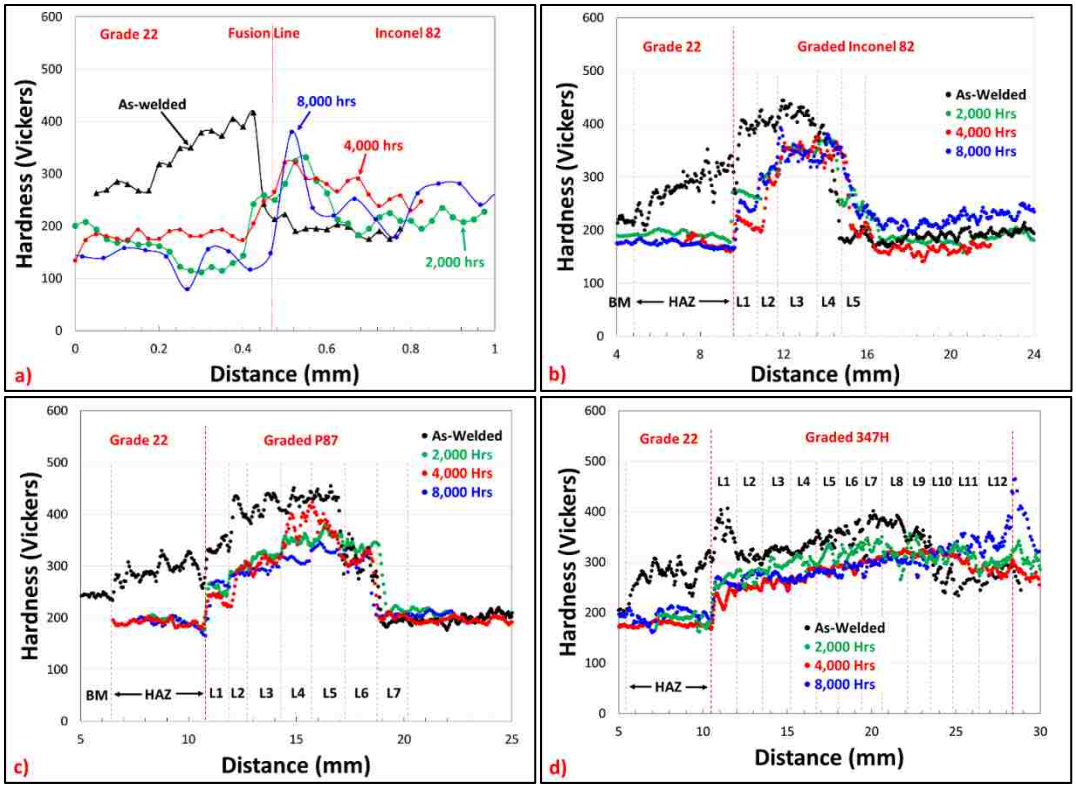

Figure 3-3. Hardness as a function of distance for a) DMW and GTJs between Grade 22 and b) Inconel 82, c) P87, and d) 347H for the as-welded and aged conditions.

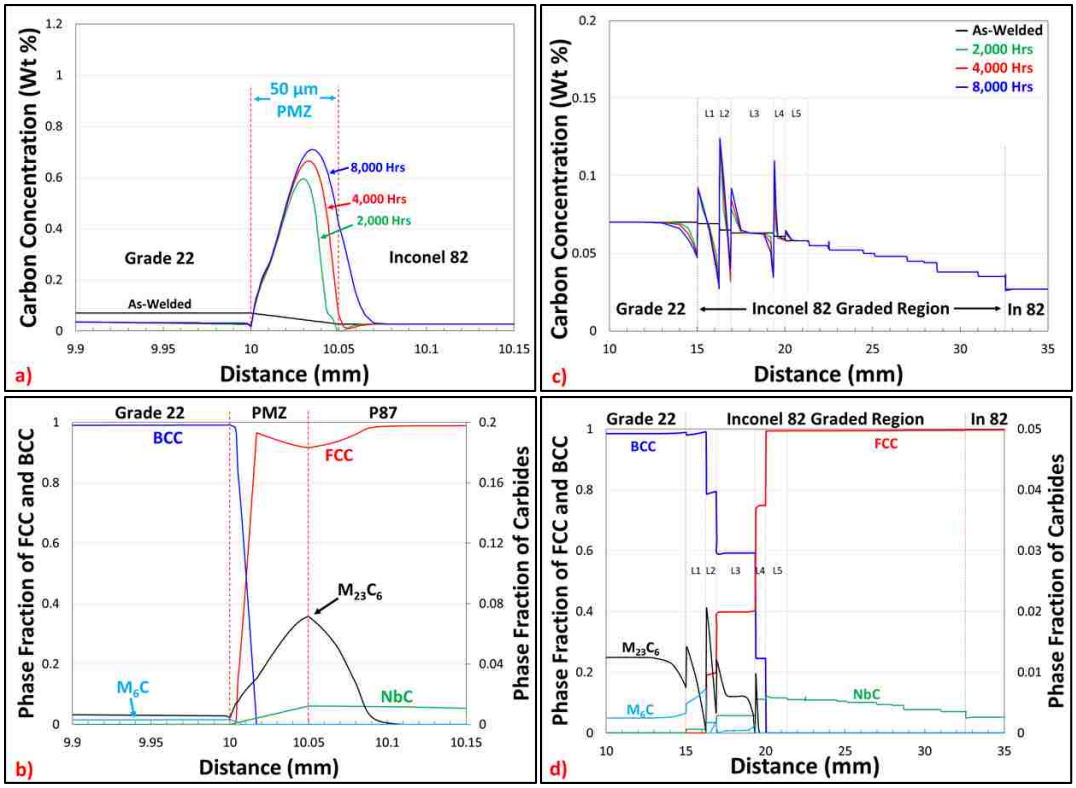

Figure 3-4. Calculated carbon concentration and phase fraction as a function of distance at the simulated aging temperature of 600°C for 8,000 hours for (a-b) conventional DMW and (c-d) the Inconel 82 GTJ.

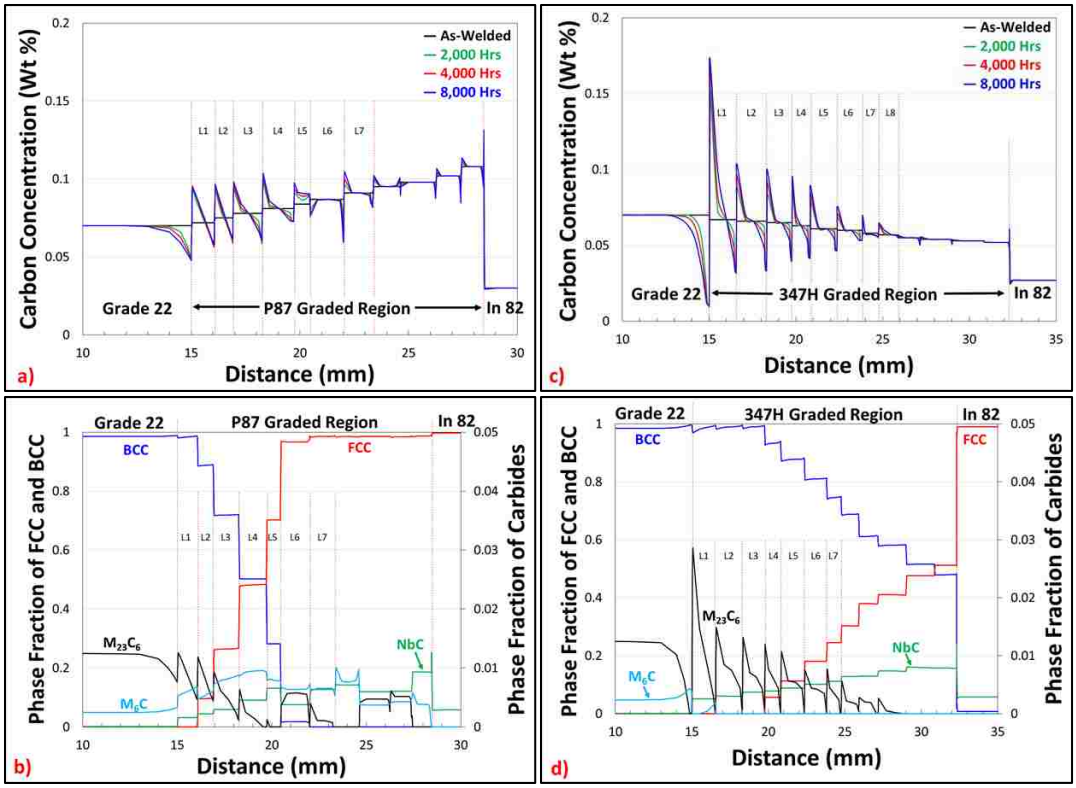

Figure 3-5. The carbon concentration and phase fraction as a function of distance at the simulated aging temperature of 600°C for 8,000 hours for (a-b) the P87 GTJ and (c-d) the 347H GTJ.

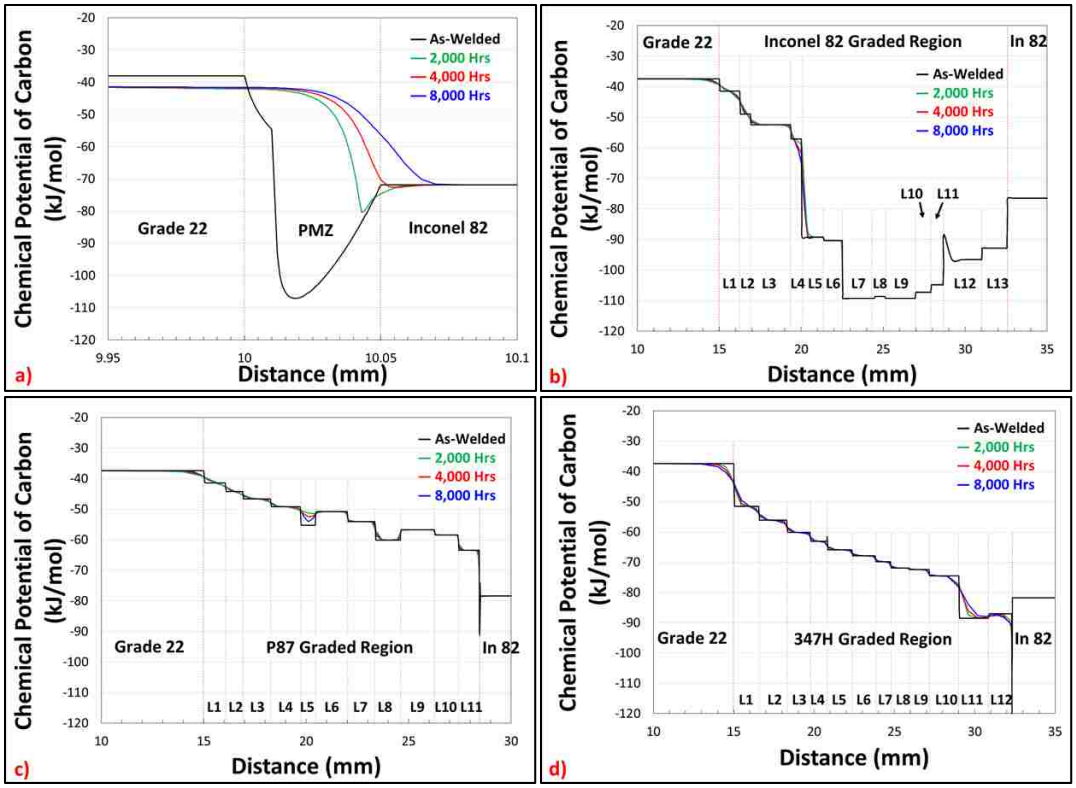

Figure 3-6. The chemical potential of carbon at 600°C in the as-welded and aged conditions for a) conventional DMW, b) Inconel 82 GTJ, c) P87 GTJ, and d) 347H GTJ.

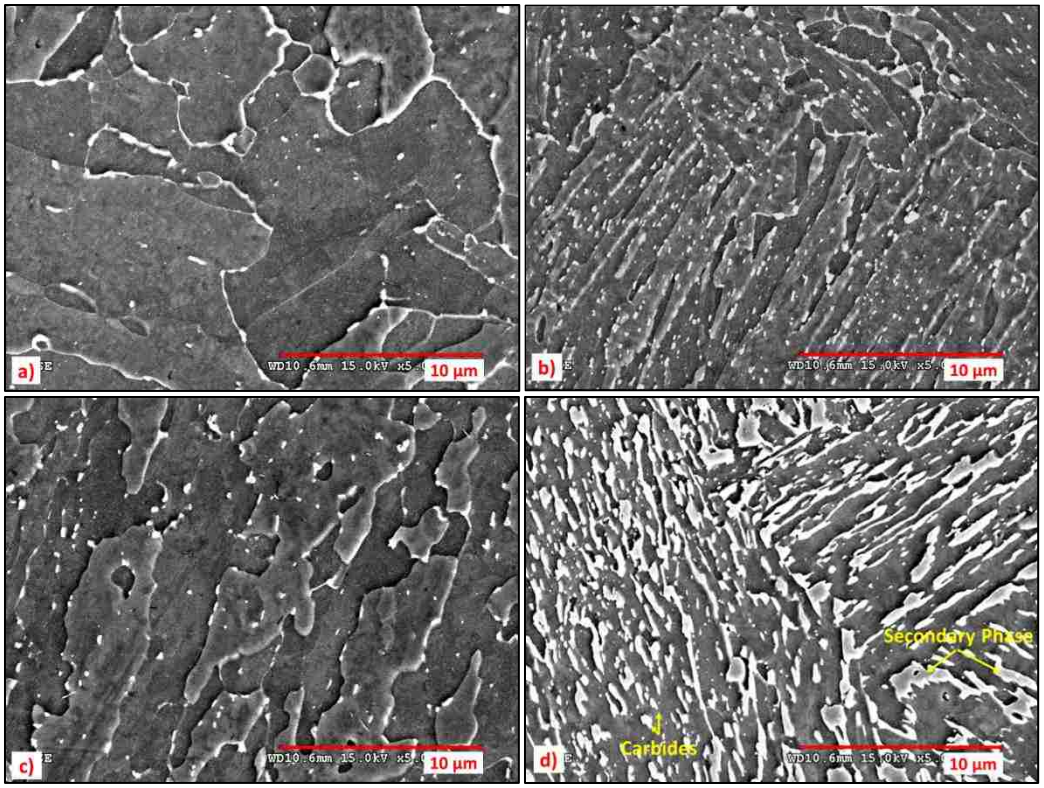

Figure 3-7. SEM photomicrographs of the Inconel 82 GTJ aged for 4,000 hours showing a) Grade 22 substrate HAZ, b) beginning of L1, c) end of L1, and d) beginning of L2.

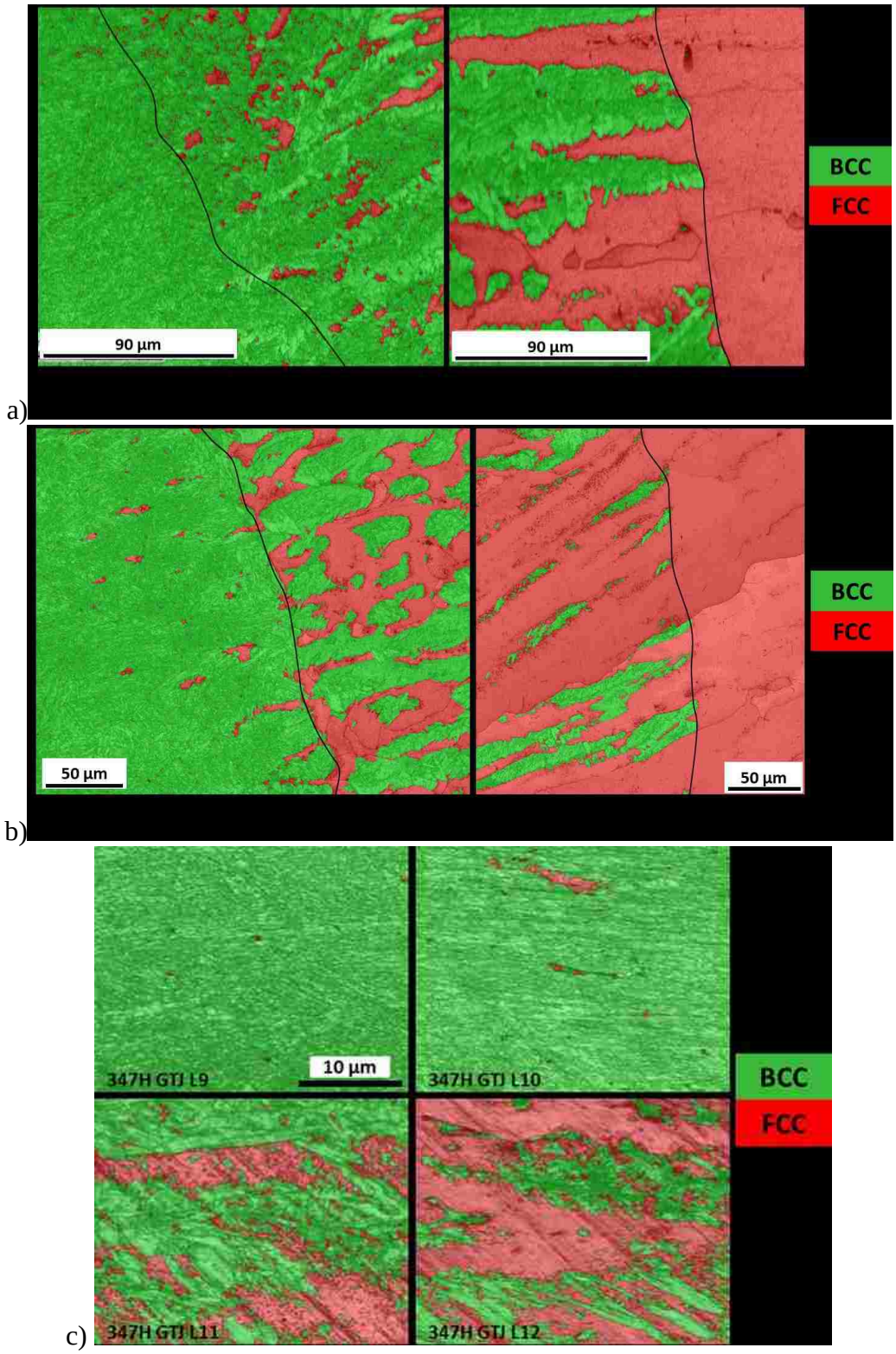

Figure 3-8. EBSD phase maps overlaid with image quality maps showing the transition to austenite for the GTJ using a) Inconel 82, b) P87, and c) 347H. (Note micron bar in L9 is for all four layers).

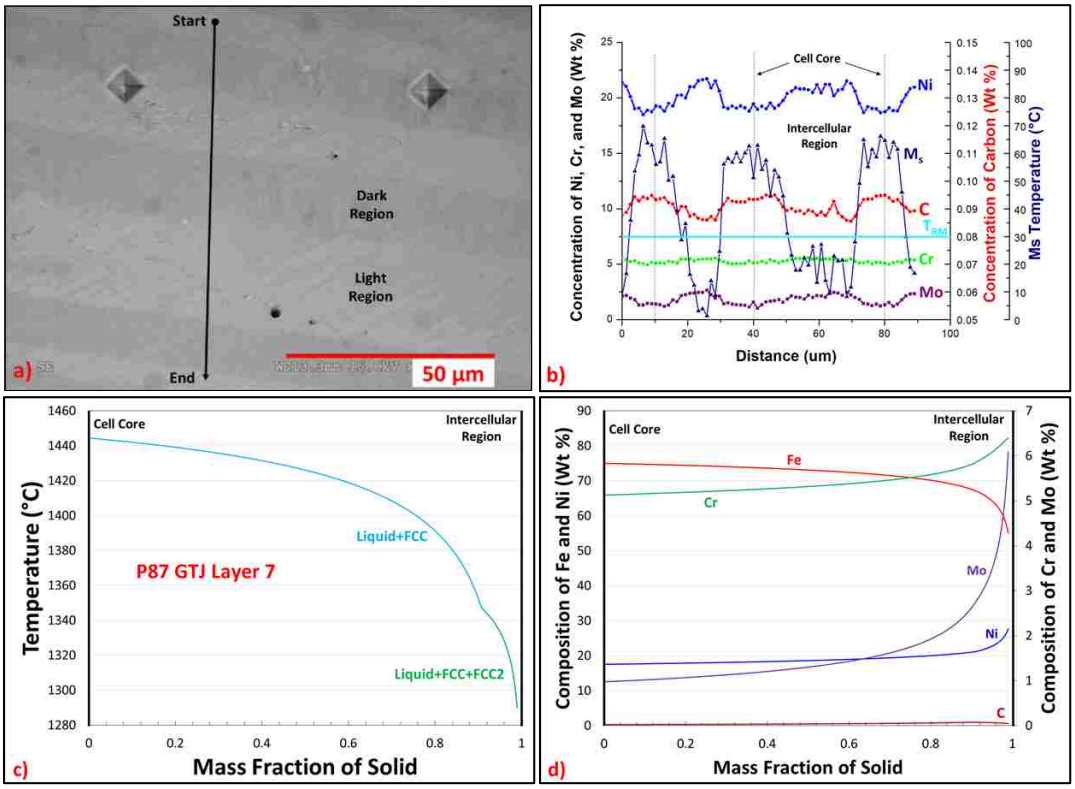

Figure 3-9. a) LOM image superimposed over the SEM image showing the location of the EDS scan in L7 of the P87 GTJ, b) the results from the EDS scan with the M_s temperature, and c) Scheil solidification simulation of L7 showing the phases that form, and d) element distribution of L7 in FCC during solidification.

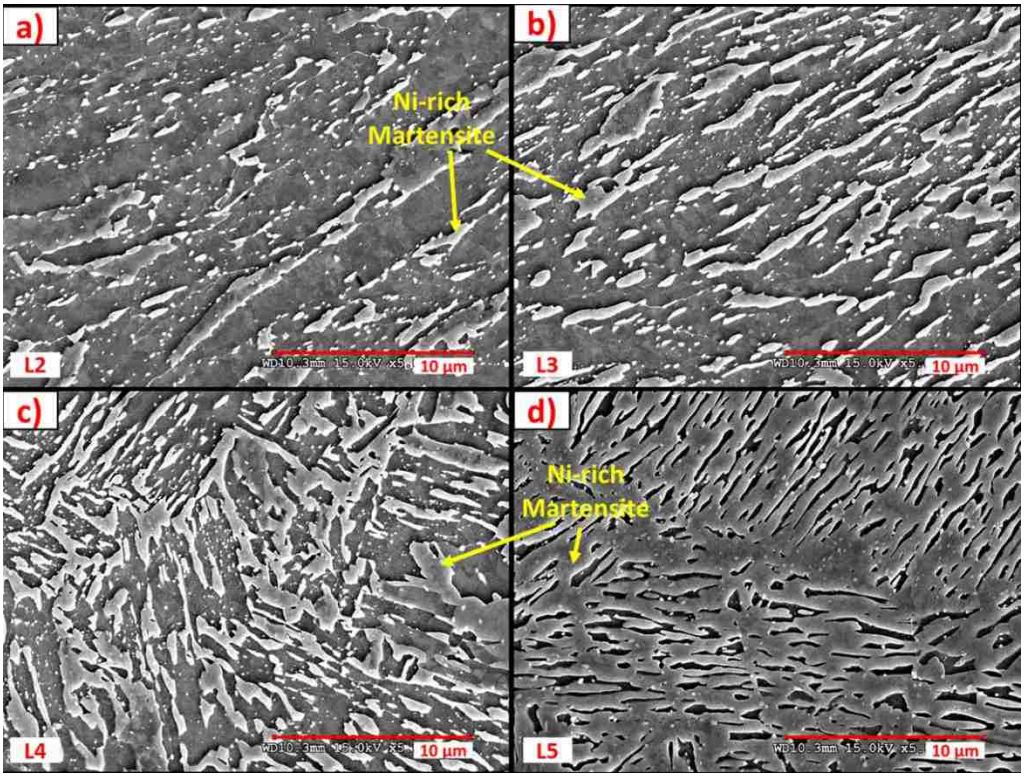

Figure 3-10. SEM photomicrographs of the P87 GTJ showing layers 2-5 aged for 8,000 hours showing the extent of the Ni-rich martensite formation.

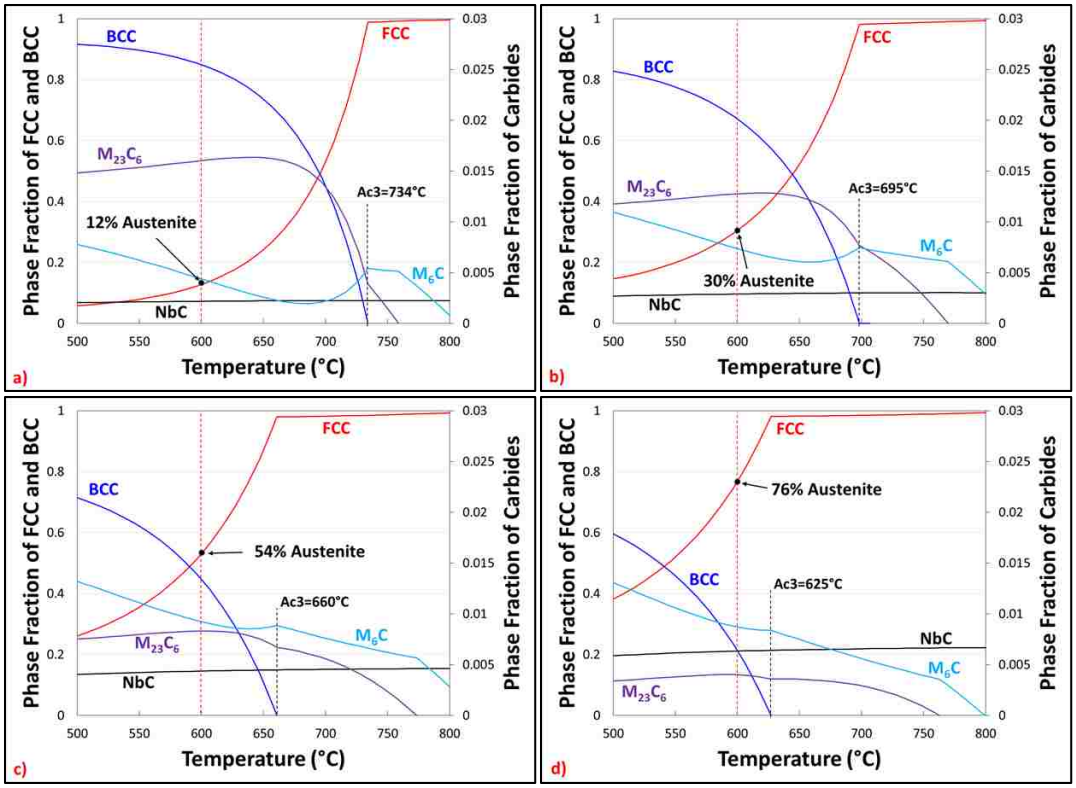

Figure 3-11. Calculated phase fraction as a function of temperatures for in a) L2, b) L3, c) L4, and d) L5 for the P87 GTJ for a simulated age at 600°C.

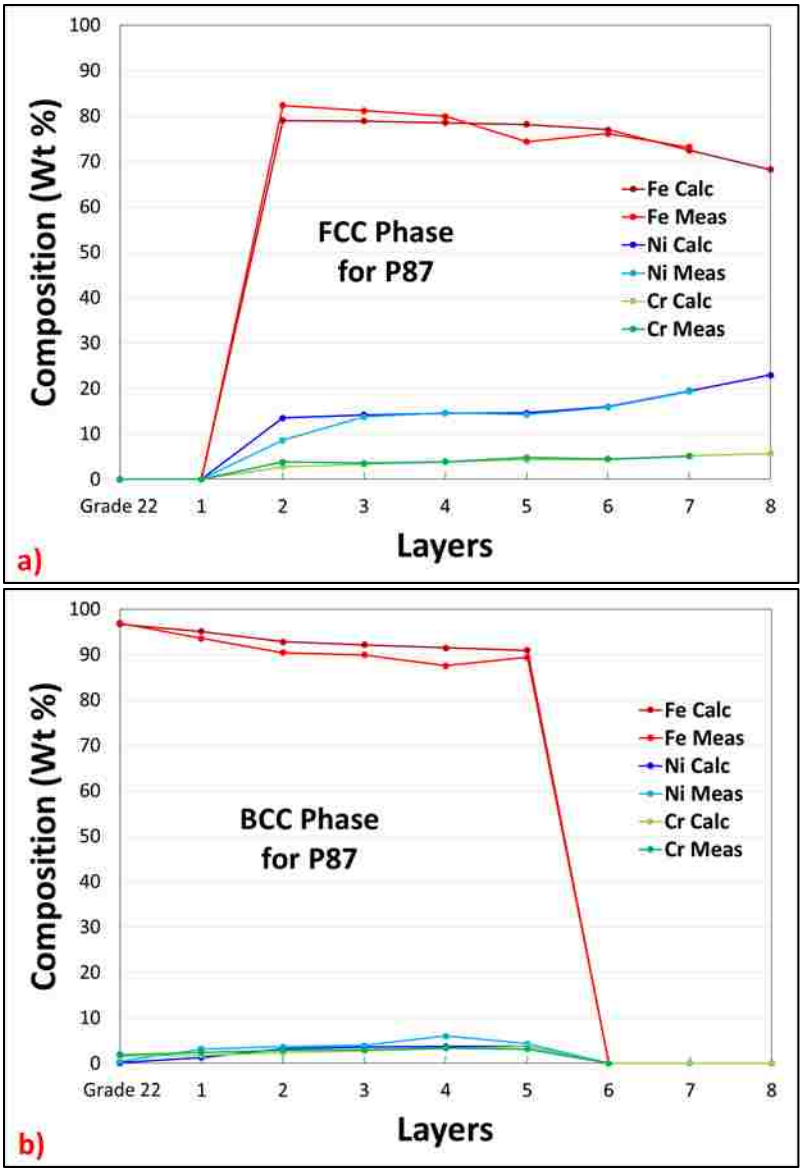

Figure 3-12. The measured and calculated compositions as a function of layers for the austenite phase in the P87 GTJ.

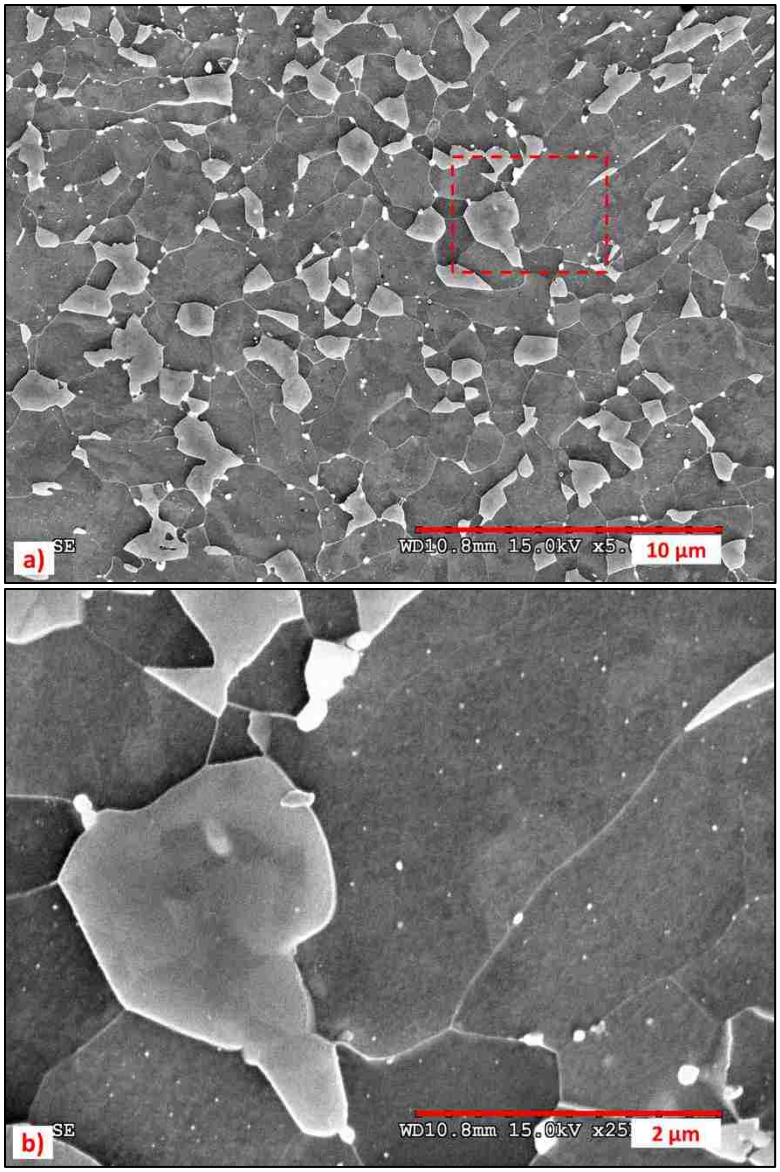

Figure 3-13. SEM Photomicrograph of L6 in the 347H GTJ aged for 8,000 hours showing the Ni-rich martensite for a) low and b) high magnifications.

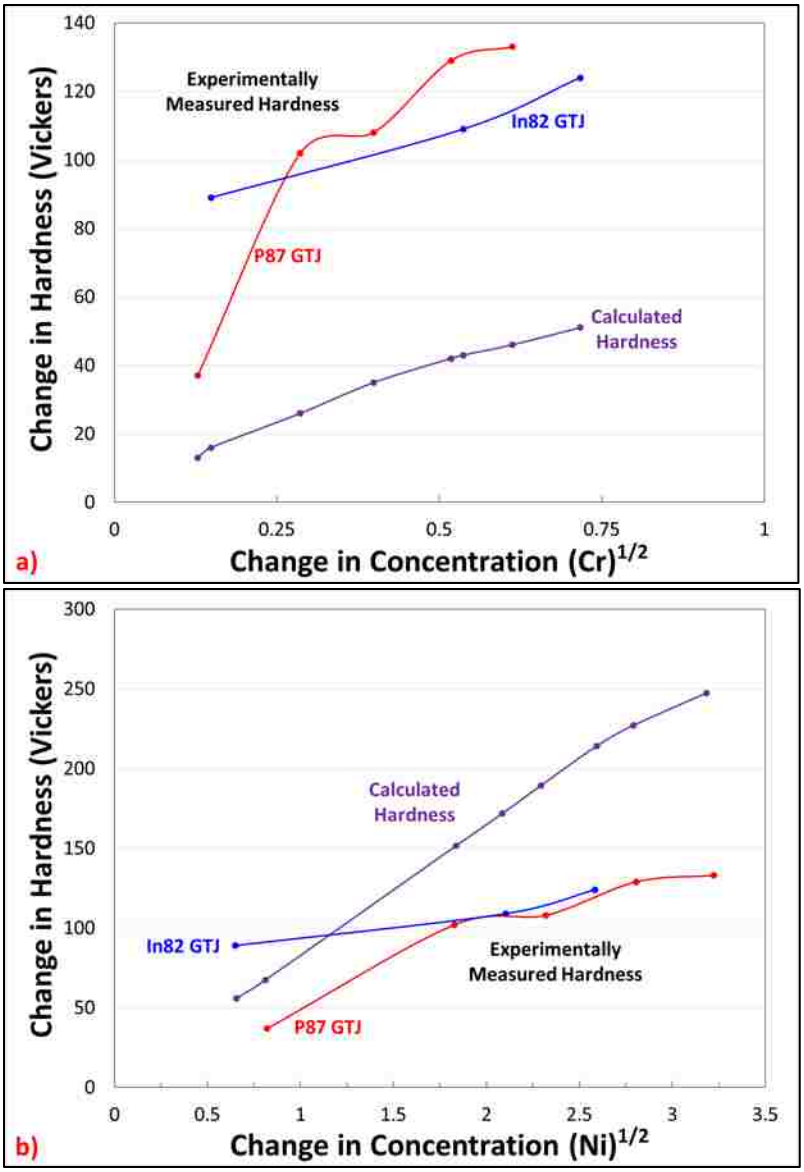

Figure 3-14. Expected change in hardness from the effects of Cr and Ni compared to the measured change in hardness in the Inconel 82 and P87 GTJs.

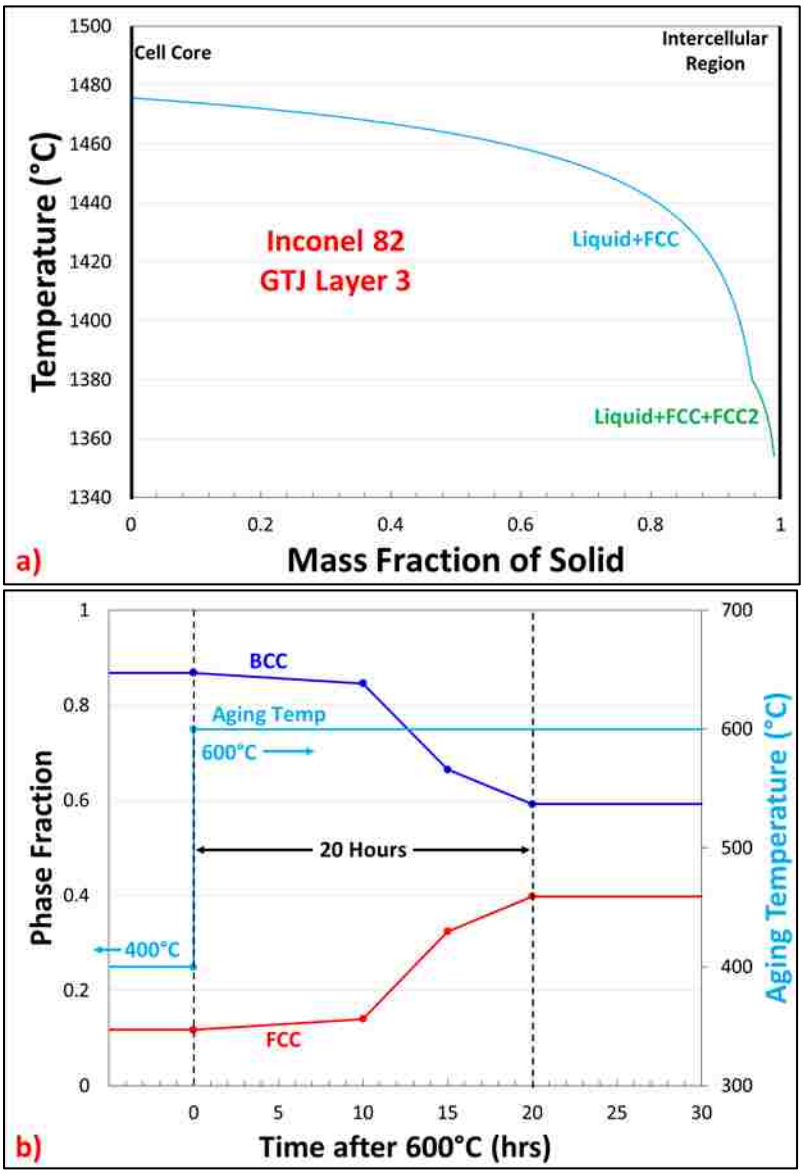

Figure 3-15. a) Scheil solidification model for the Inconel 82 GTJ L3 showing the phases that form upon solidification, and b) phase fraction and aging temperature as a function of time after reaching 600°C that shows how long it takes for the BCC and FCC phases to stabilize in L3 of the Inconel 82 GTJ.

Tables

Table 3-1. Chemical compositions of the Grade 22 plate and four welding wires, and inputs to the thermodynamic and kinetic models.

	Elements (All values in weight percent)												
Material	**Al**	**C**	**Cr**	**Cu**	**Mn**	**Mo**	**Nb**	**Ni**	**P**	**S**	**Si**	**Ti**	**Fe**
Grade 22 Substrate	0.03	0.07	2.20	0.14	0.52	0.92	<0.01	0.10	0.007	0.009	0.20	<0.01	Bal.
Inconel 82	-	0.027	21.4	0.016	3.20	-	2.36	70.8	0.003	<0.001	0.19	0.43	Bal.
EPRI P87	0.18	0.11	8.99	-	1.53	1.93	1.08	Bal.	0.004	0.001	0.22	0.10	40.4
347H	-	0.05	19.4	0.15	1.75	0.29	0.68	9.07	0.02	0.01	0.44	-	Bal.
90S-B3 (Grade 22 Wire)	0.01	0.07	2.45	0.16	0.60	0.93	<0.01	0.13	<0.005	0.005	0.58	-	Bal.

Table 3-2. Average EDS measurements compared to OES results for the custom standards.

		Elements (Values given in wt. %. N/A = not measured)								
Standards		**Si**	**Cr**	**Mn**	**Fe**	**Co**	**Ni**	**Cu**	**Nb**	**Mo**
Alloy 800	Ave	0.33	22.4	0.95	44.6	0.21	31.9	0.15	N/A	0.42
	OES	0.44	20.9	1.03	41.1	0.07	34.7	0.27	0.15	0.16
347	Ave	0.72	18.2	1.81	67.8	0.29	9.51	0.38	0.76	0.53
	OES	0.55	17.4	1.67	69.9	N/A	9.60	0.47	N/A	0.34
T22	Ave	0.49	2.37	0.57	94.8	0.21	0.07	0.03	N/A	1.41
	OES	0.38	2.19	0.50	Bal	N/A	0.06	0.09	N/A	1.01

Vita

Jonathan Galler was born on December 31, 1988 in New Haven, Connecticut to Michael and Barbara Galler. He grew up in Old Saybrook, CT with his parents and older brothers Michael and Matthew. Jonathan attended St. Johns for kindergarten, Kathleen E Goodwin Middle School, and Xavier High School, an all-boys catholic prep school where he was the captain of the tennis team, wrestled, and ran cross country. In August 2007, Jonathan enrolled in the University of Vermont in Burlington, VT where he majored in Mechanical Engineering and minored in Mathematics. He received his Bachelor of Science degree in Mechanical Engineering in 2011. He then applied to Lehigh University to pursue his Master's degree in Mechanical Engineering and Mechanics, which he received in May 2013. In June 2013, he joined the Engineering Metallurgy Group under the advisement of Dr. John DuPont. He worked on a residual stress development project for a year and published in Science and Technology of Welding and Joining, before switching projects to investigate the failure of dissimilar metal welds.